Ultrafast Electronic Processes in Doped Metal-Halide Perovskite Semiconductors



Aleksander Michal Ulatowski

Corpus Christi College

University of Oxford

A thesis submitted for the degree of

Doctor of Philosophy

Hilary 2023

Acknowledgements

I would like to thank everyone who has been a part of my DPhil experience. Your support and encouragement have been invaluable, and I am truly grateful for each and every one of you who has played a role in making this accomplishment a reality!

This work would not have been possible without funding provided by the Engineering and Physical Sciences Research Council (EPSRC) through the Centre for Doctoral Training (CDT) in Plastic Electronics. Apart from making it possible for me to undertake this journey, the CDT gathered a cohort of great people engaged in a wide variety of interesting research topics. I learned a lot through these multidisciplinary interactions, and I hope similar funding schemes will be available for future generations of graduate students. I would also like to express my gratitude to Rank Prize, whose funding through the Return to Research Grant was very helpful during the transition to hybrid working in the post-pandemic world.

I am deeply grateful to my supervisors, Professor Laura M. Herz and Professor Michael B. Johnston, for their guidance throughout my degree. Their expertise and experience were essential in helping me navigate the complexities of research, and their exceptional management skills led to the formation of a supportive and cooperative research group.

I would like to thank all members of the Semiconductors research group and the Terahertz Photonics group, who welcomed me so warmly at the start of my DPhil: Jay Patel, Sabrina Sterzl, Adam Wright, Kilian Lohmann, Hannah Eggimann, Juliane Borchert, Chelsea Xia, Mathias Rothmann, Alex Knight, Kun Peng, Tim Crothers, Leo Buizza, James Ball, Silvia Motti, Michael Trimpl, Djamshid Damry, and Kimberley Savill. Special thanks to Leo and Silvia, who taught me most of my laser lab skills and who were there for me with their support and friendship throughout my entire DPhil journey. Further big thanks to everyone who joined our team since then: Robbie Oliver, Elisabeth Duijnstee, Vincent Lim, Karim Elmestekawy, Qimu Yuan, Marcello Righetto, Siyu Yan, Jae Eun Lee, Ford Wagner, Snigdha Lal, Josh Lilly, Jiaxing Du, and Tom Siday. I would like to thank especially Vincent Lim for allowing me to find myself in an overseeing (el pastor) role and for all the great discussions and help, as well as Karim and Marcello for the science chats during tea breaks and for putting in great effort to proofread this thesis.

Lastly, I would like to thank my family and friends who believed in me and gave me the strength and motivation to continue through the challenges of the last few years. My warmest thanks go to my girlfriend, Aimee, for her support, care, and love.

Abstract

Electronic doping of semiconductors is an important topic in optoelectronics. Introducing small amounts of electron-rich or -poor dopants into the crystal structure of the semiconductor increases its conductivity and shifts the Fermi level, enabling efficient transistor, diode and photovoltaic device architectures. This thesis discusses the effects of doping in metal-halide perovskites, a novel group of semiconducting materials highly relevant for optoelectronic applications.

The properties of the doped materials are studied in this work with a variety of spectroscopic techniques, notably including terahertz (THz) spectroscopy. The analysis of terahertz transmission through thin films has proven to be an excellent tool for investigating optoelectronic properties of novel semiconductors. As the relation between the conductivity of the material and the THz transmission function is generally complicated, simple analytical expressions have been developed to enable straightforward calculations of frequency-dependent conductivity from experimental data in the regime of optically thin samples. However, significant deviations of the calculated photoconductivity from its actual value are observed in this thesis in semiconductors with high background conductivity when using these expressions. An alternative analytical formula is therefore developed, which greatly improves the accuracy of the estimated value of the photoconductivity while remaining simple to implement experimentally.

This improvement of data analysis methodology is highly relevant for studies of photoexcited charge-carrier dynamics in electrically-doped semiconductors, such as tin-iodide perovskites, where the commonly used expression for photoconductivity would result in an underestimate of charge-carrier mobility by over 50%. Tin-iodide perovskites are an important group of semiconductors for photovoltaic applications, as they exhibit higher intrinsic charge-carrier mobilities and lower toxicity than their lead-based counterparts. The spontaneous but controllable p-type doping in these materials provides an interesting opportunity to obtain novel insight into the effect of electronic doping on the dynamic processes, particularly on the intraband transitions of hot charge carriers in metal-halide perovskites. Using a new experimental technique, this thesis reveals that newly photogenerated charge carriers relax within the bands of $FA_{0.83}Cs_{0.17}SnI_3$ on a sub-picosecond timescale when a large, already fully thermalized (cold) population of charge carriers is present. Such rapid dissipation of the initial charge-carrier energy suggests that the propensity of tin-halide perovskites towards unintentional self-doping resulting from tin vacancy formation makes these materials less suited to implementation in hot-carrier solar cells than their lead-based counterparts.

Finally, an investigation of charge-carrier trapping and conduction in films of $MAPbBr_3$ perovskite chemically doped with bismuth is presented in this thesis. Successful chemical doping of metal halide perovskites with small amounts of heterovalent metals has attracted research attention because of its potential to improve long-term material stability and tune absorption spectra. However, some additives have been observed to impact negatively on optoelectronic properties, highlighting the importance of understanding charge-carrier behaviour in doped metal-halide perovskites. It is here found that the addition of bismuth has no effect on either the bandgap or exciton binding energy of the $MAPbBr_3$ host. However, a substantial enhancement of electron-trapping defects upon bismuth doping is observed, which results in an ultrafast charge-carrier decay component, enhanced infrared emission and a notable decrease in charge-carrier mobility. Such defects arise from the current approach to bismuth-doping through the addition of $BiBr_3$ salt, which may enhance the presence of bromide interstitials.

Contents

List of Publications vii

List of Abbreviations viii

1 Introduction 1

2 Background 6

2.1 Properties of Metal-Halide Perovskites . . . 7
2.1.1 Crystal Structure . . . 8
2.1.2 Optoelectronic Properties . . . 10
2.1.3 Defects . . . 11
2.2 Doping of Metal-Halide Perovskites . . . 15
2.2.1 Heterovalent Doping . . . 17
2.2.2 Tin-Halide Perovskites - Self Doping . . . 18
2.3 Hot-Carrier Solar Cells . . . 22
2.3.1 Overcoming the Thermodynamic Limit . . . 23
2.3.2 Charge-Carrier Cooling in Lead-Halide Perovskites . . . 25
2.3.3 Tin-Halide Perovskites - Hot-Carrier Relaxation . . . 29
2.4 Conclusions . . . 30

3 Spectroscopic Techniques and Semiconductor Theory 33

3.1 Energy Levels and Absorption Spectroscopy . . . 34
3.1.1 Experimental Implementation . . . 37
3.1.2 Data Analysis . . . 38
3.2 Radiative Transitions - Photoluminescence . . . 41
3.2.1 Steady-State Emission . . . 42
3.2.2 Time-Resolved Emission . . . 42
3.2.3 Experimental Implementation . . . 43
3.3 Charge-Carrier Dynamics . . . 45
3.4 Terahertz Spectroscopy . . . 48
3.4.1 Time-Domain Spectroscopy . . . 49
3.4.2 Optical-Pump–THz-Probe . . . 54
3.4.3 Pump-Push-Probe Spectroscopy . . . 55

4 Terahertz Conductivity Analysis in Doped Semiconductors 58
4.1 Introduction . . . 59
4.2 Methodology . . . 60
4.2.1 Transmission Function . . . 60
4.2.2 Material Properties . . . 62
4.3 Results . . . 66
4.3.1 Dark Conductivity Calculations . . . 66
4.3.2 Photoconductivity - Common Approach . . . 68
4.3.3 Photoconductivity of Conductive Films . . . 71
4.4 Experimental Implementation . . . 74
4.5 Effects of Charge-Carrier Scattering Time . . . 79
4.5.1 Assessment of Photoconductivity Estimates . . . 79
4.5.2 Simulated Transmission Functions . . . 80
4.6 Conclusions . . . 82

5 Hot Carrier Thermalisation Dynamics in Doped Tin-Iodide Perovskites 83
5.1 Introduction . . . 84
5.2 Background . . . 84
5.3 Results and Discussion . . . 88
5.3.1 Charge-Carrier Dynamics . . . 90
5.3.2 Chemical Doping . . . 95
5.3.3 Push Energy Dependence . . . 99
5.3.4 Spectral Analysis of Conductivity . . . 101
5.4 Conclusion . . . 105

6 Charge-Carrier Dynamics in Bi-Doped Perovskites 107
6.1 Introduction . . . 108
6.2 Results and Discussion . . . 110
6.2.1 Band Structure Changes . . . 110
6.2.2 Energetic Landscape . . . 112
6.2.3 Charge-Carrier Dynamics . . . 114
6.3 Final Remarks and Conclusion . . . 125

7 Conclusion and Outlook 130

Appendices

A Supplementary Characterisation and Data for Chapter 5 137
A.1 Absorption Measurements . . . 137
A.2 Sample Fabrication . . . 137
A.3 Photoconductivity Calculation . . . 139
A.4 Push-Wavelength Dependence and Decay Fitting . . . 140
A.5 Investigation of the Origin of the Negative Photoconductivity . . . 141

B Supplementary Data for Chapter 6 **146**
B.1 Sample Preparation 147
B.2 THz Photoconductivity 148
B.2.1 Determination of the Ratio of Electron to Hole Mobility 148
B.2.2 OPTP-Full Dataset 149
B.3 Structural Characterisation 150
B.3.1 X-Ray Diffraction 150
B.3.2 Phonon Modes 152

References **154**

List of Publications

Ulatowski, A.M., Wright, A.D., Wenger, B., Buizza, L.R., Motti, S.G., Eggimann, H.J., Savill, K.J., Borchert, J., Snaith, H.J., Johnston, M.B. and Herz, L.M. 'Charge-carrier trapping dynamics in bismuth-doped thin films of $MAPbBr_3$ perovskite'. *The Journal of Physical Chemistry Letters*, **2020** 11(9), 3681-3688.

Ulatowski, A.M., Herz, L.M. and Johnston, M.B. 'Terahertz conductivity analysis for highly doped thin-film semiconductors'. *Journal of Infrared, Millimeter, and Terahertz Waves*, **2020** 41(12), 1431-1449.

Ulatowski, A.M., Farrar, M.D., Snaith, H.J., Johnston, M.B. and Herz, L.M. 'Revealing Ultrafast Charge-Carrier Thermalization in Tin-Iodide Perovskites through Novel Pump–Push–Probe Terahertz Spectroscopy'. *ACS Photonics*, **2021** 8(8), 2509-2518.

Savill, K.J., **Ulatowski, A.M.**, Farrar, M.D., Johnston, M.B., Snaith, H.J. and Herz, L.M. 'Impact of Tin Fluoride Additive on the Properties of Mixed Tin-Lead Iodide Perovskite Semiconductors'. *Advanced Functional Materials*, **2020** 30(52), 2005594.

Savill, K.J., **Ulatowski, A.M.** and Herz, L.M. 'Optoelectronic properties of tin–lead halide perovskites'. *ACS Energy Letters*, **2021** 6(7), 2413-2426.

Lim, V.J.Y., **Ulatowski, A.M.**, Kamaraki, C., Klug, M.T., Miranda Perez, L., Johnston, M.B. and Herz, L.M. 'Air-Degradation Mechanisms in Mixed Lead-Tin Halide Perovskites for Solar Cells'. *Advanced Energy Materials*, **2022** 2200847.

Buizza, L.R., Sansom, H.C., Wright, A.D., **Ulatowski, A.M.**, Johnston, M.B., Snaith, H.J. and Herz, L.M. 'Interplay of Structure, Charge-Carrier Localization and Dynamics in Copper-Silver-Bismuth-Halide Semiconductors'. *Advanced Functional Materials*, **2022** 32(6), p.2108392.

Xia, C.Q., Poncé, S., Peng, J., **Ulatowski, A.M.**, Patel, J.B., Wright, A.D., Milot, R.L., Kraus, H., Lin, Q., Herz, L.M., Giustino, F. and Johnston, M.B. 'Ultrafast photo-induced phonon hardening due to Pauli blocking in $MAPbI_3$ single-crystal and polycrystalline perovskites'. *Journal of Physics: Materials*, **2021** 4(4), 044017.

List of Abbreviations

THz . . . . . Terahertz
IPCC . . . . . Intergovernmental Panel on Climate Change
PV . . . . . Photovoltaic
PSC . . . . . Perovskite solar cell
DSSC . . . . . Dye-sensitised solar cell
PCE . . . . . Power conversion efficiency
HTL . . . . . Hole-transport layer
ETL . . . . . Electron-transport layer
FA . . . . . Formamidinium $CH(NH_2)_2$
FACs . . . . . Formamidinium-Caesium alloy
MA . . . . . Methylammonium CH_3NH_3
TA . . . . . Transient absorption
LO . . . . . Longitudinal-optical
FTIR . . . . . Fourier-transform infrared
PL . . . . . Photoluminescence
CCD . . . . . Charge-coupled device
SPAD . . . . . Single-photon avalanche detector
TCSPC . . . . . Time-correlated single-photon counting
TDS . . . . . Time-domain spectroscopy
OPA . . . . . Optical parametric amplifier
OAP . . . . . Off-axis parabola
FPGA . . . . . Field-programmable gate array
BBO . . . . . Barium borate
ND . . . . . Neutral-density
OPTP . . . . . Optical-pump–THz-probe
PPP . . . . . Pump-push-probe
IR . . . . . Infrared
SIG . . . . . Signal
IDL . . . . . Idler

1

Introduction

According to the United Nations, the world population will continue to grow, exceeding 8.5 billion in 2030, 9.7 billion in 2050 and reaching its peak of 10.4 billion in 2080s [1]. With the growth of the population, the demand for energy will also increase. In the recent World Energy Outlook 2022 report, the International Energy Agency states that about a 1%-increase in energy demand is expected per year until 2030. At the same time, it predicts a lowering of fossil fuels' contribution to the total energy production market in the next couple of decades [2]. The decarbonisation of energy production is a necessity, due to the continuous rise of the global average temperature caused by anthropogenic activity. The Intergovernmental Panel on Climate Change's (IPCC) Sixth Assessment Report states that greenhouse gas emissions must be reduced by 43% by 2030 in order to limit global warming to 1.5°C [3]. Failing to do so could, among other effects, threaten global food security due to extreme weather conditions and land degradation [4].

One of the efficient ways to reduce our dependence on fossil fuels is the deployment of renewable sources of energy, including photovoltaic (PV) technology. Although in the past the cost of the traditionally used silicon solar panels inhibited the implementation of solar farms as the main sustainable route for energy production, this is no longer

the case [5]. The current price of a PV module is about $0.34 per watt of electricity production, which amounts to barely around 20% of the total cost of building a solar farm, currently costing around $1.72/W [6]. Such low cost of the silicon panels themselves, compared to the high cost of labour and structural and electrical systems, implies that further cost reduction of the panels will not significantly influence the overall price of building new solar farms. Therefore, rather than searching for materials and processes that would lower the cost of solar panels, an effort should be made to increase their efficiency at similar production costs. The higher power output at a similar production cost would lead to a further reduction of price per watt of solar technology, therefore allowing for the widespread use of photovoltaics.

The lack of significant progress in the efficiency of silicon-based solar cells over the decades [7] indicates that the search for novel material is necessary in order to revolutionise the market with a low-cost, high-output solution. In recent years, perovskite photovoltaics has been seen as the most promising technology to achieve this goal [8]. The fast-paced research into perovskite solar cells (PCS) resulted in over 25% power conversion efficiency being achieved in only one decade of work since solid-state perovskite photovoltaic devices were first demonstrated [7, 9, 10]. By comparison, it took silicon technology 40 years to show similar progress [7]. The impressive improvements in the field of PCSs have been largely caused by the extraordinary properties of these materials (fully discussed in Chapter 2 of this thesis), as well as the ease of their synthesis using cheap and simple solution-based methods [8]. However, achieving a similar performance to that of silicon technologies alone is not sufficient to dominate the market and reduce the price of sustainable energy production. Perovskite-based technology must observe further growth, surpassing the efficiency of current commercial modules at a similar cost of production.

The improvement of the performance of perovskite solar cells can be achieved by employing complex architectures of the photovoltaic devices, such as tandem solar cells,

where two different sub-modules are used to more efficiently absorb solar radiation [8], or by further improving the efficiency of single-layer solar cells, close to the theoretical limit of 32% power conversion [11]. One route to reach this limit is via doping of the perovskite material with a small amount of impurities, which could help in achieving the higher performance of the photovoltaic device through the improvement of the optoelectronic properties of the active material (via e.g. defect passivation) or through the increase of carrier extraction efficiency (by employing P-I-N architecture instead of using selective extraction layers). Alternatively, future-technology hot-carrier solar cells could be developed, which have the potential to exceed the theoretical limit of power conversion efficiency by operating under non-thermal equilibrium conditions [12]. This thesis discusses the potential routes and their limitations of achieving high-performing perovskite solar cells, focusing on the effects of doping in metal-halide perovskites and their implications for obtaining hot-carrier photovoltaics. Chapter 2 investigates the current state of the perovskite research, introducing all necessary concepts and terminology to then explore the work done in order to establish reliable doping routes in perovskite semiconductors. The effects of self-doping are also surveyed and the readiness of the field to achieve hot-carrier photovoltaics is assessed in the context of recent charge-carrier cooling research.

The methodology used throughout the rest of the thesis is discussed in Chapter 3, which provides an overview of the spectroscopic techniques employed to unravel the optoelectronic properties of novel PV materials, together with their fundamental theoretical principles of operation based on semiconductor physics. Terahertz spectroscopy is described in most detail, as it was used as the core technique of research presented in this thesis for uncovering charge-carrier trapping dynamics, structural properties of the crystal, doping levels, and ultrafast changes of the optical conductivity of the investigated materials, making it a versatile technique for evaluating optoelectronic properties of new materials.

Chapter 4 is the first experimental chapter of this work. It presents a computational study evaluating the current data analysis techniques used in the field of terahertz spectroscopy for the extraction of photoinduced conductivity in doped semiconductors. The chapter finds that for heavily doped semiconductors, including some metal-halide perovskites, the commonly used methods of calculating conductivity from terahertz transmission data are invalid, causing a significant underestimate of charge-carrier mobility obtained this way. An alternative, simple approach to data analysis is proposed and numerically tested against the exact, computationally-heavy methods, showing great agreement and therefore establishing a new route of extracting the properties of doped materials from terahertz spectroscopy data.

The following Chapter 5 uses the proposed conductivity extraction method to investigate the ultrafast changes of conductivity in tin-iodide perovskite via a novel optical-pump–infrared-push–terahertz-probe spectroscopy scheme. This newly-developed experimental technique allowed for an assessment of the hot-carrier cooling dynamics, proving that an ultrafast energy-loss mechanism can hinder the applicability of doped perovskites for hot-carrier solar cells. This energy loss is found to be caused by interactions of hot charge carriers with a large ocean of cold dopant carriers, suggesting that doping-suppression methods have to be found in order to use tin-iodide perovskites in highly efficient solar cells.

The last experimental Chapter 6 describes a detailed investigation of bismuth doping effects on $MAPbBr_3$ perovskite films. As explained in Chapter 2, doping in metal-halide perovskites can be a powerful tool for achieving high-efficiency photovoltaic devices, but unwanted effects can curb the progress by degrading the optoelectronic properties of the doped material. Indeed, the study presented in Chapter 6 finds that introducing a small amount of bismuth into the perovskite structure through the addition of $BiBr_3$ salt reduces the charge-carrier mobility and reduces the lifetime of photoexcited carriers, therefore

decreasing the expected charge-extraction efficiency. A formation of intrinsic defects, namely bromide interstitials, is found to be most likely responsible for this deterioration of optoelectronic performance in this doping scheme, through selective, ultrafast trapping of free electrons. This trapping mechanism is uncovered through spectrally- and time-resolved photoluminescence measurements combined with measurements of transient conductivity changes with terahertz spectroscopy. In order to alleviate the negative effects of bismuth doping, halide interstitial formation would need to be suppressed through various chemical deposition schemes.

Finally, Chapter 7 summarises the topics discussed in the thesis, outlining the most important findings and their implications for future research in the field of perovskite semiconductors.

Additionally, Appendices A and B contain supplementary data for Chapters 5 and 6, supporting the conclusions made in the main text.

2

Background

Contents

2.1 Properties of Metal-Halide Perovskites 7
2.1.1 Crystal Structure 8
2.1.2 Optoelectronic Properties 10
2.1.3 Defects 11
2.2 Doping of Metal-Halide Perovskites 15
2.2.1 Heterovalent Doping 17
2.2.2 Tin-Halide Perovskites - Self Doping 18
2.3 Hot-Carrier Solar Cells 22
2.3.1 Overcoming the Thermodynamic Limit 23
2.3.2 Charge-Carrier Cooling in Lead-Halide Perovskites 25
2.3.3 Tin-Halide Perovskites - Hot-Carrier Relaxation 29
2.4 Conclusions 30

This chapter outlines the brief history of perovskite photovoltaics, introducing the most important concepts in the field that are relevant to the rest of this thesis. The principles of semiconductor doping are described together with extrinsic and intrinsic doping mechanisms in metal-halide perovskites. Finally, recent advances in investigating hot-carrier cooling dynamics in metal-halide perovskites are summarised in the context of future-generation photovoltaic technologies.

2.1 Properties of Metal-Halide Perovskites

The field of metal-halide perovskites stems from the area of Dye-Sensitised Solar Cells (DSSC) [13]- photoelectrochemical devices employing a thin (a few microns), porous layer of titanium dioxide (TiO_2) and a liquid electrolyte to transfer electric charges generated by sunlight to the conductive contacts of the cells [14]. However since the absorption of TiO_2 lies in the ultraviolet part of the solar spectrum, organic dyes have been used as sensitisers (injected into the porous structure of TiO_2) to extend the absorption to visible and infrared wavelengths in order to increase the power conversion efficiency (PCE, a fraction of the power of incident solar radiation converted to electrical power) of such devices [15].

The first reports of employing metal-halide perovskites as sensitisers of DSSC from 2009 and 2011 used methylammonium lead iodide ($MAPbI_3$) and methylammonium lead bromide ($MAPbBr_3$), due to their high absorption coefficients and the ease of fabrication through solution processing [16, 17]. Using metal-halide perovskites as sensitisers resulted in solar cells with PCE of 3.8%, and later 6.5%, but the lifetime of these devices was severely limited to a few minutes by the perovskite layer dissolving in the liquid electrolyte [17].

Finally, in 2012, a solid-state hole transport layer (HTL) was used instead of the electrolyte. This not only significantly extended the cells' lifetime but also boosted the efficiency of the PV devices to around 10% [9, 10]. Moreover, it was realised that the presence of the mesoporous titanium dioxide as an electron transport layer (ETL) was redundant, due to the great charge-transport properties of the perovskite material, and could be replaced with any hole-stopping material. This realisation led to intense research in the field of perovskite photovoltaics, which in one decade resulted in an impressive increase of power conversion efficiency from 10.9% in 2012 [10] to 25.8% in 2022 [7].

2.1.1 Crystal Structure

The family of metal-halide perovskite semiconductors extends far beyond the methylammonium lead halides used in the above-mentioned studies. The perovskite structure (crystal structure analogue to that of Perovskite mineral $CaTiO_3$) can be formed by many compositions of the ABX_3 form [18]. As shown in Figure 2.1, a perovskite crystal is formed by a large cation on the A-site surrounded by metal-halide octahedral cage. The A-site is occupied either by a molecular cation - usually methylammonium or formamidinium, or by a large atom ion, such as caesium. A mixture of these cations can also be used, which results in the best stability of the crystal and optimal optoelectronic properties, as explained below [19, 20]. The metal cation B-site in the structure is most often occupied by lead or tin, or a mixture of thereof in the case of low-bandgap applications [21]. Halide site X can host iodine, bromine, or chlorine anions, again with some mix of those being most often used. The stability of a perovskite structure can

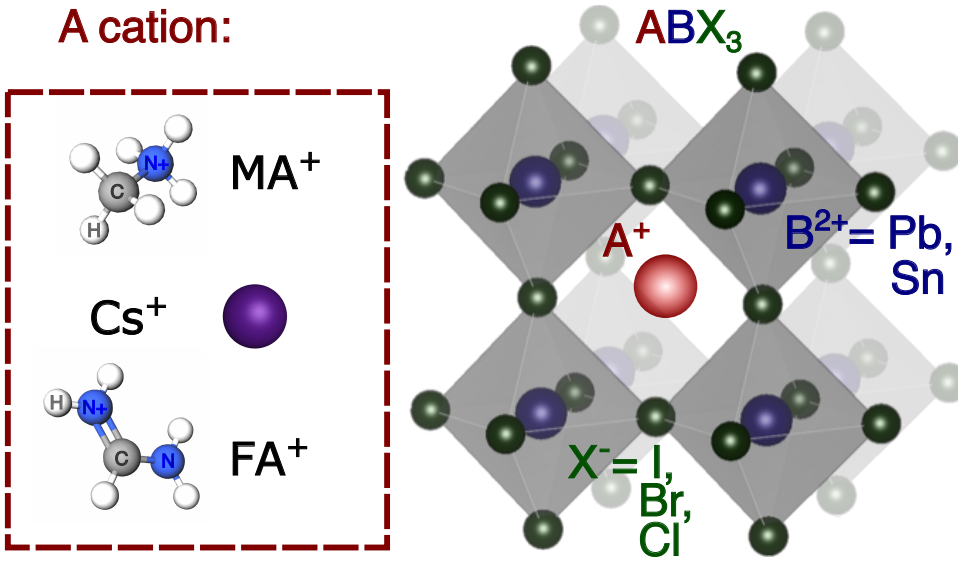


Figure 2.1: The ABX_3 structure of metal-halide perovskites incorporates a large molecule or atom (MA^+ - Methylammonium, FA^+ - Formamidinium, Cs^+- Caesium) on the A-site, a metal cation on the B side, usually lead (Pb^{2+}) or tin (Sn^{2+}), and a halide on the X site - iodine (I^-), bromine (Br^-) or chlorine (Cl^-).

be determined using a Goldschmidt factor α [22], defined in terms of the radii of the

different ionic species in the crystal ($R_{\mathrm{A,B,X}}$),

$$\alpha = \frac{R_{\mathrm{A}} + R_{\mathrm{X}}}{\sqrt{2}(R_{\mathrm{X}} + R_{\mathrm{B}})} \,. \tag{2.1}$$

For metal-halide perovskites, the Goldschmidt factor in the range $0.8 < \alpha < 1$ was generally found to result in stable perovskite structures [23], although the rule cannot be used reliably due to the complicated shape of the organic molecules in perovskite structure. Due to the thermal and chemical instability of the MA molecular cation [24], it is beneficial to use the more stable FA or Cs ion on the A-site to improve the lifetime of the perovskite material. However, due to the yellow delta phase formation when using just the FA molecule [25], and the small size of a Cs atom leading to the Goldschmidt factor lying outside the preferable range, a mix of these cations has to be used to obtain thermally and structurally stable crystals [24].

The ease of fabrication of metal-halide perovskite through solution processing allowed for a full exploration of the effect of compositional substitution on the properties of these semiconductors. Most notably, bandgap tuning can be achieved through halide substitution, with pure iodine-based perovskite having the most redshifted absorption onset in the infrared regime, mixing iodine and bromine can blueshifts the absorption to the visible part of the spectrum and adding chloride can further push the bandgap onset of the semiconductor towards ultraviolet wavelengths [26–28]. Also, mixing lead with tin on the metal site in the structure leads to a bandgap bowing effect where the absorption onset of the mixed metal perovskite is more redshifted than of tin-only or lead-only semiconductor [21]. The relatively simple bandgap tuning in perovskite semiconductors can have its application in the development of light sources such as light-emitting diodes (LED) and lasers. It can also be exploited in photovoltaics to achieve optimal bandgap for the absorption of sunlight or artificial lighting in indoor applications, or in tandem solar cells where multiple layers of active materials are combined to increase the efficiency of the PV device [29].

2.1.2 Optoelectronic Properties

Apart from the ease of processing and bandgap tunability, metal-halide perovskites exhibit fantastic optoelectronic properties making them highly suitable for applications in photovoltaics, radiation detection, light emission and other semiconducting devices. These materials exhibit band charge-carrier transport, which means the electrons and holes in the conductive state are delocalised and have relatively high mobility when compared with organic semiconductors [30, 31]. The high mobility implies efficient charge-carrier extraction and injection of carriers in PV devices and light source applications, respectively.

Also, the direct bandgap of metal-halide perovskites ensures a high absorption coefficient and efficient radiative emission, also important for photovoltaics. Employing these materials allows for very thin layers (hundreds of nanometers) to be used to efficiently absorb all of the solar light [32], in contrast to indirect-bandgap silicon solar cells which require a thick layer of the active material to effectively capture the solar energy [33].

Moreover, a low exciton binding energy, comparable to the thermal energy at room temperature, results in the vast majority of photons absorbed by the semiconductor being converted to mobile free carriers rather than charge-neutral excitons [34–36]. Such high photon-to-carrier conversion rate simplifies the charge extraction in perovskite solar cells compared to organic semiconductor photovoltaics, where special efforts have to be made to dissociate the strongly-bound excitons [37].

Finally, the defect chemistry of metal-halide perovskites leads to the high resistance of these materials to detrimental effects of defects in the crystal structure, and hence the long lifetimes of the free charge carriers [38].

The relatively long lifetime and high electrical mobility of charge carriers are essential for obtaining efficient PV devices, since the photogenerated electrons and holes must be able to travel through the whole thickness of the active layer within their lifespan. A good measure of their ability to do so is the diffusion length, the average distance free carriers will

diffuse by within their lifetime in the absence of an externally applied electric field [39]. The diffusion length L_{diff} depends on the electrical mobility μ and the lifetime of carriers τ as

$$L_{\text{diff}} = \sqrt{\frac{\mu \tau k_{\text{B}} T}{e}}, \tag{2.2}$$

where $k_{\text{B}}T$ is the thermal energy of the carriers and e is the electron charge. Thanks to high mobility and long charge-carrier lifetime, perovskites exhibit very long (microns) diffusion lengths, well above the average thickness required for solar cells (hundreds of nanometers) [40].

2.1.3 Defects

In conventional silicon photovoltaic technology, extreme care has to be taken to avoid defects in the semiconductor. A missing or misplaced atom in the crystal structure leads to a local energy minimum which traps free carriers and induces substantial non-radiative recombination losses, significantly reducing the optoelectronic performance of the material [41]. However, in metal-halide perovskites, this mechanism does not appear to have as detrimental effect on the optoelectronic properties of the crystal [42]. Since such point defects can have a wide range of effects on the behaviour of the semiconductor, defect chemistry in metal-halide perovskites has been extensively investigated in recent years [38, 43–47].

Multiple point defects can occur in a perovskite ABX_3 structure - a vacancy of one of the elements labelled V_A, V_B or V_X, a misplacement, or interstitial of the atom from its prescribed site (A_i, B_i or X_i) or substitution of one atom Z with another Y, labelled Y_Z. Often, these defects come in pairs, called Frenkel pairs- for example, iodine misplaced from its original site can create iodine vacancy V_I and iodine interstitial I_i, which ensures charge neutrality in the case of charged defects. Whether any given defect will or will not be formed depends on the formation energy of that defect [43]. The lower the formation energy, the more abundant the defect will be in the structure and therefore the more

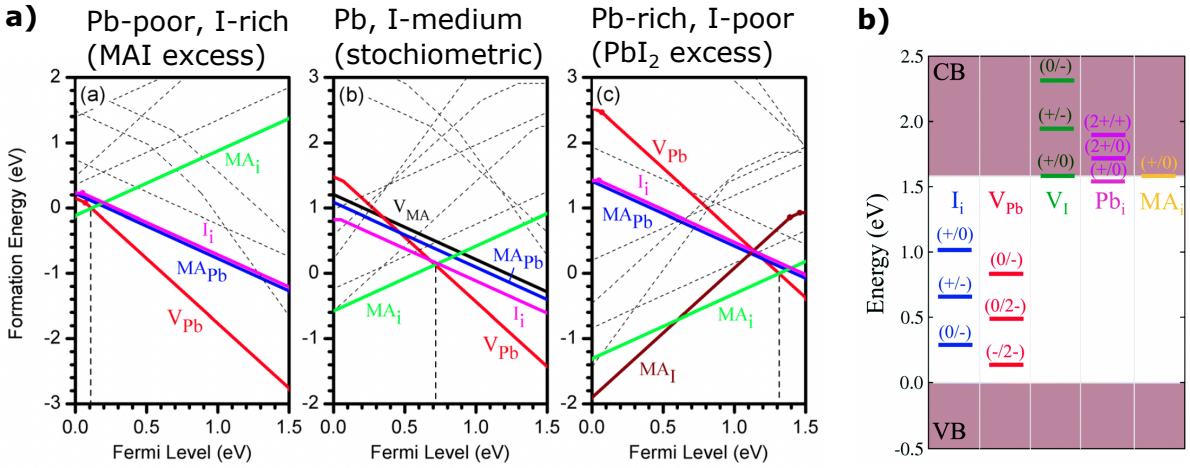


Figure 2.2: a) The formation energies of selected defects under various synthesis conditions of $MAPbI_3$ perovskite. Solid lines indicate the evolution of the formation energy of defects most easily formed and grey lines show the formation energies of other, less common defects. b) The energy levels of the point defects in this material represent the potential energy gain of a charge carrier captured by these traps. Figure a) reprinted from [38], with the permission of AIP Publishing, figure b) reprinted from [44] with the permission of RSC Publishing.

detrimental effect it could have on the performance of the semiconductor. The formation energy can sometimes be controlled by the deposition conditions of the crystal - an excess metal added during the deposition process can reduce the number of metal vacancies formed but could lead to an increased density of metal interstitials [38, 48]. This is illustrated in Figure 2.2a for $MAPbI_3$ perovskite, where the formation energies for most abundant defects are shown for three different deposition conditions. As the ratio of MAI:PbI_2 changes in the precursor solution, the chemical potential of these components shifts, affecting the formation energies of some defects. Notably, the lead vacancy is less likely to form (higher formation energy) when excess PbI_2 is introduced, due to the excess of metal ions in the precursor solution.

One of the effects of the defects in a semiconductor is charge-carrier scattering. In a simple Drude model of conductivity, the time evolution of the momentum $\mathbf{p}$ of a particle with charge q is affected by the externally applied electric field $\mathbf{E}$ and the scattering events - interactions of the particle with a scattering centre such as ion, phonon, or

defect, which randomise the momentum of the charged particle,

$$\frac{d\mathbf{p}}{dt} = q\mathbf{E} - \frac{\mathbf{p}}{\tau_s}\,. \tag{2.3}$$

Here, τ_s is the average time between scattering events, and for a particle with mass m, the steady-state solution of Equation 2.3 yields the average drift velocity v_d,

$$v_d = \frac{q\tau_s}{m}E \equiv \mu E\,, \tag{2.4}$$

where the charge-carrier mobility $\mu \equiv \frac{q\tau_s}{m}$ is defined as the ratio of drift velocity and electric field strength [49]. According to Equation 2.4, the more scattering events a charge carrier undergoes, the lower its average drift velocity and therefore the lower its electronic mobility. The drop in mobility in defect-rich perovskites has been confirmed experimentally [47, 50, 51] and is a strong motivation for an overall reduction of the defect density through a carefully designed deposition process to avoid the worsening of charge extraction in PV devices.

However, not all defects have exactly the same effect on the optoelectronic properties of a semiconductor. Apart from scattering the charge carriers, defects can create local energy minima, leading to strong non-radiative recombination through carrier capture and a reduction of charge-carrier lifetime [47]. This effect would depend on the exact energy levels formed, which vary between different defects, as shown in Figure 2.2b, also for $MAPbI_3$ [44]. In the figure, the calculated energy levels are shown for selected point defects in different oxidation states, with the conduction band (CB) and valence band (VB) labelled on the energy scale set to 0 at the top of the valence band. As can be clearly seen in the figure, only some of the point defects lead to the formation of energy states deep in the bandgap of the semiconductor. As explained by Motti et al. [43], the lead vacancy and halide interstitial will have the most detrimental effect on the optoelectronic performance of lead-halide perovskite, by selectively capturing free electrons leading to

nonradiative carrier recombination. Other common defects, including iodine vacancies as well as MA and lead interstitials, will not cause a significant reduction to free carrier lifetimes due to their energy levels lying very close to or within the conduction band. The very small energy gain an electron can experience by localising on those point defects can be easily overcome by the thermal energy at room temperature.

Finally, apart from affecting the free carriers, the presence of point defects influences the Fermi level of the semiconductor [48]. An intrinsic semiconductor, where thermally-excited populations of free electrons and free holes balance each other, will have the Fermi level placed precisely in the middle of the band gap. However, introducing energy states of defects into the semiconductor will change the position of the Fermi level, making the semiconductor positively (p-type) or negatively (n-type) doped. A large pool of point defects with various oxidation states existing in lead-halide perovskite allows for a compensation effect, where both hole-donating (acceptor)-type defects (eg. lead vacancy) and electron-donating (donor) defects (eg. MA interstitial) are formed, offsetting each other's effect on the Fermi level position [38]. This compensation can result in an intrinsic semiconductor, an example of which is $MAPbI_3$ deposited under stoichiometric conditions, as indicated by the middle graph in Figure 2.2a - the formation energies of acceptor and donor-type defects roughly equalise for Fermi level in the middle of the band, reaching an equilibrium of defect formation and lack of further shifts of Fermi level. By contrast, when MAI excess is used (left graph in this figure), the Fermi level placed in the middle of the bandgap makes the hole-donating defect formation (such as lead vacancy and iodine interstitial) much more favourable, leading to an increase in the density of these point defects and hence a lowering of the Fermi level until a new equilibrium is reached, in this case resulting in a slightly p-doped semiconductor [52].

2.2 Doping of Metal-Halide Perovskites

Many semiconducting devices rely on the ability to electrically dope the semiconductor. P-N junctions (interfaces of p-doped and n-doped semiconductors) are used to make diodes and transistors and P-I-N structures (p-doped–intrinsic–n-doped) result in efficient photodetectors and solar cells made of conventional semiconductors, eg. silicon [53]. Typically, doping is achieved by intentionally introducing impurities into the crystal structure. Boron (3 valence electrons) and phosphorus (5 valence electrons) are typically used to replace some of the silicon atoms (4 valence electrons) to achieve electron deficiency (p-type doping) or excess (n-type doping), respectively. Relatively straightforward methods like ion implantation (accelerating dopant ions in an electric field and shooting them into a silicon wafer target) are most often used to introduce the dopant into the structure, providing control over the spatial distribution and density of dopants [54]. Additionally, the rigid structure of silicon prevents the impurities from migrating, ensuring the lasting and localised effect of doping.

This simplicity of electrical doping cannot be directly transferred from the field of conventional semiconductors to metal-halide perovskites. The complicated defect chemistry described above leads to a compensation effect which reduces the effectiveness of extrinsic doping of these materials. Solvent-based processing enables a simple way to introduce new ion species into the precursor solution, but it also requires the new elements to be accompanied by other ions in form of salts, complicating the perovskite formation chemistry and introducing unwanted effects. Moreover, the soft, ionic structure of metal halide perovskites can result in any attempts of extrinsic doping being unsuccessful. The low barrier to ion migration can result in the dopant ions travelling throughout the perovskite film, especially in the presence of a built-in electric field, such as in a solar cell [55].

Nevertheless, attempts at extrinsic doping have been extensively reported in the literature, due to the substantial potential reward of successfully achieving doping and the formation of stable homojunction (interfaces of the same semiconductor with opposite-sign doping) [56–61]. A perovskite P-N junction would alleviate the need for electron- and hole-transport layers (ETL, HTL) in photovoltaic cells, which are currently necessary for the efficient extraction of charge carriers under solar illumination but suffer from poor transport properties and band alignment, which limits the achievable performance of perovskite solar cells [62].

It is worth noting that the term "doping" can be used to describe different processes in metal-halide perovskite literature. In the field of inorganic semiconductors, doping usually implies the addition of a very small number of impurities into the lattice, which introduces additional electrons or holes to the bands of the semiconductor. Therefore, the terms "electrical doping" (addition of charges) and "impurity doping" (addition of ion species normally not present in the structure) can be used interchangeably [53]. However, due to the complicated defect chemistry of metal-halide perovskite, electrical doping can occur spontaneously through point defect formation [21], and the introduction of foreign ions might not lead to any change in electrical conductivity due to the compensation effect [50]. Additionally, the term "chemical doping" can be used to indicate partial substitution of ions in the structure, even when relatively high concentrations of these ions are used [63], which would normally be termed "alloying" in the field of conventional semiconductors [64]. Section 2.2.1 describes the efforts made in the field of metal-halide perovskites to achieve electrical doping through the substitution of the metal cation with heterovalent ions (ions with different numbers of valence electrons). This chemical doping can sometimes result in slight electrical doping, but more often leads to changes in material properties by affecting the defect formation chemistry in the semiconductor [48]. Section 2.2.2, on the other hand, discusses spontaneous electrical hole doping in tin-halide

perovskites, which stems from tin-vacancy defect formation [21]. This kind of electrical doping is not associated with adding dopant impurities into the perovskite structures.

2.2.1 Heterovalent Doping

The first report of successful heterovalent extrinsic doping in lead-bromide perovskites appeared in 2016 [57], when Abdelhady et al. incorporated ions of Bi^{3+}, Au^{3+} and In^{3+} into the perovskite structure, expecting a substitution of lead ions (Pb^{2+}) on the metal site. Although a very high density of the impurities was incorporated into the single crystals of $MAPbBr_3$, about $10^{19}\,cm^{-3}$ for the case of bismuth ions, the achieved free carrier concentration was 7 orders of magnitude lower ($10^{12}\,cm^{-3}$), proving that the complicated defect formation chemistry and compensation effect from intrinsic defects can invalidate the approach used in the field of inorganic semiconductors to achieve electrical doping when applied to metal-halide perovskite materials.

The full extent of the influence of extrinsic doping on the optoelectronic properties had to be still investigated, especially as Bi^{3+} doping appeared to significantly affect the bandgap of the perovskite hosts, leading to hopes of a straightforward bandgap engineering method [57, 65] but also inducing controversy in the field [66–68] over the validity of this approach. Moreover, understanding what mechanisms led to the compensation of the n-doping expected from bismuth incorporation could potentially result in improved heterovalent doping techniques. These unresolved questions led to the study presented in Chapter 6 of this thesis being conducted [50], which investigated the effects of bismuth chemical doping on the properties of $MAPbBr_3$ thin films. The enhancement of bromide interstitial formation was concluded by investigating charge-carrier trapping dynamics, which would explain the charge compensation effect and low efficiency of n-doping through bismuth addition. A lack of bandgap tuning was also observed, instead attributing the previously reported redshift of absorption onset to an energetic disorder induced by doping.

Further investigations of heterovalent chemical doping in lead-halide perovskites employed indium doping [69, 70], which was shown to slightly improve the performance and stability of the perovskite solar cells by improving the crystal growth of the perovskite and increasing the absorption strength of the active layer. No effect on the electronic doping levels was reported though, likely due to the compensation effect in perovskites. Monovalent thallium and silver (Tl^+, Ag^+) were also incorporated into perovskite structure, enhancing the PCE of perovskite-based PV devices and showing effects of p-type electrical doping [59, 71]. However, a detailed investigation of the exact contribution of the p-type dopants to the conductivity of the perovskite semiconductor and the efficiency of this type of doping is still lacking. N-type doping levels as high as $10^{17}cm^{-3}$ also has been demonstrated experimentally through trivalent antimony (Sb^{3+}) addition [72], although the same research indicated similar electron densities in the undoped perovskite films.

Overall, to date, no reliable method of electrical doping of perovskite semiconductors has been demonstrated by heterovalent ion incorporation. Electronic doping levels achieved by this route have not exceeded significantly the majority carrier densities obtained in undoped perovskites, indicating that the intrinsic defect formation currently has the most influence on the Fermi level and free-carrier density in the final perovskite material [48].

2.2.2 Tin-Halide Perovskites - Self Doping

As mentioned in Section 2.1.3 of this chapter, intrinsic point defects can lead to the electrical doping of perovskite semiconductors and a shift of the Fermi level away from the middle of the band gap. In lead-based $MAPbI_3$, the sign of the doping can be controlled through the deposition conditions, as shown in Figure 2.2 and described in reference [38]. However, in its tin-based counterparts (tin-halide perovskites), the control of the deposition process has little influence on the type of majority carriers. As described by

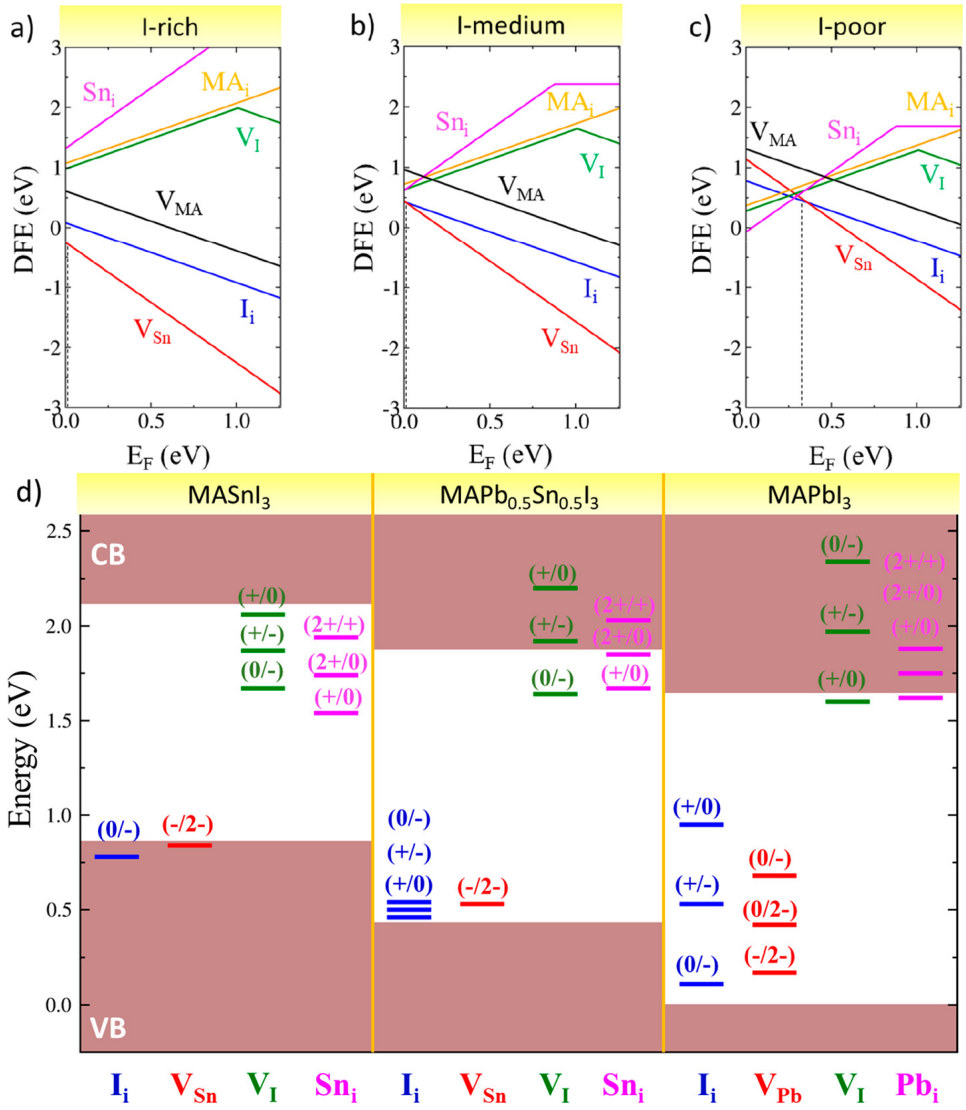


Figure 2.3: The formation energies of selected defects in $MASnI_3$ perovskites under various synthesis conditions (a- iodine rich, tin poor, b-stoichiometric, c-iodine poor, tin rich). d) Energy levels of the point defects in $MASnI_3$, mixed tin-lead $MASn_{0.5}Pb_{0.5}I_3$ and lead-based $MAPbI_3$, showing the relative positions of the defect energy levels with respect to the bands. Figures adapted with permission from [46]. Copyright 2023 American Chemical Society.

Meggiolaro et al. [46] and shown in Figure 2.3a and b, the defect formation energy of hole-donating tin vacancies and iodine interstitials in $MASnI_3$ perovskite is significantly lower than that of any other defects. The low formation energy, together with the propensity of tin to form compounds with oxygen and iodine in its more stable Sn^{4+} oxidation state than that occurring in the perovskite structure (Sn^{2+}) [73], results in a significant density of tin vacancies and the concomitant hole doping observed in tin-halide

perovskites [74–76]. The formation energies of the compensating defects, such as iodine vacancy and MA and tin interstitials are significantly higher than those of the p-dopants, which results in the Fermi level being shifted into the valence band of the semiconductor, explaining its metallic properties and high conductivity [77]. Figure 2.3c indicates that by using high SnI_2 excess during deposition, Fermi level within the bandgap can be achieved, although the semiconductor remains p-doped [46].

Theoretical predictions of tin vacancy formation and hole doping have been extensively confirmed in the literature. High conductivity originating from self-doping has been well understood for over a decade [77], and recent developments in novel deposition methods confirmed that increasing the density of tin ions in the precursor solution results in a lowering of the tin vacancy formation and p-type conductivity of these materials [75, 78]. However, completely eliminating or compensating for the acceptor defects in tin-halide perovskites remains elusive with the lowest reported density of holes being around 10^{17}cm^{-3} [79], much higher than the density of photoexcited charge carriers under solar illumination ($10^{15}\text{cm}^{-3} - 10^{16}\text{cm}^{-3}$) [80].

An interesting comparison can be made between lead-based and tin-based perovskites in terms of the energy levels created by the intrinsic defects formed in the crystals. The energy levels of most common defects calculated by Meggiolaro et al. [46] are shown in Figure 2.3d and include calculations done for $MASnI_3$, $MASn_{0.5}Pb_{0.5}I_3$ and $MAPbI_3$. In lead-based perovskites, metal vacancies and halide interstitials are the main drivers of non-radiative charge-carrier recombination, due to their energy levels lying in the middle of the band gap, providing large energy gain for electrons to localise at the defect sites and subsequently recombine with free holes. However, in tin-based perovskites, the same point defect states are located within the valence band of the semiconductor, “trapping” electrons (releasing free holes) from the valence band (to the band) and not contributing to the nonradiative recombination of photoexcited charge carriers [46]. Although the

energy gain from localising at those defects is very small (smaller than thermal energy at room temperature), these defects can still scatter free carriers, reducing their mobilities. A "middle ground" is achieved in mixed lead-tin perovskites (middle graph of Figure 2.3d), where the position of band edges with respect to the point defect levels results in only weak doping (p-type semiconductor without the metallic properties of $MASnI_3$), and relatively shallow traps. This could explain the relatively long photoexcited charge-carrier lifetimes observed for compositions similar to $MASn_{0.5}Pb_{0.5}I_3$ across the literature [21].

Practically, the level of doping in tin-containing perovskites can be tuned from heavily p-doped to moderately p-doped by controlling the density of tin ions in the precursor solution - this is usually done by adding SnF_2 or metallic tin to the precursor [75, 78, 81]. Further reduction of the dopant density currently can be only achieved through alloying tin with lead on the metal ion site, which at the same time reduces the amount of tin in the final crystal (decreasing the number of possible tin vacancies) and lowers the valence band energy such that the process of donating holes to the valence band is less efficient [46, 51]. Moving across the compositional range from tin-only perovskite, through mixed tin-lead to lead-only eventually results in an intrinsic semiconductor (eg. $MAPbI_3$ deposited in a stoichiometric environment) being formed. On the other hand, in order to achieve higher amounts of hole doping in tin-halide perovskite, the deposition can be performed under stoichiometric, or tin-poor conditions [82]. Moreover, exposing tin-iodide perovskite to oxygen has proven to increase further tin-vacancy abundance, eventually leading to the formation of vacancy-ordered perovskite (a perovskite-like structure where every second tin ion is missing) [47].

The propensity to hole self-doping, together with readily available methods of significant doping reduction, make tin-halide perovskite a perfect system to investigate the possible effects of successful electronic doping on other perovskite semiconductors. Chapter 5 investigates such effects of doping on the charge-carrier cooling dynamics,

assessing the applicability of doped perovskites for future-generation hot-carrier solar cells, and finding that hot-carrier interactions with cold holes can rapidly disperse the energy of the hot carriers in tin-iodide perovskites [83], reducing the chance of successful hot-carrier extraction, as explained in following Section 2.3 of this chapter.

2.3 Hot-Carrier Solar Cells

In order to produce an efficient photovoltaic device, most of the energy of photons incident onto the solar cell must be converted to electrically usable power, i.e. a current of charge carriers flowing through a load. However, employing semiconductor technology cannot offer a 100% conversion rate due to the inherent limitations of light–semiconductor interactions [84, 85]. Figure 2.4a shows the two fundamental loss mechanisms in a single-layer solar cell operating under thermodynamic equilibrium. Due to the existence of a band gap in a semiconductor, a range of energies an electron is not allowed to have, photons with energies too low to excite charge carriers across the gap cannot be absorbed by the active material, as shown by process 1. The second biggest loss is related to charge-carrier cooling. Photons with energies larger than the bandgap of the semiconductor will excite electron-hole pairs deeper into the bands, providing the newly generated charge carriers with more kinetic energy. However, through interactions with the lattice, this excess energy is quickly dissipated in the form of phonons (heat) until the temperature of the charge-carrier gas equalises with that of the lattice. This process of charge-carrier cooling is shown in Figure 2.4a as process 2, both in a form of a cartoon of a single electron losing its excess energy and as the evolution of the Maxwell-Boltzmann distribution from hot to cold [86]. Figure 2.4b shows the spectrum of sunlight, highlighting how these losses affect the maximum power output of a solar cell made with $MAPbI_3$ active layer. Although transmission losses (unabsorbed photons) can be reduced by using lower bandgap materials, higher losses would be induced by

charge-carrier cooling. Balancing these two loss pathways results in the optimal bandgap of 1.34eV providing the highest theoretical power conversion efficiency of 33.16% [85]. For a perovskite material with a bandgap of 1.5eV, the same calculation yields the maximum theoretical efficiency of 32% PCE [11].

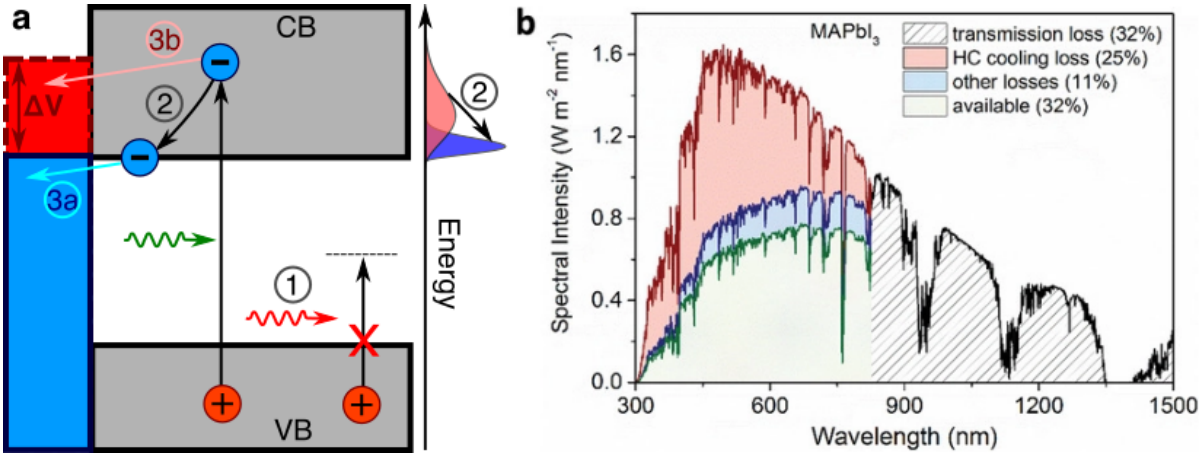


Figure 2.4: a) A simplified diagram of fundamental power losses in a single-layer solar cell with conduction band (CB) and valence band (VB) labelled. The loss of photons with sub-bandgap energy (transmission loss) is shown as process 1 and the hot-carrier cooling is shown as process 2. The carrier extraction of cold carriers (3a) and hot carriers (3b) is shown and ΔV represents the open circuit voltage gain possible to achieve through hot-carrier extraction. b) The solar spectrum is shown with the visualised losses marked for a $MAPbI_3$-like semiconductor, including transmission loss shown as grey shading, hot-carrier cooling loss in red and other, relatively small thermodynamic voltage losses in blue. Figure b) reprinted from [11] with the permission of John Wiley and Sons.

2.3.1 Overcoming the Thermodynamic Limit

Theoretically, the charge-carrier cooling losses could be avoided if the carriers were extracted before the transfer of kinetic energy to the lattice occurs, i.e. when the solar cell operates not in thermal equilibrium [12]. As Figure 2.4a indicates, such hot-carrier extraction (process 3b) could be implemented by using a selective contact with a higher work function than that used in cold-carrier extraction (3a), resulting in higher achievable open-circuit voltage and therefore higher efficiency of the solar cell. This simplified dynamic picture is often used to describe the principle of operation of hot-carrier solar cells but it does not represent well the steady-state condition under solar illumination.

The generation of charge carriers with different amounts of kinetic energy, as well as the transfer of the excess energy to the lattice, occurs simultaneously and continually, reaching an equilibrium state in which some temperature of the lattice T_{L} and a different temperature of the charge-carrier gas T_{cc} is established [87] (these are described by the two-temperature model developed by Anisimov et al. [88]). The temperature of the lattice is set by balancing the dissipation of energy into the environment with the heating from the low-energy photon absorption and hot-carrier cooling processes. The temperature of the charge-carrier gas is on the other hand dependent on the details of the energy extraction and the rate at which the energy can be transferred into the lattice (which in turn depends on electron-phonon coupling and the thermal capacity of the lattice). In the limit of this energy transfer occurring instantly, the temperature of the carrier gas will be equal to that of the lattice, $T_{\mathrm{cc}} = T_{\mathrm{L}}$, close to 300K under regular operating conditions [89]. If the energy transfer is very slow and inefficient, the temperature of the carrier gas will be larger than that of the lattice $T_{\mathrm{cc}} > T_{\mathrm{L}}$ and it will depend on the rate of energy extraction from the system either through carrier extraction or charge-carrier recombination.

Under such conditions of slow hot-carrier cooling, the high temperature of carrier gas leads to the formation of the free charge-carrier population with Maxwell-Boltzmann distribution. The high-energy carriers in the tail of this distribution can be extracted by suitable contacts high above the bandgap. The hot-carrier extraction was calculated to enable a very high power conversion efficiency of 66%, significantly increasing the achievable power output of single-layer cells, as fully described by Ross and Nozik in Reference [12]. Such high efficiency would be achieved by completely thermally isolating the hot-carrier gas from the environment (most importantly by removing charge-carrier cooling through interaction with the lattice), and extracting the carriers at potential energy of 4.2 eV in a semiconductor with bandgap energy tending to 0 (since the hot-carrier cooling losses are removed, narrowing the bandgap assures higher photon absorption

rate). Under these conditions, the temperature of the hot-carrier gas would reach 3600 K. In order to unlock the potential of this future-generation PV technology, it is crucial to identify semiconducting materials with relatively long charge-carrier cooling times or find suitable operational conditions under which energy exchange of hot carriers with the lattice is highly inefficient [11].

2.3.2 Charge-Carrier Cooling in Lead-Halide Perovskites

The first reports of hot-carrier cooling dynamics in lead-halide perovskites came in 2013 when by using transient-absorption (TA) spectroscopy, the researchers found that following photoexcitation, hot charge carriers relax to their respective band edges in about 0.4 ps [90]. Although insufficiently slow for achieving hot-carrier technology, such cooling dynamics were longer than those observed in organic semiconductors [91, 92], triggering a large amount of research into hot-carrier relaxation in lead-halide perovskites [11].

An important discovery was that of a very slow charge-carrier cooling reaching hundreds of picoseconds duration, occurring at high excitation densities [93]. This is summarised in Figure 2.5a-d, which shows that after the photo-excitation with a high-fluence, above-bandgap photon energy laser pulse, the high-energy photon absorbance is reduced due to hot carriers occupying energy levels deep in the bands. As time progresses, this high-energy tail of the above bandgap absorbance bleach decreases and the bandgap bleach (reduced absorbance at the photon energy equal to the bandgap) increases, as is expected from charge carriers relaxing to the band edges following the cooling process. Figure 2.5a shows the full evolution of the transient absorption spectrum and Figure 2.5b shows the TA spectra at different delay times with the high-energy tail used for carrier temperature extraction (through Maxwell-Boltzmann distribution fitting) highlighted in red.

As explained by Yang et al. [93], the main pathway of hot-carrier cooling in metal-halide perovskites is hot-carrier–LO-phonon interactions, due to the strong coupling between electrons and longitudinal-optical phonons in polar ionic materials (because of the periodic changes in the dielectric constant of the material caused by these lattice vibrations) [94]. This mechanism leads to the loss of energy of hot carriers (dU/dt) according to

$$\frac{dU}{dt} = \frac{\hbar\omega_{\mathrm{LO}}}{\tau}\left(\exp(-\frac{\hbar\omega_{\mathrm{LO}}}{k_B T_e}) - \exp(-\frac{\hbar\omega_{\mathrm{LO}}}{k_B T_l})\right), \tag{2.5}$$

where τ is the scattering time of the electrons with phonons, $\hbar\omega_{\mathrm{LO}}$ is the energy of the phonon taking part in the hot-carrier cooling process, k_B is the Boltzmann constant and $T_{e,l}$ are the temperatures of the electron gas and the lattice, respectively. This model was successfully used to explain the temperature decay traces shown in Figures 2.5c and d, shown for various excitation photon energies (c) and excitation fluences (d).

Importantly, by fitting the hot-carrier–LO-phonon cooling model to data, the researchers found that the electron-phonon scattering time τ is independent of the excess energy of the hot carriers, leading to overall longer cooling times at higher excitation photon energies. This result is consistent with the theory of scattering of hot carriers off LO-phonons and confirms that this interaction is the dominating pathway of carrier cooling in lead-halide perovskites, which has been further confirmed by later investigations [95].

The second important realisation was that at high hot-carrier excitation density ($6 \times 10^{18}\,\mathrm{cm}^{-3}$) the dynamics of the charge-carrier cooling were significantly slowed down - by two orders of magnitude when compared with excitation density of $5.2 \times 10^{17}\,\mathrm{cm}^{-3}$. The increase in a charge-carrier cooling lifetime with the density of hot carriers was found to originate from the hot-phonon bottleneck effect - under high fluence excitation, so many phonons are released by the large ocean of electrons and holes during the cooling process that the phonon re-absorption process can be no longer neglected. The re-absorption of phonons heats up the carrier gas, artificially extending the cooling time observed in

the material. This first observation of the hot-phonon bottleneck effect in lead-halide perovskites indicated that an efficient hot-carrier extraction can be achieved if sufficiently high excitation densities are used. Many studies have since confirmed the presence of the hot-phonon bottleneck effect in metal halide perovskites [96–99].

However, in order for a hot-carrier solar cell to be developed, the long charge-carrier cooling dynamics have to directly translate to a higher temperature of the charge-carrier gas under steady-state conditions. Such continuous-wave evaluation of the temperature of the carriers is still lacking in the field, but the very recent investigation seems to broadly confirm the insights gained from time-resolved studies, concluding that at high excitation densities, one can achieve a build-up of high-energy electrons and holes in their bands [100]. Figure 2.5e shows the photoluminescence spectra emitted from $FAPbI_3$ thin films under strong continuous-wave illumination by a laser source. A blue shift of the PL, caused by hot-carrier emission, can be seen when the perovskite material is excited with light intensities hundreds of times greater than that of solar illumination. As can be seen from figure 2.5f, the carrier gas temperature of 500 K can be achieved under 400 Suns.

Overall, the current state of research suggests that in order to realise hot-carrier solar cells employing bulk lead-halide perovskite material, a higher-than-solar light intensity has to be used. Such intensities (hundreds of Suns) can be achieved in concentrator photovoltaics, where the solar illumination is focused onto the device using lenses or curved mirrors [101]. However, the thermal instability of metal-halide perovskites, especially at high light intensities, could potentially invalidate this approach [102–106], instead requiring reaching longer hot-carrier cooling times at lower excitation densities. These could be potentially achieved by reducing the dimensionality of the perovskite systems, for example by using perovskite nanocrystals, as some research has suggested [107, 108].

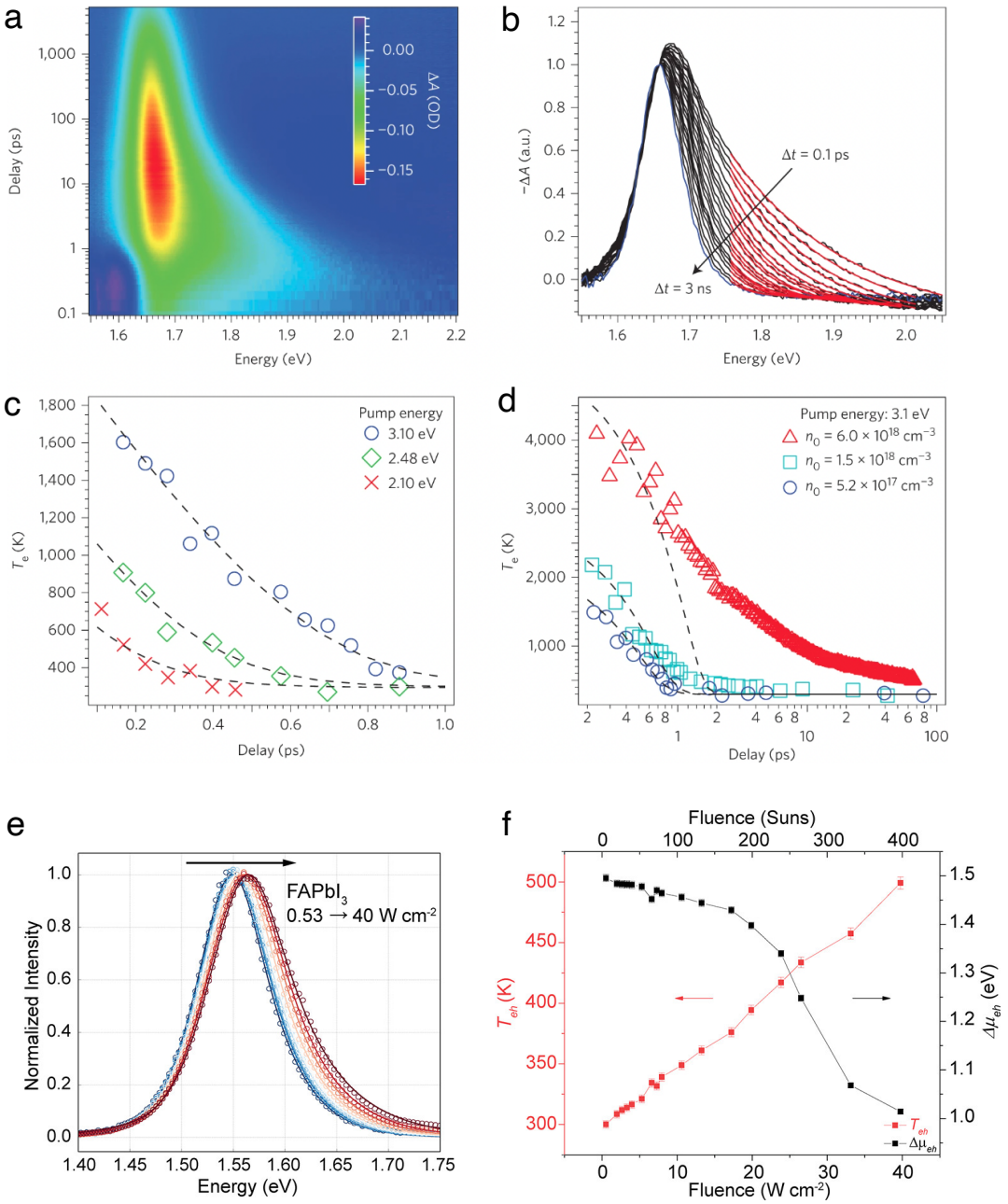


Figure 2.5: Summary of hot-carrier cooling dynamics in lead-halide perovskites. a),b) The transient absorption spectral traces show the rise of the bandgap bleach (just below 1.7eV) and decay of the high-energy tail following photoexcitation of $6 \times 10^{18}\,\mathrm{cm}^{-3}$ charge-carrier pairs with 3.1 eV laser excitation. c) The dependence of hot-carrier temperature evolution on photoexcitation photon energy and d) carrier excitation density, obtained by fitting spectra in panel b) with Maxwell-Boltzmann distribution in the region marked by red lines. Figures a)-f) reproduced with permission from Springer Nature from reference [93] and data was taken for $MAPbI_3$ perovskite thin films. e) Dependence of the spectral shape of steady-state photoluminescence on the excitation intensity and f) the calculated charge-carrier gas temperature (red) and Fermi level splitting (black) achieved under continuous-wave excitation for various excitation intensities in thin films of $FAPbI_3$. Figures e)-f) reprinted with permission from [100]. Copyright 2023 American Chemical Society.

2.3.3 Tin-Halide Perovskites - Hot-Carrier Relaxation

In the final section of this chapter, recent reports of charge-carrier cooling in tin-iodide perovskites are summarised. The differences between tin- and lead-based perovskites, including their thermal conductivity [109], charge-carrier mobility [21], phonon lifetimes [51] and doping levels [74, 75, 77] could all affect the efficiency of energy transfer from hot carriers to the lattice, potentially exhibiting higher suitability for hot-carrier PV.

Initially, a 2018 report indicated that extremely long hot-carrier cooling times can be achieved in $FASnI_3$ perovskites, reaching 6 ns at high excitation densities [110]. Such long charge-carrier cooling times were extracted from the high energy tail of photoluminesce spectra, attributed to hot-carrier emission. Fang et al. explained this observation by band filling (saturation of energy states close to the band edge) occurring in tin iodide perovskites at high excitation densities, combined with the hot-phonon bottleneck effect and Auger heating (re-heating of cooled carriers with the energy released by electron-hole recombination in a 3-body recombination process). Importantly, using steady-state photoluminescence data gathered with continuous-wave illumination, the researchers estimated that the impressive elevated charge-carrier temperature of 500 K can be achieved at illumination equivalent to 44 Suns, an order of magnitude lower than in lead-halide perovskites - see reference [100] and Figure 2.5f.

However, later research further investigated charge-carrier cooling in tin-iodide perovskites, finding that the extremely long-lived, but weak blueshift of photoluminescence could be related to the quality of the material affecting the energetic disorder in the $FASnI_3$ thin films [111]. A high level of energetic disorder combined with the band filling effect at high excitation density could result in some charge carriers remaining in the localised, high energy states, until they recombine radiatively on nanosecond timescales. Nevertheless, Savill et al. reported hot-carrier cooling lifetime of tens-of-picoseconds, at

relatively low excitation densities of $6.9 \times 10^{16} - 3.4 \times 10^{17} \mathrm{cm}^{-3}$, much longer than those reported in lead-based perovskites at similar hot-carrier excitation densities [11, 111].

Finally, some research suggested that the population of holes from the self-doping effect discussed in Section 2.2.2 could also influence the cooling dynamics in tin-iodide perovskites [112]. Kahmann et al. demonstrated that the treatment of the films aimed to decrease the tin-vacancy formation and p-type doping (used in both abovementioned studies of carrier cooling in $FASnI_3$) also led to a longer charge-carrier cooling time. This raised questions over the suitability of using the LO-phonon-mediated hot-carrier cooling model (by now well-established for lead-halide perovskites) to describe charge-carrier relaxation in tin-iodide perovskite. The study presented in Chapter 5 helps to answer this uncertainty by showing that for the low hot-carrier population density in highly-doped tin-iodide perovskite films, the charge-carrier cooling occurs mostly by interactions of hot carriers with the large ocean of cold dopant holes present in the crystal [83]. This research indicated that doping in tin-iodide perovskites could hinder their applicability for hot-carrier photovoltaics and has to be addressed to realise efficient hot-carrier extraction in this material.

2.4 Conclusions

An introduction to the field of metal-halide perovskite semiconductors has been so far provided in this thesis, describing their properties and explaining their high suitability for photovoltaic applications. The defect formation chemistry and energetics of trap states were discussed, showing their large effects on the optoelectronic performance of the semiconducting materials. The current state of research related to heterovalent doping was also presented, highlighting the need to investigate the influence of substitutional doping on defect formation and trapping dynamics in perovskite semiconductors. Further investigation of such effects is presented and discussed in Chapter 6, where the heterovalent

doping with bismuth is revealed to increase the bromide interstitials formation, leading to fast electron trapping and possibly to the previously-reported compensation effect where the n-type effect of bismuth inclusions is offset by the p-type halide interstitial formation.

This chapter has also explained the importance of defect formation chemistry in the context of tin-halide perovskites, a group of materials exhibiting metal-like behaviour due to tin-vacancy formation and the concomitant large p-type doping levels leading to their high conductivity. Such high conductivity, rarely achieved in thin-film semiconductors, can affect certain assumptions made when interpreting spectroscopic data, which often rely on a negligible optical thickness of the sample. Since the optical thickness depends not only on the physical thickness but also on the complex refractive index of the material, at high doping levels such assumptions can be invalid. Chapter 4 investigates this effect in detail in the context of data analysis of terahertz spectroscopy experiments (described in Chapter 3), developing new data analysis techniques relevant to investigations of optoelectronic properties of tin-iodide perovskites.

Lastly, the limitations of the single-layer photovoltaics were discussed in Section 2.3, providing a possible technique of improving solar cell efficiency by extracting charge carriers with excess thermal energy, high above the bandgap of the semiconductor. Such operation is only possible in semiconductors with very slow hot-carrier cooling dynamics, which significantly drives the search for such materials. The charge-carrier cooling in metal-halide perovskites also has been discussed, showing promising results of slow cooling at high hot-carrier densities, caused by hot-phonon bottleneck effect. Finally, limited research of hot-carrier cooling in tin-halide perovskites was presented, which indicated potential suitability of these semiconductors for hot-carrier PV. In the light of this limited research, Chapter 5 describes a study of the effect of doping on hot-carrier cooling in tin-iodide perovskites, proving that the hot-carrier–cold-carrier scattering events could be a limiting factor in the hot-carrier relaxation, highlighting the need

for doping suppression in tin-based perovskites if they were to be used in this highly efficient, next-generation photovoltaic technology.

3

Spectroscopic Techniques and Semiconductor Theory

Contents

3.1 Energy Levels and Absorption Spectroscopy 34
3.1.1 Experimental Implementation 37
3.1.2 Data Analysis 38
3.2 Radiative Transitions - Photoluminescence 41
3.2.1 Steady-State Emission 42
3.2.2 Time-Resolved Emission 42
3.2.3 Experimental Implementation 43
3.3 Charge-Carrier Dynamics 45
3.4 Terahertz Spectroscopy 48
3.4.1 Time-Domain Spectroscopy 49
3.4.2 Optical-Pump–THz-Probe 54
3.4.3 Pump-Push-Probe Spectroscopy 55

In this chapter, the experimental techniques used in Chapters 4, 5, and 6 are discussed together with the fundamental principles of their operation. Various spectroscopic methods were used to uncover the energetic structure, disorder and charge-carrier dynamics in the materials studied as part of the presented work. From measurements of absorption spectra to time-resolved ultrafast laser spectroscopy techniques, the methods presented in this chapter allowed for a detailed investigation of the physical phenomena

occurring in metal-halide perovskites.

3.1 Energy Levels and Absorption Spectroscopy

Measuring the electromagnetic radiation absorbed at various wavelengths of light allows for gaining an insight into the energetic landscape of the studied material. The amount of absorbed light depends on the probability of an electronic (or vibrational for the case of low-energy IR photons) transition occurring at the energy of the incident radiation, which in turn depends on the available energy levels, the density of states, and how close the energy of the incoming photon matches the energy of the transition [113]. The spectrum of the absorbed light can also reveal the broadening of the energy levels, which stems from the natural broadening (related to the lifetime of the state), thermal broadening (caused by a Doppler shift due to atom movement) and energetic disorder in the material (changes to the local energy of the transition caused by the structural or chemical inhomogeneity) [114].

In a semiconductor, the electronic wave functions of the individual constituent elements overlap and hybridise when the atoms are brought close together in a crystal structure [115]. Due to the interactions of the electrons, the individual energy levels split, which avoids violation of the Pauli exclusion principle [116]. When the number of atoms brought together is large (like in a semiconducting crystal), the spacing between the adjacent energy levels is negligible, which leads to the formation of bands - ranges of allowed energies for the electrons to have. In an intrinsic (undoped) semiconductor with negligible thermal energy, all the electrons occupy the lower-energy valence band, completely filling all available energy states in that band. However, when enough energy is provided, either thermally or through a photoexcitation, the electrons can overcome the energetic gap, referred to as a band gap, and be promoted to a (normally empty) conduction band. The availability of unoccupied higher energy states in the conduction band allows the

electrons to accelerate when an external force is applied, making them conductive [113]. A cartoon diagram of a band structure is shown in Figure 3.1, where the vertical axis represents energy and the horizontal axis - the momentum of electrons (although the absorption processes are drawn at arbitrary positions on the momentum axis). The break in energy between the valence (VB) and conduction (CB) bands represents the band gap of the semiconductor and the alignment of the extremes of the bands on the momentum axis indicates that this is a direct semiconductor (where an optical transition is allowed from top of the valence band to bottom of the conduction band). The band gap energy of a semiconductor is typically of the order of an electron-volt, corresponding to visible-to-near infrared light. When this energy becomes sufficiently large (a few eVs), the material is usually referred to as an insulator, although there are no fundamental differences between insulators and semiconductors [113]. After the promotion of the electron into the conduction band (represented by process 1 in Figure 3.1), an unoccupied energy state remains in the valence band. Nearby electrons feel the attraction force from this unoccupied energy level and can occupy it, causing an apparent movement of the vacant spot. This behaviour is equivalent to the unoccupied state being described as a positively charged particle with its mass determined by the energy-momentum dispersion in the valence band. Such a particle is commonly referred to as a hole, meaning that the promotion of an electron into the conduction band can be equivalently seen as a creation of a free charge-carrier pair that increases the conductivity of the semiconductor [115]. Furthermore, the electron and hole can form a bound, hydrogen-like state called an exciton (shown as process 2 in the same figure). The binding energy of the (weakly binding, Wannier-Mott) exciton will depend on the effective masses of the charge carriers and the dielectric constant of the surrounding material and its energy levels can be calculated in a similar fashion to a hydrogen atom. However, if the exciton is strongly bound and its radius is comparable to the atomic spacing in the crystal (Frenkel exciton),

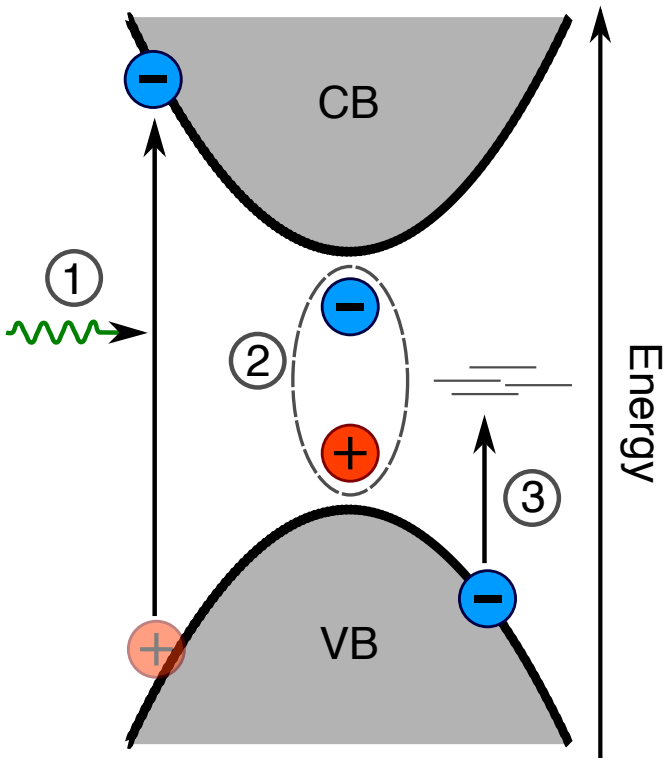


Figure 3.1: Simplified schematic of the band structure of a direct semiconductor, with the vertical axis representing energy and the horizontal axis - momentum. Absorption of a photon (1) leads to an optical transition of an electron from valence (VB) to conduction band (CB), resulting in the creation of a positively charged hole in the valence band. An exciton (2) can also be formed via the absorption of a photon with energy equal to the difference between the band gap energy and exciton binding energy. In some systems, it is also possible that mid-gap defect energy levels are accessible by a direct optical transition (3), increasing the absorbance of the material at that energy.

the dielectric constant is ill-defined and complex calculations have to be performed to estimate the energies of available states [115].

Finally, energy states associated with defects can sometimes be revealed in the absorption spectrum of a semiconductor [43]. A point defect is a local disturbance of the crystal lattice, where an atom is either missing or misplaced from its assigned location (as described in detail in the previous chapter). This can lead to a local variation of the energy landscape, resulting in the appearance of energy states within the bandgap of the semiconductor. These mid-gap states can enhance the charge-carrier localisation and can increase the scattering rate of the free carriers, reducing their electronic mobility. It is sometimes possible that a direct, optical transition exists between the defect state and the

valence band, which would be apparent as an increased absorption at the photon energy corresponding to that transition. This transition is shown as process 3 in Figure 3.1.

3.1.1 Experimental Implementation

The technique used to measure the absorption spectrum of a semiconductor in the ultraviolet-visible-infrared range depends on the properties of the material and the available sample preparation methods. For highly absorptive materials, such as metal-halide perovskites studied in this thesis, special care has to be taken when calculating the absorption coefficient, due to the limited amount of light transmitted through the samples and therefore low signal-to-noise ratio. For this reason, very thin films of the semiconductor (only hundreds of nanometers thick), deposited on top of transparent substrates have to be used to accurately measure the transmitted as well as reflected fraction of incident light as a function of wavelength. This approach of measuring the spectrum of light transmitted through and reflected by metal-halide perovskite thin films was used throughout this thesis to uncover the energetic landscape of these semiconductors, determining their bandgap, exciton binding energy and energetic disorder.

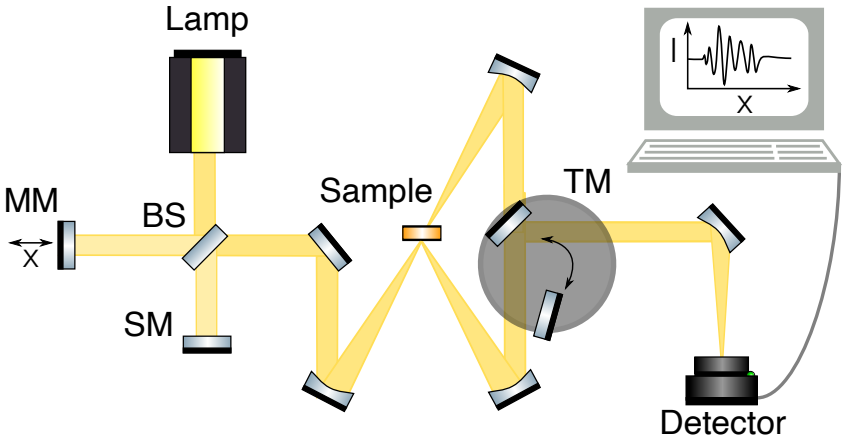


Figure 3.2: Schematic diagram of a Fourier-Transform IR spectrometer employing a tungsten filament lamp as an emission source. Michealson interferometer includes stationary (SM) and motorised mirror (MM) and a CaF_2 beamsplitter (BS). Turret with mirrors (TM) is used to choose between reflection and transmission mode and a silicon photodiode detector measures the light intensity interferogram used to calculate the spectrum.

The reflection-transmission spectra shown in Appendix A, as well as the absorption spectra shown in Chapter 6, were measured using a Fourier-Transform Infrared (FTIR) spectrometer (Bruker Vertex 80v) with a reflection-transmission attachment fitted. The simplified diagram of such FTIR spectrometer setup is shown in Figure 3.2. The light from a tungsten filament lamp is split with a CsF_2 beamsplitter (BS) into two arms of a Michelson interferometer, one with stationary (SM) and one with motorised mirror (MM). The recombined beam is focused onto the thin film sample and either the reflected or transmitted light is collected by mirrors on a motorised turret (TM) and re-focused onto a silicon photodiode detector. The motorised mirror is used to scan the optical path difference (x) between the arms of the interferometer and the intensity of the beam (I) is recorded by the detector. The interferogram can be then Fourier transformed into the spectral domain.

Reference measurements are performed by placing a silver mirror at the sample position to measure the "100% reflection" spectrum and an empty sample holder is used to measure "100% transmission". Since the setup used for the measurements presented in this thesis can only be used to measure the transmission and specular reflection, the scattering off the sample leads to light losses, which can appear in the measured spectrum as an artificially enhanced absorption. In Figure 6.1 in Chapter 6, the presence of such scatter was apparent for below-bandgap photon energies and so the absorption spectra were offset to 0 absorption below the bandgap.

3.1.2 Data Analysis

The measured reflected and transmitted spectra, together with reference measurements are used to calculate the absorption strength of the thin film. The reflection spectrum, $R(\nu)$, where ν is the wavenumber, is calculated as

$$R(\nu) = \frac{R_{\text{sample}} - R_{\text{empty}}}{R_{\text{mirror}} - R_{\text{empty}}}, \tag{3.1}$$

where the reflected spectrum measured for the empty sample holder, R_{empty}, is used as a background measurement and the mirror is assumed to reflect 100% of the incident light. Similarly the transmission spectrum, $T(\nu)$, is obtained from

$$T(\nu) = \frac{T_{\text{sample}} - T_{\text{mirror}}}{T_{\text{empty}} - T_{\text{mirror}}}, \tag{3.2}$$

since the mirror used as a reference does not transmit any light, meaning that any transmission recorded in that reference measurement is caused by light scattered inside the spectrometer.

Absorption Calculation

Together, the transmission and reflection spectra can be used to calculate the strength of the absorption in the form of the optical depth $OD(\nu)$ of the sample,

$$OD(\nu) = \ln\left(\frac{1 - R(\nu)}{T(\nu)}\right), \tag{3.3}$$

which can be related to the absorption coefficient as $\alpha = OD/d$, where d is the physical thickness of the thin film sample. The exact definitions of parameters used to describe absorption in semiconductors are a matter of convention and are aimed to recover the Beer-Lambert law, stating that the intensity of light I decays exponentially during propagation through a solid,

$$I(x) = I(0)\exp\left(-\alpha x\right), \tag{3.4}$$

where x is the distance of propagation and $I(0)$ is the intensity of light at the boundary of the sample. The convention used in this section accounts for the partial reflection of the incident light, $I(0) = I_{\text{incident}}(1 - R)$, and uses natural logarithm to describe the decay of light inside the sample, rather than base-10 logarithm. Other conventions include the use of optical density (also termed absorbance or decadic absorbance), which employs base-10 logarithm in a definition equivalent to Equation 3.3. Sometimes, the reflectance

of the material is also ignored in the definitions (i.e $R = 0$). It is important to note the convention used in a given publication since very often the terms "absorbance", "optical depth", "optical density" (defined above), and "absorption" (term without a rigorous mathematical definition) are used loosely and interchangeably with both base-10 and natural logarithms being commonly used.

Data Fitting

Finally, once the absorption is measured and calculated, a suitable model can be employed to account for the features present in the spectrum. In a semiconductor, a contribution of the continuum band-to-band absorption, as well as direct excitonic absorption, have to be included in the description of the spectra, as explained in this section. These are accounted for in the semiconductor absorption theory by Elliott [117], which was used to fit the absorption spectra presented in Chapter 6, Figure 6.1. In this model the energy (E) dependent absorption, $\alpha(E, E_\mathrm{g}, E_\mathrm{b})$, is described by a combination of contributions from bound excitons and electron-hole continuum states, involving the exciton binding energy E_b and band gap energy E_g:

$$\alpha(E, E_\mathrm{g}, E_\mathrm{b}) = \frac{b_0}{E}\sum_{n=1}^{\infty}\frac{4\pi E_\mathrm{b}^{3/2}}{n^3}\delta\left(E - \left[E_\mathrm{g} - \frac{E_\mathrm{b}}{n^2}\right]\right) + \frac{b_0}{E}\left[\frac{2\pi\sqrt{\frac{E_\mathrm{b}}{E-E_\mathrm{g}}}}{1-\exp\left(-2\pi\sqrt{\frac{E_\mathrm{b}}{E-E_\mathrm{g}}}\right)}\right] c_0^{-1}\mathrm{JDoS}(E) \tag{3.5}$$

where the joint density of states is given by $\mathrm{JDoS}(E) = c_0\sqrt{E - E_\mathrm{g}}$ for $E > E_\mathrm{g}$, and 0 otherwise, and the joint density of states constant $c_0 = \frac{1}{(2\pi)^2}\left(\frac{2\mu}{\hbar^2}\right)^{\frac{3}{2}} \times 2$, where μ is the reduced effective mass of the electron-hole system.

Broadening due to electron-phonon interactions, local fluctuations in the stoichiometry of the material, and energetic disorder is represented by convolution of $\alpha(E)$ with a normal distribution $N(0, \Gamma^2)$ which has mean 0 and standard deviation Γ. Unlike in the case of the modelling of absorption spectra of $MAPbI_3$ thin films reported previously

[114], a log-normal distribution was not additionally required to describe broadening in $MAPbBr_3$ perovskites studied in Chapter 6.

The Elliott function, $f_{\text{Elliott}} = \alpha(E, E_g, E_b) \otimes N(0, \Gamma^2)$, (where convolution is represented by the symbol $\otimes$) was fitted to the absorption onsets for the five samples shown in Figure 6.1 in Chapter 6 by a least-squares minimisation method, with E_g fitted globally across all samples. The resultant Elliott fits are shown in that figure in black solid lines and the extracted fit parameters are listed in Table 6.1 in the same chapter. Note: Elliott fitting was performed by Dr Adam D. Wright (Semiconductors Group, Department of Physics, University of Oxford).

3.2 Radiative Transitions - Photoluminescence

The emission from a semiconductor is a process inverse to absorption. As such, all three transitions shown in Figure 3.1 can occur in the opposite direction, leading to the emission of a photon with the energy matching that of the transition [118]. Additionally, radiative transitions can exist between the conduction band and mid-gap states which would normally be unoccupied prior to photoexcitation and therefore would not be revealed in the absorption measurements. Finally, the spectral shape of the emission is rarely similar to that of the absorption profile because of the dynamic processes occurring after the electrons are promoted to a higher energy state [119]. In order to minimise their energy, the electrons will relax nonradiatively to the lowest available state on a short timescale after excitation. This state can correspond to the bottom of the conduction band (relaxation through the charge-carrier cooling process) or the bound excitonic state (exciton formation), depending on the available thermal energy and exciton binding energy [118]. Moreover, in some systems, including bismuth-doped $MAPbBr_3$ discussed in Chapter 6, the electrons can relax to localised, mid-gap states (charge-carrier trapping) [50].

3.2.1 Steady-State Emission

The emission spectrum measured in the steady state (under continuous illumination) is typically dominated by the lowest available energy transition [119]. Examining the photoluminescence (PL) spectrum emitted from a semiconductor can hence give insight into the energetic landscape of the material complementary to that gained through an absorption measurement. PL spectrum can be used to, for example, identify the bandgap of the material [26] or to measure the charge-carrier gas temperature due to hot carrier emission [100]. It can also help to identify loss mechanisms in the investigated samples. As discussed in Chapter 6, a red-shifted emission could be indicative of the presence of low-energy defect states, which reduce the optoelectronic performance of the semiconductor. Such redshift in the steady-state PL could also reveal the funnelling of electrons into regions with lower bandgap, which occurs for example in mixed-halide perovskites. These materials undergo halide segregation, which leads to the formation of low-bandgap, iodine-rich regions in the crystal. The majority of photoexcited charge carriers funnels into those regions and emits lower-energy PL than expected from the bandgap of the fully-mixed phase. This effect is difficult to observe through measurements of the absorption spectra as these regions could constitute a small volumetric fraction of the sample [120].

3.2.2 Time-Resolved Emission

Additionally, dynamic processes can sometimes be probed via time-resolved photoluminescence measurements [119]. The changes in the intensity and spectral shape of the emission after the photoexcitation can reveal processes like charge-carrier cooling and recombination [111]. In the case of luminescent defects, like those uncovered in Chapter 6, the dynamics of the photoluminescence decay can provide insight into the nature of charge-carrier traps present in the material [50, 68].

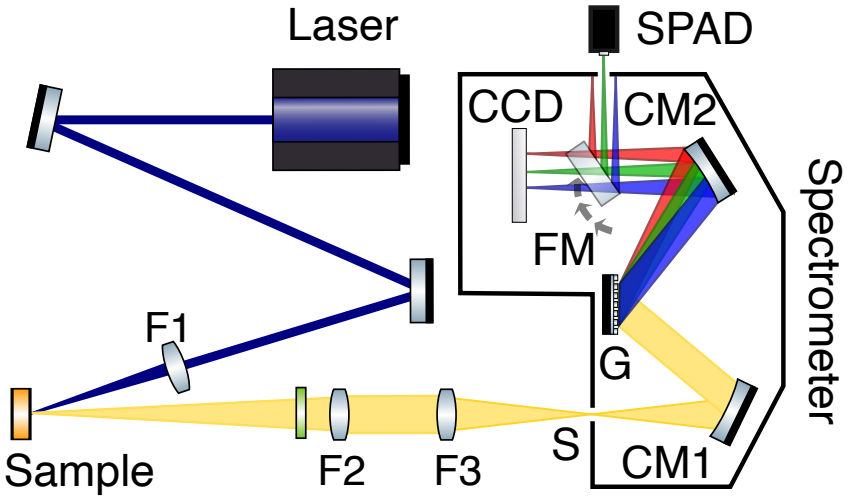


Figure 3.3: Photoluminescence measurement in a reflective geometry, including laser excitation source, spectrometer and collection and focusing optics (F2 and F3). Lenses, as well as spherical mirrors, have been used for PL collection in various systems listed in the main text of this section. Spectral filters were used to prevent the scattered laser light from reaching the spectrometer.

3.2.3 Experimental Implementation

Both steady-state and time-resolved photoluminescence data shown in Chapter 6 were measured in a reflection geometry. A simplified layout of such a PL measurement setup is shown in Figure 3.3. The photoexcitation laser beam is focused onto the thin-film sample using a lens (F1). The emitted light is passed through spectral filters to remove laser scatter (green rectangle) and collected by a collimating optic F2. The emission is then re-focused onto the slit (S) of the spectrometer with a lens (F3) of matching numerical aperture to that of the spectrometer. Matching the convergence angle of the PL beam to that of the focusing optic inside the monochromator ensures that the whole surface area of the internal optics of the spectrometer is utilised, without being overfilled. Inside the spectrometer, the PL beam is collimated with a curved mirror (CM1) onto the reflective diffraction grating (G) that splits the beam into its spectral components. The light is then re-focused onto a detector with another curved mirror (CM2) resulting in different wavelengths being spatially separated at the detection plane. To perform a steady-state, spectral PL measurement, an image sensor is used at the detector plane, where different

wavelengths of light are focused at different pixel positions of the sensor.

Alternatively, a motorised flip mirror (FM) can be used to re-direct the light through a slit (to select a single wavelength from a spectrally-separated beam) onto a single-photon avalanche detector (SPAD). This technique, known as time-correlated single-photon counting (TCSPC) relies on a pulsed laser excitation and an attenuation of the photoluminescence beam to the point where there is only a small chance (5%) of detection of a single photon per pulse of excitation. The time between the excitation and detection of the single photon is measured and a histogram of photon arrival times can be plotted to visualise the decay of emission intensity at the chosen wavelength.

In the study described in Chapter 6, various spectroscopic systems were used to measure the PL spectra and time-resolved PL. Liquid nitrogen-cooled silicon CCD was used as an image detector to record visible range spectra of steady-state PL shown in Figures 6.2 (Symphony, HORIBA with TRIAX 190 monochromator) and 6.3 (Symphony II, HORIBA with iHR320 monochromator). The infrared (IR) part of the spectrum was recorded using an InGaAs detector (Symphony II, HORIBA with iHR320 monochromator). A spectral correction of the image was performed (for data in Figure 6.2 only) to account for the varying response of the image sensor to different wavelengths of light. For this purpose, a tungsten calibration lamp of a known spectrum was placed at the sample position and its spectrum was recorded as a reference used to calculate the correction function. To gather the data shown in Figure 6.2, the samples were excited in a vacuum, using an ultrafast Ti:Sapphire laser (Mai Tai, Spectra-Physics with 80 fs pulse width, 80 MHz repetition rate, frequency doubled to 400 nm) for the visible part of the spectrum. For the IR region of the spectrum, the samples were excited in a vacuum by a 405 nm diode laser with the repetition rate set to 80 MHz (LDH, PicoQuant). Figure 6.3 shows the PL spectra measured in air with excitation at 470 nm (continuous wave LDH diode laser from PicoQuant). For time-resolved measurements shown in Figures 6.4 and 6.5,

the Ti:Sapphire laser mentioned above was used to excite the samples placed in a vacuum with a fluence of 40 nJ/cm^2 at 400 nm wavelength. TRIAX 190 monochromator was used to direct the photoluminescence of chosen wavelength (530 nm for bandgap emission, 900 nm for IR emission and 410 nm for instrument response function measurement) onto the SPAD detector (PDM, Micro Photon Devices).

3.3 Charge-Carrier Dynamics

Following the absorption of an above-bandgap-energy photon by a semiconductor, a free charge-carrier pair is created. In this thesis, the dynamic processes occurring directly after that photoexcitation are studied in metal-halide perovskites to uncover the influence of the electric and chemical doping on the optoelectronic performance of these materials.

Figure 3.4 demonstrates the behaviour of free electrons excited with a pulse of narrowband laser light (process 1). Initially, a non-thermal population of electrons is created in the conduction band with a narrow spread of energies, matching that of the excitation pulse. Through the very fast electron-electron scattering process, lasting only tens of femtoseconds, the electron gas thermalises to form a Fermi-Dirac distribution with a temperature higher than the lattice temperature (process 2a) [121]. Next, a cooling process occurs (2b), during which the temperature of the electron gas equalises with the temperature of the lattice. This cooling process is usually mediated via the emission of longitudinal-optical (LO) phonons by the hot electrons, which decreases the electrons' kinetic energy [93]. The optical phonons subsequently decay into acoustic phonons, transferring the energy to the lattice [95]. Such a cooling process can last between hundreds of femtoseconds up to nanoseconds if the phonon-mediated processes are slowed down (eg. when the population of hot carriers is so large that the emitted LO phonons become re-absorbed, re-heating up the electron gas - this is named hot phonon bottleneck effect) [11, 93]. Additionally, as discovered in Chapter 5, hot carriers

can also lose their energy via hot-carrier–cold-carrier scattering if an already cold, large population of carriers is present in the material [83]. In this case, the energy of the hot carriers is transferred to a much larger pool of cold carriers, causing an insignificant rise in overall charge-carrier gas temperature.

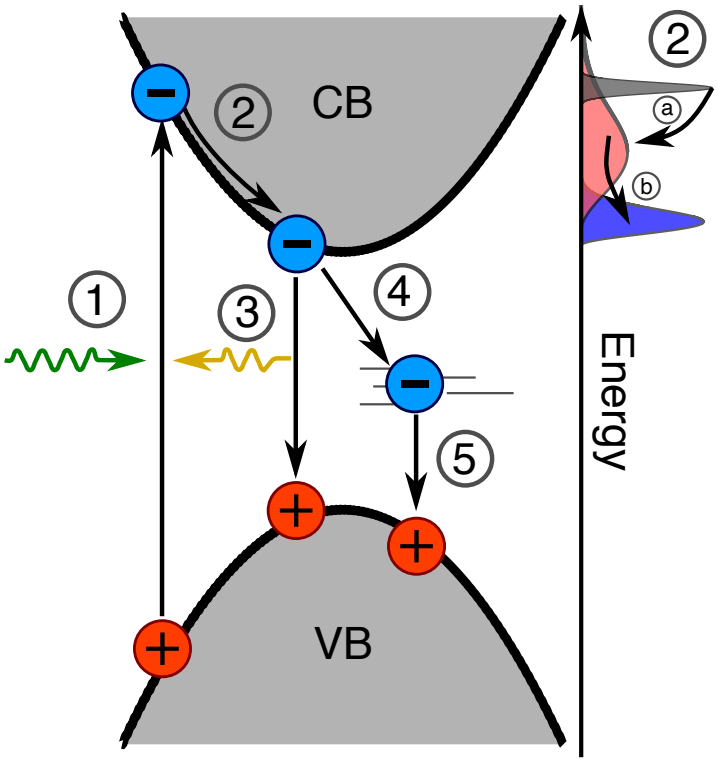


Figure 3.4: Diagram of charge-carrier dynamics after photoexcitation (1). The vertical and horizontal axes represent energy and momentum, respectively. Charge-carrier relaxation (2) is differentiated into thermalisation (a) and cooling (b). Radiative recombination (bimolecular) (3) and trap-assisted (monomolecular) recombination (4-5) of electrons and holes are shown and monomolecular recombination is composed of trapping (4) and trapped-carrier recombination (5).

Once the free carrier population cools down to the bottom of the conduction band, in order to minimise their energy, charge carriers undergo various recombination processes [122]. An optical transition, shown as process 3 in Figure 3.4 leads to radiative (bimolecular) recombination in direct-bandgap semiconductors (such as metal-halide perovskites), emitting a photon in the process [123]. Alternatively, trap-assisted recombination can occur, during which a charge carrier is captured by a defect with a mid-gap energy state (process 4) to later recombine with a hole (process 5). Although trap-assisted

(monomolecular) recombination is usually considered to be a non-radiative process [80, 87], Chapter 6 reveals that sometimes a radiative transition can exist between the trap state and the valence band, which leads to the emission of sub-bandgap photoluminescence, like that shown in Figure 6.2. Finally, higher-order (multi-body) processes can lead to charge-carrier recombination, through for example Auger effect. Such non-radiative recombination of a free electron with a free hole can occur when a direct optical transition is not allowed due to an offset in the momentum space. However, a presence of a third carrier, which absorbs the excess momentum released in the transition, is required for this transition to occur, which reduces the probability of this recombination pathway in direct-bandgap semiconductors [122].

The rates of recombination processes in a semiconductor will determine its performance in various optoelectronic devices [80]. A slow charge-carrier cooling process enables more efficient above-bandgap charge-carrier extraction in hot-carrier solar cells, a high rate of bimolecular recombination is desirable in light-emitting diode applications, and slow trap-mediated recombination and large photon recycling (re-absorption of a photon emitted during radiative recombination) make the material highly suitable for an active layer in efficient photovoltaic devices. It is therefore important to understand fully the relaxation and recombination pathways of photoexcited charge carriers in novel semiconducting materials, in order to identify the promising candidates for future technologies.

A charge-carrier population decay model encompassing radiative and trap-mediated recombination is presented in Chapter 6. The model is successfully used to explain the dynamic behaviour of photoluminescence and conductivity induced after pulsed laser excitation. Chapter 5, on the other hand, introduces a novel experimental technique, able to measure the charge-carrier cooling dynamics on a sub-picosecond timescale, and describes the effect of electrical doping on the ultrafast charge-carrier relaxation processes.

3.4 Terahertz Spectroscopy

Dynamic electronic processes in semiconductors can be studied with a variety of time-resolved techniques. However, measuring the transient conductivity of a photoexcited semiconductor is particularly important for assessing the suitability of the material for photovoltaic applications. To achieve high power conversion efficiency (PCE), photoexcited charge carriers need to maintain relatively high mobility long enough to reach the transport layers, undergo extraction, and generate electricity flow [124].

The mobility and lifetime of free carriers can be probed with terahertz (THz) radiation, a non-contact method of measuring the conductivity of a thin film by transmitting short (picosecond-duration), single-cycle pulses of THz light through the sample [49]. The method of extracting the conductivity of thin films from THz transmission function is discussed in detail in the next chapter, in which the technique most applicable to doped semiconductors is identified. Briefly, the expression used throughout this thesis to calculate the photoinduced change of conductivity ($\Delta\tilde{\sigma}$) from the strength of the transmitted THz radiation ($T_{\text{pump-off/on}}$) can be shown to be of the form

$$\Delta\tilde{\sigma} = \left[\tilde{\sigma}_{\text{dark}} + \frac{\epsilon_0 c(n_1 + n_3)}{L}\right] \frac{T_{\text{pump-off}} - T_{\text{pump-on}}}{T_{\text{pump-on}}}\,, \tag{3.6}$$

where $\tilde{\sigma}_{\text{dark}}$ is the complex conductivity of the material in the dark (no photoexcitation), $n_1 = 1$ and $n_3 = 2.1$ are the refractive indices of vacuum and quartz substrate, respectively [125], and L is the thickness of the thin film (400 nm for films investigated in Chapter 5, 500 nm in Chapter 6). An approximation related to negligible dark conductivity $\tilde{\sigma}_{\text{dark}} = 0$ was made for films investigated in Chapter 6 and for films with suppressed doping studied in Chapter 5. Furthermore, the charge-carrier sum mobility of the free charge carriers μ can be determined assuming Drude-type conductivity [49], for which

$$\Delta\tilde{\sigma} = \mu n e\,, \tag{3.7}$$

where e is the electron charge and n is the charge-carrier population density, which could be estimated just after the excitation by knowing the fluence of the photoexcitation pulse (the energy of the pulse divided by the excitation spot area) and the absorption measurement data (absorbed fraction of the incident photons is equal to $1 - T(\lambda) - R(\lambda)$ at the wavelength λ of the excitation beam, as defined by Equations 3.2 and 3.1).

By measuring the THz transmission function through a thin film of a semiconductor, and tracking its evolution after photoexcitation, terahertz spectroscopy allows for detailed investigation of the charge transport properties in a semiconductor, essential for the assessment of its optoelectronic performance. This section focuses on describing the experimental methods used in this thesis to generate and detect THz pulses, and the ways various ultrafast laser pulses are timed with respect to each other, and their wavelength and intensity controlled in the discussed spectroscopic techniques. The next chapter further investigates how the material properties can be calculated from data gathered in the measurements described below, focusing on doped semiconducting thin films.

3.4.1 Time-Domain Spectroscopy

The most basic terahertz spectroscopy technique is the THz time-domain spectroscopy (THz TDS). This method allows measuring the IR response (including among others free carrier conductivity and lattice dielectric response) of a thin film sample on a transparent substrate in the dark, i.e. without initial photoexcitation. Such measurement enables estimating the doping level in the material (see Figure 5.1 in Chapter 5) and detecting phonon modes in the crystal (Figure B.6 in Appendix B) [49].

A detailed diagram of the experimental setup used to acquire conductivity data presented in Chapters 4,5 and 6 is shown in Figure 3.5. A Ti:Sapphire amplified laser system composed of the oscillator (Maitai, Spectra-Physics) and regenerative amplifier

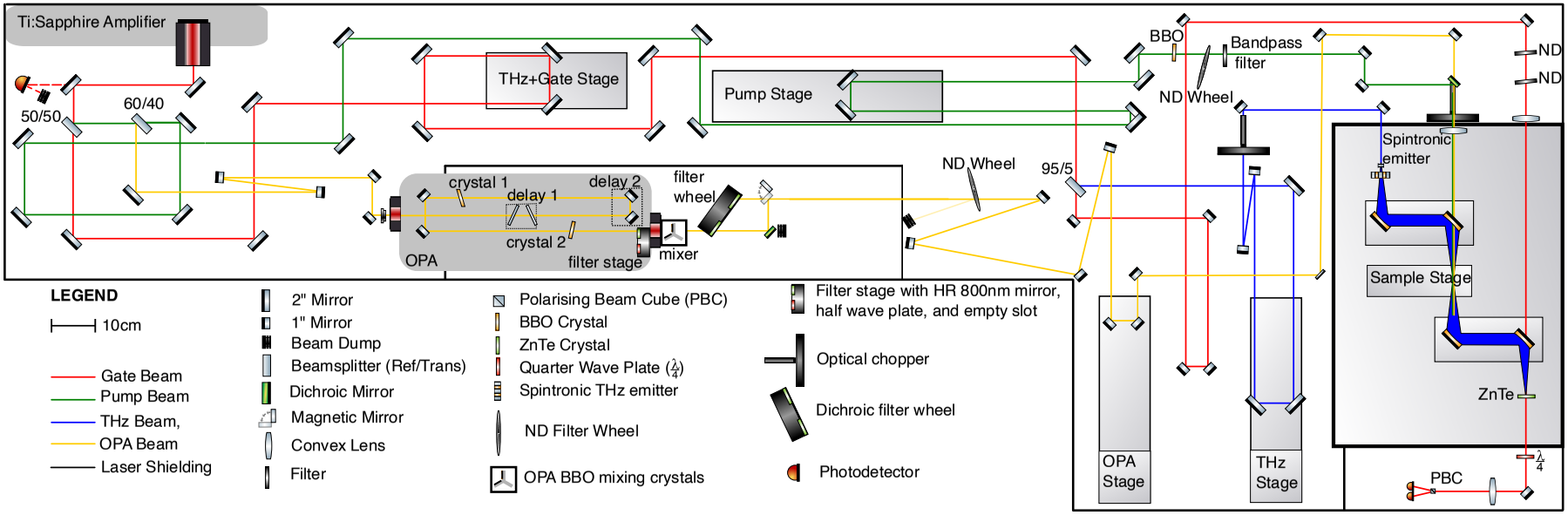


Figure 3.5: Terahertz spectroscopy setup including Ti:Sapphire amplified laser system and optical parametric amplifier used to generate 35 fs laser pulses used in the discussed spectroscopic techniques. Optical delay stages are used to control the relative arrival time of the pulses at the sample position and at the THz detection plane. Optical choppers are used to block relevant laser pulses (as discussed in this section) to enable background subtraction. Photoexcitation and measurement of the conductivity of the samples, as well as THz generation and detection, occurs in a vacuum chamber evacuated to $\sim 10^{-1}$ mbar.

(Spitfire, Spectra-Physics), pumped by a Nd:YAG Q-switched laser (Ascend, Spectra-Physics), was used to generate ultrafast light pulses (35 fs duration) with a central wavelength of 800 nm, at 5 kHz repetition rate. These pulses are split into multiple beam lines, of which THz generation beam (blue line in Figure 3.5) and gate beam (red) are relevant to THz TDS experiments. THz generation beam is delayed with respect to the gate using an optical delay stage. This mechanical stage allows for very precise control over the relative arrival time of the two pulses at the detection point by extending or contracting the optical path length of one of the laser beams. THz generation beam is also passed through an optical chopper running at 2.5 kHz rate (half of the repetition rate of the laser), allowing only every second pulse to pass through to enable background measurement.

Terahertz Generation

Terahertz radiation is generated using a spintronic emitter [126], a tri-layer device composed of 2 nm tungsten, 1.8 nm $Co_{40}Fe_{40}B_{20}$, and 2 nm platinum deposited on a quartz substrate, magnetically biased between two permanent magnets. When an ultrafast laser pulse with sufficient energy is incident onto a such structure, a transient current of electrons is launched in all directions in the $Co_{40}Fe_{40}B_{20}$ alloy. Due to the ferromagnetic nature of the material and external magnetic bias, the current is strongly spin-polarised. Upon entering the non-magnetic material (Pt or W), the electrons are deflected from the direction of propagation through the inverse spin Hall effect (originating from spin-orbit interactions). Since electrons with opposite spins are deflected in opposite directions and the current is strongly spin-polarised, a net transient current will flow perpendicularly to the laser beam propagation direction. If the current is sufficiently short-lived and strong, its rise and decay will radiate a single cycle of radiation in the THz frequency range. Platinum and tungsten are used on either side of the $Co_{40}Fe_{40}B_{20}$ alloy in such spintronic devices because they both exhibit strong inverse spin Hall effects but act in opposite

directions. Therefore, sandwiching the ferromagnetic material between them enhances the terahertz radiation emission as the electrons launched in the opposite directions in the stack will be deflected in the same direction in the two metals, producing in-phase radiation.

Terahertz Detection

After generation, the THz pulse is collimated and then focused onto the sample with gold-coated, off-axis parabolic (OAP) mirrors. Due to the long wavelength of THz radiation (∼0.3 mm) and therefore the long Rayleigh length of the focused beam, the THz beam at the sample position can be considered to be a plane wave, which is a necessary assumption for derivations of data analysis methods discussed in the next chapter. After passing through the thin-film sample on a transparent (in the THz frequency range) substrate, the transmitted radiation is collected and refocused onto a detection crystal with another pair of off-axis parabolic mirrors. ZnTe crystal, cleaved along the (110) crystal plane, is used to detect the radiation through electro-optic sampling [127] (in the study presented in Chapter 5, 1 mm-thick crystal was used and in Chapter 6, 0.2 mm). To detect the electric field strength of the THz radiation, the beam is overlapped with the gate beam spatially and temporally at the detection crystal, by ensuring the spatial overlap of the gate beam and THz generation beam without the spintronic emitter placed in its path, and by setting the optical path lengths of the THz generation beam and the gate beam to be the same. Due to the Pockels effect in ZnTe, the THz radiation's electric field modulates the crystal's birefringence, causing a change in the polarisation of the gate beam. This change can be measured using a quarter-wave plate (marked as $\frac{\lambda}{4}$ in Figure 3.5), Wollaston prism (marked as PBC) and a balanced-photodiode detector. The quarter-wave plate is rotated such that in the absence of THz radiation it converts the elliptically polarised output from the ZnTe crystal to a circularly polarised beam (the amount and angle of ellipticity will depend on the thickness of the crystal and its rotation angle with respect to the

input polarisation of the gate beam). The vertically (s) and horizontally (p) polarised components of the gate beam are split by the polarising Wollaston prism and their relative intensity is measured by balanced photodiodes (two biased photodiodes connected in series, where the differential photoinduced current is measured). In the absence of THz radiation, the circularly polarised output from the waveplate is split evenly and no signal is detected. However, when the electric field of the radiation is present in the ZnTe, the gate beam will no longer be perfectly circularly polarised, causing a differential current flow in balanced photodiodes proportional to the electric field strength.

Signal Processing

The gate pulse is incident at the balanced photodiodes at 5 kHz repetition rate of the laser. Since THz beam goes through an optical chopper, the radiation is only present every second gate pulse, producing alternating "THz-off" - "THz-on" signals in the balanced photodiode detector. This output is most often amplified using a lock-in amplifier, locked to the frequency of the optical chopper, which amplifies the difference between the two signals. However, in the experiments presented in the following chapters, a custom-made FPGA-based data acquisition board was used to acquire the data for both channels ("THz-off" and "THz-on") subtracting and amplifying the signal after acquisition.

Time-Domain Measurement

The temporal overlap of the gate beam and the THz beam on the ZnTe crystal is varied with the optical delay stage. This allows for the electric field strength (rather than just the intensity) to be mapped with resolution only limited by the duration of the gate pulse (35 fs) and the resolution of the optical stage (around 1 μm, corresponding to $\sim$6 fs delay). The result of such measurement is presented in Figure 4.6 in Chapter 4. The phase information of the THz radiation is conserved, enabling direct measurement of the complex refractive index of the sample, as described in the next chapter.

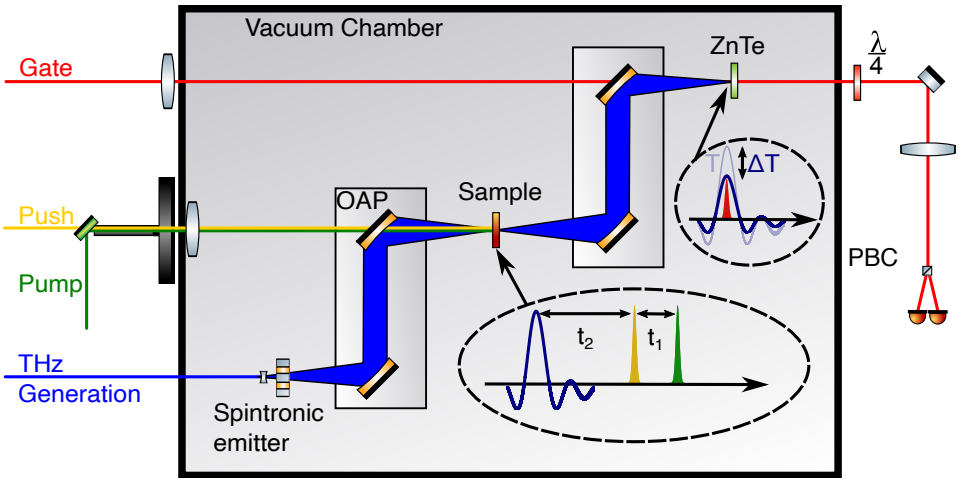


Figure 3.6: A diagram of the vacuum chamber used in THz spectroscopy measurements. The off-axis parabolic mirrors (OAP) are used to focus the generated THz probe onto the thin film sample and subsequently onto the ZnTe detection crystal. Lenses are used to focus the pump (green line) and push (yellow line) beams through a hole in the OAP. The relative delays between the pulses (t_1 between pump and push which is kept constant and t_2 between push and probe which is varied) are shown schematically at the sample position and at the detection plane. The pump-on and pump-off channels of detection (discussed in the main text) are shown as a reduced intensity of the transmitted THz pulse, T without photoexcitation and $T - \Delta T$ with photoexcitation present.

3.4.2 Optical-Pump–THz-Probe

To study the dynamics of free charge carriers in semiconductors, the conductivity of the material (and hence the THz transmission) has to be known at different time delays after photoexcitation. For this reason, an additional laser beamline is added to the THz-TDS experiment to promote electrons to the conduction band. This beam is shown in the green line (pump beam) in Figure 3.5. The pump pulse is delayed with respect to the THz probe using an optical delay stage (pump stage) and passes through an optical chopper running at 1.25 kHz frequency. The 50% duty cycle of the chopper lets through two laser pulses and blocks the subsequent two, resulting in 4 detection channels: THz-off–Pump-on, THz-on–Pump-on, THz-off–Pump-off, THz-on–Pump-off. The pump beam delay is adjusted so that the excitation pulse arrives at the semiconductor at various times before the THz probe pulse- this enables mapping of the conductivity decay trace of the sample. At each delay point, it is possible to perform a full THz-TDS measurement to obtain

the spectral photoinduced conductivity response of the material. However, most often only the spectral average of the real part of the conductivity is measured, by adjusting the THz beam-gate beam so that transmitted THz radiation is measured at the peak of the electric field profile. This method of average conductivity measurement is discussed in Chapter 4. The resultant decay traces of the transient photoinduced conductivity are shown in Figure 6.6 in Chapter 6 for $MAPbBr_3$ perovskite semiconducting films. These films were photoexcited with the pump beam that was frequency doubled in a BBO crystal to produce light pulses with 400 nm central wavelength, using fluences indicated in the legend of the figure, adjusted with a neutral-density (ND) filter wheel. It is important to note that the film has to be excited evenly across the area probed by the THz radiation, i.e. the beam spot size of the pump beam has to be larger than that of the THz beam. This is ensured by focusing the pump beam through a hole drilled in the off-axis parabola focusing THz radiation onto the sample and then allowing the pump to diverge onto the investigated thin film.

3.4.3 Pump-Push-Probe Spectroscopy

As a part of the DPhil work presented in this thesis, a novel extension of the optical-pump–THz-probe (OPTP) spectroscopy was built, expanding the capabilities of the system described above. This Optical-pump–IR-push–THz-probe technique (or simply pump-push-probe, PPP), pioneered in the study presented in Chapter 5, allows for investigating sub-bandgap transitions by illuminating the already-photoexcited semiconductor with an IR laser pulse with below-bandgap photon energy. Using this technique, intraband, intersubband and de-trapping transitions can be observed and their effects on the material's conductivity measured.

In the setup shown in Figure 3.5 and used in measurements summarised in Chapter 5, this technique was implemented by introducing the fourth beamline split-off from the

main Ti:Sapphire output beam (OPA beam, marked by the yellow line) and using an optical parametric amplifier (OPA- TOPAS-C, Light Conversion) to convert the 800 nm wavelength beam to an IR beam of adjustable wavelength. After the generation of white light in a sapphire plate and two stages of parametric amplification, the OPA outputs a beam composed of the signal light (SIG) and the idler light (IDL). The photon energies of the two beams must sum up to the photon energy of 800 nm pump, therefore the SIG light will always have a central wavelength <1600 nm and IDL beam >1600nm. The output of the OPA is passed through a spectral filter (dichroic filter wheel in Figure 3.5) to separate the two beams and remove the remaining white light and 800 nm pump light.

The infrared push beam path length is adjusted with an optical delay stage (OPA stage). In order to ensure the IR pulse arrives at a constant time delay after the initial, visible photoexcitation, the OPA stage has to move synchronously with the pump stage such that their relative path length difference remains constant as the conductivity at various time delays after photoexcitation is probed by the THz pulse. The push pulse (yellow line) is recombined spatially with the visible pump (green line) using a dichroic mirror, which reflects light with a wavelength <950 nm and transmits IR light. The propagation of the recombined beams is shown in Figure 3.6. After recombining, the two beams go through an optical chopper (there is no separate chopper for the push beam), and a lens, which focuses them through a hole in the OAP and diverges them onto the sample. The fluence of the push beam is adjusted with a variable ND filter wheel and its wavelength is controlled in the OPA's software.

Once the semiconducting film is photoexcited with the pump pulse, a population of free carriers is created, enabling further excitation to higher energy states with the IR pulse, which on its own is not able to promote the electrons across the band gap. In the absence of radiative trapping (defect states that capture the electrons radiatively would also allow for the inverse process of de-trapping with an optical IR pulse), the carriers

can only be excited through intraband transitions deeper into their respective bands or through intersubband transitions to higher-lying sub bands. Chapter 5 uncovers that in $FA_{0.83}Cs_{0.17}SnI_3$ perovskites, the former effect is present and that such pump-push-probe technique allows investigating the relaxation dynamics of free carriers promoted to energy states high in the bands (charge-carrier thermalisation and cooling). The THz radiation is found to be able to probe the hot carrier population due to reduced conductivity of the material upon IR push pulse heating, therefore providing an excellent scheme for measuring the cooling decay times in high charge-carrier mobility semiconductors.

Since tin-iodide perovskites studied in Chapter 5 are generally electrically doped due to spontaneous tin vacancy formation, the presence of the free carriers in un-excited samples allows for probing the charge-carrier cooling dynamics without the initial photoexcitation. In this kind of experiment, resulting in data shown in Figures 5.3, 5.4, 5.5, 5.6 and 5.7A, the pump beam is blocked and only the push beam is allowed to excite the sample. This scheme is referred to as "push-probe" in Chapter 5. In tin-iodide perovskites with tin-fluoride added during deposition, the un-excited sample shows much lower doping levels due to suppressed tin vacancy formation. Therefore, a photoexcitation has to be used prior to the infrared push illumination to observe hot-carrier dynamics. The photoexcitation wavelength of the pump beam of 800 nm was used (direct output of the Ti:Sapphire laser without frequency doubling) with the wavelength of the push pulse set to 1450 nm in the pump-push-probe measurement presented in Figure 5.2B and to 1430 nm during the spectral measurement presented in Figure 5.7B. Figures 5.5 and 5.7A show push-induced conductivity obtained with IR push pulse of 1390 nm wavelength at the estimated fluence of 142 $\mu J/cm^2$ in the spectral measurements. The push-fluence of 254 $\mu J/cm^2$ was used in measurement shown in Figure 5.2B and 46 $\mu J/cm^2$ in the spectral measurement shown in Figure 5.7B.

4

Terahertz Conductivity Analysis in Doped Semiconductors

Contents

4.1 Introduction 59
4.2 Methodology 60
4.2.1 Transmission Function 60
4.2.2 Material Properties 62
4.2.2.1 Calculations 64
4.3 Results 66
4.3.1 Dark Conductivity Calculations 66
4.3.2 Photoconductivity - Common Approach 68
4.3.3 Photoconductivity of Conductive Films 71
4.4 Experimental Implementation 74
4.5 Effects of Charge-Carrier Scattering Time 79
4.5.1 Assessment of Photoconductivity Estimates 79
4.5.2 Simulated Transmission Functions 80
4.6 Conclusions 82

The work presented in this chapter has been published in: A. M. Ulatowski, L. M. Herz, M. B. Johnston. 'Terahertz Conductivity Analysis for Highly Doped Thin-Film Semiconductors', *J Infrared Milli Terahz Waves*, **41**, *1431-1449* (2020) (Ref. [128]).

4.1 Introduction

In this chapter of the thesis, approximations commonly made in data analysis of THz transmission through thin films are challenged and investigated in detail. Mathematical derivations are used together with computational simulations to find the most accurate expression for photoinduced conductivity from the transmitted THz radiation for electrically doped thin film semiconductors.

The progress of thin-film technology in photovoltaic (PV) applications has led to highly efficient solar cells employing a variety of semiconductors being developed in recent years [7]. The benefits of devices based on thin-films include their ease of fabrication, wide choice of substrate materials and low cost of production [129]. One of the promising groups of materials used as sub-micron thin-films are hybrid metal-halide perovskites, which exhibit excellent optoelectronic properties and are relatively easy to fabricate through solution processing using widely available precursors [18, 40, 130].

Terahertz time-domain spectroscopy (THz-TDS) and optical-pump–THz-probe (OPTP) experiments (described in Chapter 3) have been successfully used to investigate properties of thin films used in PV applications, by measuring the charge-carrier mobilities and the recombination dynamics of photoexcited carriers. These measurements allow one to estimate the diffusion length of electrons and holes, which directly affects the performance of semiconductor devices [30, 31, 131–134]. By investigating THz field transmission through photoexcited thin films, the type of photoconductivity can be established by comparing different conductivity models (including Drude conductivity, hopping transport, plasmon models etc. [49]) against the THz transmission data. Such analysis provides valuable information about the charge transport properties in novel materials, which is essential for an improvement of their optoelectronic properties. Finally, THz-TDS on thin films in the dark (without photoexcitation) can be used as a non-contact probe

of conductivity arising from doping in the semiconductors, thereby revealing directly the resistivity of the material without the need for metal contacts. The resistivity obtained in this way can be used to estimate the background dopant density when paired with charge-carrier mobility measurements.

With the fast progress of thin-film technology in photovoltaics and a rise in popularity of THz spectroscopy to investigate the properties of semiconducting materials, it is important to pay close attention to data analysis, in order to avoid misinterpretation of results due to artefacts [135, 136]. In this chapter, the assumptions commonly made when calculating the properties of thin films from THz-TDS data are investigated, showing the limitations of the approximated expressions. In highly doped thin films, with dark conductivity comparable to $10^2\,\Omega^{-1}\mathrm{cm}^{-1}$, some of these approximations result in a significant underestimate of the photoconductivity, and therefore charge-carrier mobility in the semiconductor. Tin-iodide perovskite thin films were used as an example system, for which the assumption of negligible dark conductivity can no longer be used as it leads to significantly underestimated values of charge-carrier mobility. A more precise analytical formula should be used for photoconductivity calculations in doped semiconductors, which greatly improves the accuracy of the calculated photoconductivity values, while not requiring numerical data fitting or other involved data analysis techniques, to obtain material properties from THz field transmission measurements.

4.2 Methodology

4.2.1 Transmission Function

The chapter begins by considering a common experimental method used to obtain the conductivity of a material with terahertz radiation. Details of the experimental procedures for generating and measuring the THz pulse are described in Chapter 3. Figure 4.1 shows a typical geometry used for THz-TDS measurements, in which the thin film sample with

complex refractive index $\tilde{n}_2 = \tilde{n}$ and thickness L is deposited on a thick, transparent substrate ($\tilde{n}_3 = n_3$) and placed in vacuum ($\tilde{n}_1 = n_1 = 1$) in the focal spot of the THz beam. A condition that is often met, and simplifies calculations is that the thickness of the substrate D is large enough to allow internal reflections of the THz probe (of duration t_{THz}) to be removed by windowing the TDS data (i.e. $D > t_{\mathrm{THz}}c/2n_3$) [49]. The transmitted amplitude of the THz electric field at normal incidence through such

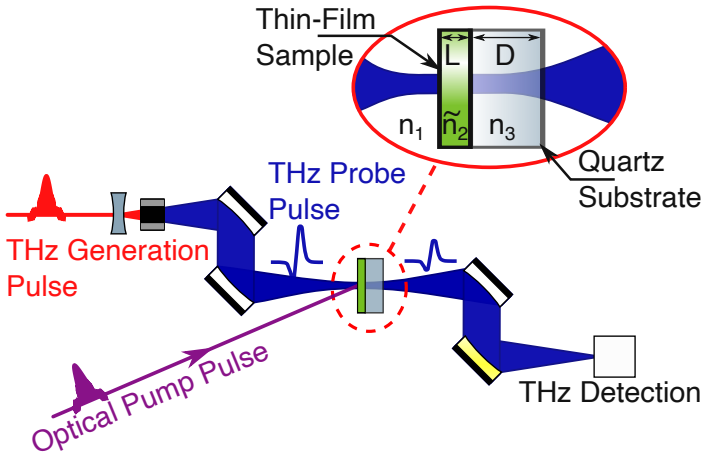


Figure 4.1: Typical geometry of THz-TDS experiment, featuring terahertz pulse generation using ultrafast laser beam and a spintronic THz emitter, gold-coated off-axis parabolic mirrors used to focus the radiation onto the thin film and subsequently onto THz detector, and time-domain field detection (realised by electro-optic sampling in (110)-ZnTe crystal in the setup used in this Thesis and described in Chapter 3).

a geometry (T_{sample}) depends on the properties of the sample, and can be calculated explicitly by considering amplitude reflection and transmission on the boundaries between media, as well as the propagation of the plane wave through the materials [49, 137, 138],

$$T_{\mathrm{sample}} = t_{12}t_{23}\exp(i\tilde{n}L\omega/c) \times \mathrm{FP} \times \psi\,, \tag{4.1}$$

where ψ describes the propagation of the field through the substrate. The Fabry-Perot term FP due to multiple internal reflections inside the thin film is given by

$$\mathrm{FP} = \sum_{p=0}^{\infty}\left(r_{21}r_{23}\exp(2i\tilde{n}L\omega/c)\right)^p = \frac{1}{1 - r_{21}r_{23}\exp(2i\tilde{n}L\omega/c)}\,, \tag{4.2}$$

where r_{ij} and t_{ij} are the Fresnel reflection and transmission coefficients at normal incidence:

$$t_{ij} = \frac{2\tilde{n}_i}{\tilde{n}_i + \tilde{n}_j}, r_{ij} = \frac{\tilde{n}_i - \tilde{n}_j}{\tilde{n}_i + \tilde{n}_j}. \tag{4.3}$$

The plane-wave approximation can be satisfied by placing the film in the focal spot of the terahertz radiation and ensuring that the sample is much thinner than the Rayleigh range of the THz beam [138] (usually in few-mm range). The reference transmission through the bare substrate is then given by

$$T_{\text{substrate}} = t_{13} \exp(iLn_1\omega/c) \times \psi. \tag{4.4}$$

Finally, using Equations 4.1 and 4.4, the relative transmission of the THz electric field through the sample can be expressed as

$$\frac{T_{\text{sample}}}{T_{\text{substrate}}} = \frac{t_{12}t_{23}}{t_{13}} \frac{\exp(i(\tilde{n} - n_1)L\omega/c)}{1 - r_{21}r_{23}\exp(2i\tilde{n}L\omega/c)}. \tag{4.5}$$

It is worth noting that the Fabry-Perot term originating from internal reflections inside the substrate was neglected in Equations 4.1 and 4.4, as for thick substrates the multiple internal reflections can be windowed-out in time-domain measurement of the transmitted electric field [49].

4.2.2 Material Properties

The complex refractive index of a material $\tilde{n}$ depends on its polarisability, which can be described by the complex dielectric function $\tilde{\epsilon}_r = \epsilon_1 + i\epsilon_2$. The relation between the refractive index and the dielectric function is given by

$$\tilde{n}^2 = \tilde{\epsilon}_r = \epsilon_1 + i\epsilon_2. \tag{4.6}$$

For conductive samples, one can further distinguish the individual contributions to the dielectric function from the crystal structure (through phonon modes, lattice polarisation), $\tilde{\epsilon}_L$, as well as the charge carriers (movement of free charge carriers, polarisation of excitons),

$i\tilde{\sigma}_{\mathrm{cc}}/\omega\epsilon_0$. Here, $\tilde{\sigma}_{\mathrm{cc}}$ is the complex conductivity of the charge carriers, which could be present in the semiconducor as a result of either photoexcitation or doping.

An apparent conductivity, $\tilde{\sigma} = \sigma_1 + i\sigma_2$, can be then defined, which encompasses both these contributions to the overall dielectric response of the material,

$$\tilde{\epsilon}_r = \tilde{\epsilon}_L + \frac{i\tilde{\sigma}_{\mathrm{cc}}}{\omega\epsilon_0} \equiv 1 + \frac{i\tilde{\sigma}}{\omega\epsilon_0}\,. \tag{4.7}$$

The relation between these quantities is illustrated in Figure 4.2, which shows how the charge-carrier conductivity (panel A) and the dielectric function of the crystal (panel B) contribute to the overall polarisability of the sample (panel C), here presented as the apparent complex conductivity $\tilde{\sigma}$. The conductivity of charge carriers $\tilde{\sigma}_{\mathrm{cc}}$ with number density n, mobility μ and charge q was assumed to be Drude-like,

$$\tilde{\sigma}_{\mathrm{cc}} = \sigma_{\mathrm{DC}}/(1 - i\omega\tau) = n\mu q/(1 - i\omega\tau)\,, \tag{4.8}$$

where σ_{DC} is the DC conductivity of the charge carriers (the conductivity in the limit of frequency of the THz probe tending to 0), and τ is the scattering time of charge carriers, with the scattering rate $1/\tau$ comparable to THz frequencies. The dielectric response of the crystal is modelled by including one optical phonon mode in the presented spectral region at $\omega = \omega_p$, resulting in the overall dielectric function being described by

$$\tilde{\epsilon}_L = \epsilon_\infty - (\epsilon_{\mathrm{s}} - \epsilon_\infty)\frac{\omega_p^2}{\omega^2 - \omega_p^2 + i\omega\gamma}\,, \tag{4.9}$$

where ϵ_∞ is the high frequency dielectric constant of the material and ϵ_{s} is the static dielectric constant.

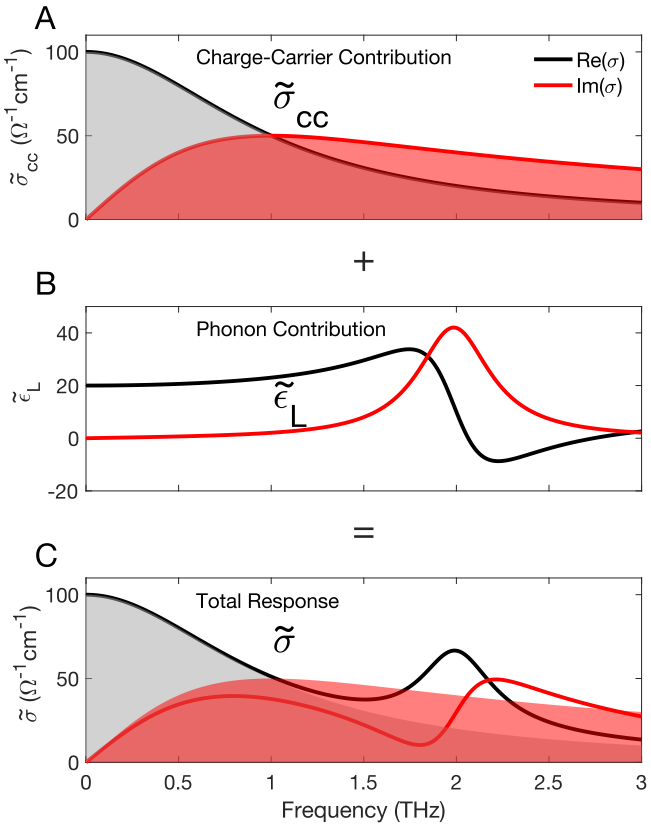


Figure 4.2: (A) The complex conductivity of the free charge carriers was assumed to be Drude-like (Equation 4.8) with the DC conductivity of $\sigma_{\mathrm{DC}} = 100\,\Omega^{-1}\mathrm{cm}^{-1}$, and the average charge-carrier scattering rate $\frac{1}{\tau} = 2\pi \times 10^{-12}\,\mathrm{s}^{-1}$. (B) The dielectric contribution of the crystal is affected by the presence of an optical phonon mode at $\omega_p = 4\pi\,\mathrm{THz}$, and can be described by Equation 4.9. Here, the background optical dielectric constant was set to $\epsilon_\infty = 10$, and the static dielectric constant was chosen to be $\epsilon_{\mathrm{s}} = 20$. (C) The overall dielectric response was calculated from Equation 4.7 and is shown as the apparent complex conductivity, with the shaded areas indicating the conductivity of the charge carriers only, for comparison.

4.2.2.1 Calculations

In this chapter, Equation 4.5 is used to calculate numerically the complex transmission function of the THz electric field through a thin film with chosen dielectric function, $\tilde{\epsilon}_r$. Subsequently, the calculated transmitted field is substituted into commonly used approximated analytical formulas (Equations 4.10, 4.11 and 4.12), to obtain the apparent complex conductivity of the sample. Then, a comparison of the estimated conductivity to its exact, initially chosen value is made, in order to evaluate the limits of these

approximations. A derivation of the expression shown in Equation 4.17 is presented and the derived formula is tested in the same way, showing much higher accuracy of the calculated photoconductivity over a large range of photo- and dark conductivity values than the commonly used approximations.

The focus of this chapter is the effect of background doping, which induces significant dark conductivity in samples. This is modelled as Drude-type conductivity throughout the chapter since this kind of conductivity is most relevant for bulk, 3D semiconductors. As the effect of the phonon modes on photoconductivity calculations in the THz regime was previously discussed by La et al. [136], an assumption was made (for simplicity) that the crystal contribution to the dielectric response can be described by an optical (high-frequency) dielectric constant. This dielectric constant is set to $\tilde{\epsilon}_L = \epsilon_\infty = 10$, it is frequency-independent, and any phonon contribution to the conductivity spectrum in the calculations is neglected.

In common with the approach of La et al., the limits of the discussed approximations are assessed by comparing only the real part of the calculated conductivity to its exact values, as the measurements of the imaginary part are strongly affected by experimental uncertainty, originating from variations of substrate thickness between the reference and the sample [136].

Although previous research investigated the limits of thin-film approximation in the context of optical determination of conductivity [139–141], the existing studies focused on the error caused by the thickness of the sample and the frequency of the probe beam, rather than the conductivity of the film. Since the thin-film approximation can be also violated by the high refractive index of the sample [142–144], it is important to understand the effects of the complex conductivity on the validity of commonly used formulas in the regime where thin-film approximation would usually be made. This chapter, therefore, analyses the influence of complex conductivity alone on the error

caused by using the over-simplified formulas for 400 nm-thick thin films probed with THz radiation at the frequency of 1 THz.

4.3 Results

4.3.1 Dark Conductivity Calculations

First, the validity of assuming negligible optical thickness of the thin film is investigated. This assumption is commonly made in the literature in order to calculate the conductivity of a sample from its relative THz-field-amplitude transmission obtained from THz-TDS measurements [49, 135–137]. This condition can be written as $L\omega n/c \ll 1$ and $L\omega\kappa/c \ll 1$, where n and κ are the real and imaginary parts of the complex refractive index $\tilde{n}$, respectively. As the wavelength of the THz radiation (∼mm) is much longer than the thickness of the thin film ($< 1\,\mu$m), this approximation is generally satisfied for thin films with low refractive index. As a result, Equation 4.5 can be simplified and re-arranged to obtain the electric field transmission equivalent of Tinkham formula [145, 146], relating the complex conductivity to the relative THz field transmission through the thin film [49, 135–137],

$$\tilde{\sigma} = \frac{T_{\text{substrate}} - T_{\text{sample}}}{T_{\text{sample}}} \frac{\epsilon_0 c(n_1 + n_3)}{L}\,. \tag{4.10}$$

The validity of this approximation for dark conductivity calculations is assessed in Figure 4.3, which shows the relative error of the approximated value of the real part of the conductivity, compared with its exact values. As indicated by the green region in the figure, high accuracy of the expression is noted for low-conductivity materials. The formula is suitable to calculate the real part of the complex dark conductivity of materials up to $10^4\,\Omega^{-1}\text{cm}^{-1}$, above which the large complex refractive index invalidates the assumption of negligible optical thickness.

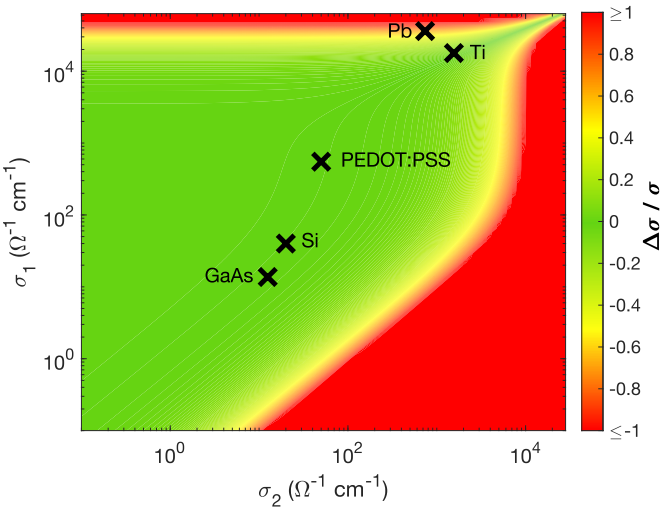


Figure 4.3: The relative error $\left(\frac{\Delta\sigma}{\sigma} = \frac{\sigma_{\text{exact}} - \sigma_{\text{calculated}}}{\sigma_{\text{exact}}}\right)$ of the real part of complex apparent conductivity σ_1, calculated using simplified analytical expression shown in Equation 4.10. The accuracy of the approximation was assessed by choosing the exact values of σ_1 and σ_2 and calculating the transmission function numerically, using Equations 4.5, 4.6 and 4.7. The calculated transmission was then used in Equation 4.10 to obtain the approximated value. The calculations were performed at $\nu = 1\,\text{THz}$ ($\omega = 2\pi\,\text{THz}$) for a 400 nm thin film deposited on a thick quartz substrate ($n_3 = 2.1$ [125]) and is shown as a function of the real and imaginary part of the apparent complex conductivity $\tilde{\sigma}$, as defined in Equation 4.7. The green regions in the plots represent values of complex conductivity, for which Equation 4.10 provides a good approximation and red regions indicate large deviation of calculated quantities from their exact values, as indicated by the colour bar. The positions marked with a cross represent the complex conductivities at 1 THz of various conductive materials, including doped semiconductors and metals: 0.038 Ωcm n-doped GaAs [147], n-type Si with phosphorus dopant density of $10^{18}\,\text{cm}^{-3}$ [148], solvent-doped PEDOT:PSS (6% DMSO) [149], titanium and lead [150].

The large range of conductivity values for which the thin-film approximation holds well spans a variety of materials including inorganic doped semiconductors [147, 148], conductive organic semiconductors [149] and even metals [150]. Equation 4.10 is therefore most suitable for calculating the dark conductivity of novel doped semiconductors, provided that sub-micron-thick thin films are used. For the characterisation of highly conductive, metallic films, thinner samples (tens of nanometers) have to be used to satisfy the assumption of negligible optical thickness [151].

Furthermore, Equation 4.10 provides a relation between the relative transmission of THz field through the sample and its total apparent conductivity, regardless of its origin.

A semiconductor thin film could exhibit apparent conductivity in THz regime due to the existence of phonon modes in the investigated spectral range as well as presence of charge carriers introduced either by electrical doping or photoexcitation. Therefore, the validity of the thin-film approximation presented in Figure 4.3 is relevant to measurements of dark charge-carrier conductivity, dielectric response of the lattice, as well as the photoconductivity of the sample excited by laser pulses with above-bandgap photon energy. As such, the limits of the validity of Tinkham formula (shown in Equation 4.10) discussed in this section are the upper bounds of validity limits of all formulas assessed in the following sections, all based on the assumption of a negligible thickness of the sample.

4.3.2 Photoconductivity - Common Approach

It is important to consider the effect of a photoexcitation on the properties of the material when studying its applicability in optoelectronic devices. In this section this is modelled as a uniform excitation of free charge carriers throughout the thickness of the thin film. Such uniform photoexcitation is achieved when the absorption depth at the wavelength of the pump beam (used to photoexcite the film, as shown in Figure 4.1) is much longer than the thickness of the sample, which can be easily realised by exciting the semiconductor with pump photon energy just above the bandgap energy or by using sufficiently thin samples. The assumption that the photoexcited charge carriers exhibit Drude-like electric conductivity is made, which is relevant for three-dimensional bulk inorganic semiconductors at room temperature. The validity of the approximations is checked at a probe frequency of 1 THz for very short charge-carrier scattering time ($\tau \ll 1\,\mathrm{ps}$). Finally, in the absence of free charge carriers, the dielectric response of the films is assumed to be described by a constant real dielectric function (here $\epsilon_L = 10$ was used), which is a good assumption for materials without strong phonon mode response in the THz spectral region. To put the values of photoconductivity used in this section

into the context of experimental parameters, a material with sum charge-carrier mobility of $100\,\mathrm{cm^2V^{-1}s^{-1}}$ is used as a case study. In order to achieve DC photoconductivity of 100 $\Omega^{-1}\mathrm{cm}^{-1}$, charge-carrier density of around $6 \times 10^{18}\mathrm{cm}^{-3}$ has to be photoexcited (see Equation 4.8). In a 400 nm-thick thin film, uniformly photoexcited by a pulsed laser with wavelength of 800 nm, this charge-carrier density corresponds to a photoexcitation laser pulse (pump pulse) fluence of $\sim 60\,\mu\mathrm{J/cm^2}$, assuming that all photons are absorbed and that each photon photoexcites one electron-hole pair. Such charge-carrier mobility and sample thickness are similar to those observed in the materials studied in this thesis and excitation wavelength and excitation density are easily achievable with the laser system described in Section 3.4.1 of Chapter 3.

The photoconductivity of a thin film (which is not conductive in the absence of photoexcitation) can be calculated from an expression similar to that for the dark conductivity, given in Equation 4.10, but using the unexcited sample as a reference

$$\tilde{\sigma}_{\mathrm{photo}} = -\frac{\Delta T}{T + \Delta T}\frac{\epsilon_0 c(n_1 + n_3)}{L}\,, \tag{4.11}$$

where ΔT is the transient electric-field-transmission change between the photoexcited thin film and the reference sample in the dark ($T_{\text{pump-on}} - T_{\text{pump-off}}$) and T is the electric field transmission through the sample in the dark $T = T_{\text{pump-off}}$. For very small changes in transmission ($\Delta T \ll T$), caused by low photoconductivity of the sample, Equation 4.11 can be further approximated as [135]

$$\tilde{\sigma}_{\mathrm{photo}} = -\frac{\Delta T}{T}\frac{\epsilon_0 c(n_1 + n_3)}{L}\,, \tag{4.12}$$

an expression which is commonly used to calculate the photoconductivity of thin films from THz transmission measurements [30, 131–133, 152–154].

Figure 4.4 shows the deviation of the real part of the photoconductivity value calculated using Equation 4.11 from the value chosen to calculate the THz transmission function for

thin films with different values of dark conductivity. The presence of free charge carriers in the unexcited sample (used as reference) significantly affects the accuracy of the expression, even for purely real values of charge-carrier conductivity (Drude with scattering time $\tau \ll 1/\omega$). However, the linearity of the calculated photoconductivity with its exact value indicates that only the proportionality constant between the photoconductivity and $\frac{\Delta T}{T+\Delta T}$ term in Equation 4.11 is affected by the presence of dark conductivity. Furthermore, the assumption of a small change in transmission, used to derive Equation 4.12, is invalid for photoconductivity values above $\sim 10\,\Omega^{-1}\mathrm{cm}^{-1}$, as indicated by the red dotted line in the inset of Figure 4.4. The inset shows the relative error of the photoconductivity calculated from Equations 4.11 and 4.12.

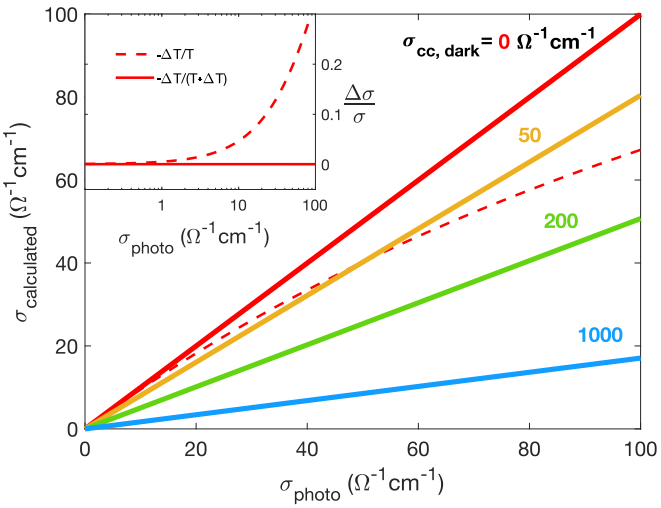


Figure 4.4: The deviation of the real part of photoconductivity calculated using Equation 4.11 ($\sigma_{\mathrm{calculated}}$) from its exact (chosen) value (σ_{photo}), obtained for a few different values of dark charge-carrier conductivity ($\sigma_{\mathrm{cc,\,dark}}$, indicated in $\Omega^{-1}\mathrm{cm}^{-1}$ in the colour of the relevant solid line). The red dotted line represents the photoconductivity at $\sigma_{\mathrm{cc,\,dark}} = 0$, calculated assuming negligible relative change of THz transmission between excited and unexcited film (Equation 4.12). The inset shows the relative error $\Delta\sigma/\sigma = (\sigma_{\mathrm{photo}} - \sigma_{\mathrm{calculated}})/\sigma_{\mathrm{photo}}$ of the photoconductivity values obtained from Equations 4.11 (solid line) and Equation 4.12 (dotted line) for dark conductivity $\sigma_{\mathrm{dark}} = 0$. The accuracy of the approximate expressions were calculated for the frequency of 1 THz ($\omega = 2\pi$ THz) for a 400 nm thin film deposited on a thick quartz substrate ($n_3 = 2.1$). The dielectric constant of $\epsilon_L = 10$ was used in the calculations to represent polarisation effect of the crystal lattice and the photoconductivity and dark conductivity due to free charge carriers in the film were assumed to be real (DC Drude conductivity).

Equation 4.11 is therefore suitable for photoconductivity estimates in the case of non-conductive thin films and that it provides a highly accurate value, even for high excitation fluences. Equation 4.12, however, can be used only for sufficiently low potoconductivities, lower than $10\,\Omega^{-1}\mathrm{cm}^{-1}$ in the case of 400 nm-thick films. Importantly, neither of the equations discussed above provides enough accuracy for calculating the photoconductivity of doped semiconductors, as has been previously pointed out by Burdanova et al. [155] These approximations assume a lack of conductivity of the unexcited sample, which is invalid in doped semiconductors. The analytical expression for photoconductivity given by Equation 4.17 is more appropriate in the case of conductive thin films, as discussed in the following section.

4.3.3 Photoconductivity of Conductive Films

Derivation

Using the approach presented by Nienhuys et al. [135], a simple analytical expression for calculating the photoconductivity of highly doped semiconducting thin films from THz-TDS data is derived. The derivation starts from the time-domain relation between the electric current $J(t)$ flowing through a photoexcited thin film ($L \to 0$) and the electric field incident ($E_{\mathrm{in}}(t)$) and transmitted ($E_{\mathrm{tr}}(t)$) through the film [135],

$$J^{\text{pump-on}}(t) = \frac{\epsilon_0 c}{L}[2n_1 E_{\mathrm{in}} - (n_1 + n_3)E_{\mathrm{tr}}^{\text{pump-on}}]\,, \tag{4.13}$$

where the thin film is placed on the boundary between two media with refracting indices n_1 and n_3, respectively (as illustrated in Figure 4.1). For a highly doped semiconducting thin film, the current flowing through the unexcited sample is then

$$J^{\text{pump-off}}(t) = \frac{\epsilon_0 c}{L}[2n_1 E_{\mathrm{in}} - (n_1 + n_3)E_{\mathrm{tr}}^{\text{pump-off}}]\,. \tag{4.14}$$

Combining Equations 4.14 and 4.13, and using a Fourier transform to obtain the frequency-dependent current $\tilde{J}(\omega)$ and electric field transmission $T(\omega)$ results in

$$\tilde{J}^{\text{pump-on}}(\omega) = \tilde{J}^{\text{pump-off}}(\omega) + \frac{\epsilon_0 c(n_1+n_3)}{L}[T_{\text{pump-off}} - T_{\text{pump-on}}]\,, \tag{4.15}$$

where $T_{\text{pump-on}}$ and $T_{\text{pump-off}}$ are the frequency-dependent THz electric field transmission functions through the photoexcited film and film in the dark, respectively. Using the definition of complex conductivity of the thin film, $\tilde{J}^{\text{pump-on}}(\omega) = \tilde{\sigma}_{\text{pump-on}} T_{\text{pump-on}}$ and $\tilde{J}^{\text{pump-off}}(\omega) = \tilde{\sigma}_{\text{dark}} T_{\text{pump-off}}$, leads to

$$\tilde{\sigma}_{\text{pump-on}} T_{\text{pump-on}} = \tilde{\sigma}_{\text{dark}} T_{\text{pump-off}} + \frac{\epsilon_0 c(n_1+n_3)}{L}[T_{\text{pump-off}} - T_{\text{pump-on}}]\,, \tag{4.16}$$

where $\tilde{\sigma}_{\text{pump-on}}$ is the total apparent conductivity of the photoexcited sample and $\tilde{\sigma}_{\text{dark}}$ is the dark conductivity of the film without photoexcitation, including the lattice conductivity.

Equation 4.16 can be rearranged to obtain the photoconductivity $\tilde{\sigma}_{\text{photo}}$, which is the difference of the total apparent conductivity of the photoexcited sample $\tilde{\sigma}_{\text{pump-on}}$ and apparent dark conductivity of the film $\tilde{\sigma}_{\text{dark}}$,

$$\tilde{\sigma}_{\text{photo}} = \tilde{\sigma}_{\text{pump-on}} - \tilde{\sigma}_{\text{dark}} = \left[\tilde{\sigma}_{\text{dark}} + \frac{\epsilon_0 c(n_1+n_3)}{L}\right] \frac{T_{\text{pump-off}} - T_{\text{pump-on}}}{T_{\text{pump-on}}}\,. \tag{4.17}$$

Assessment

Figure 4.5 shows the comparison of the photoconductivity calculated using Equation 4.17 with its exact value, and proves a very high accuracy of the analytical expression derived here, even for high values of dark conductivity and photoconductivity. The calculation was performed for thin films with Drude-type conductivity with very short charge-carrier scattering time (here τ=0 was used). Figure 4.7 further assesses this analytical formula for a few different charge-carrier scattering times, ranging between $2\pi\tau = 0.01\,\text{ps}$ and $2\pi\tau = 10\,\text{ps}$, and shows that the approximation yields a highly

accurate value of photoconductivity for dark conductivity and photoconductivity values as high as $10^4\,\Omega^{-1}\mathrm{cm}^{-1}$.

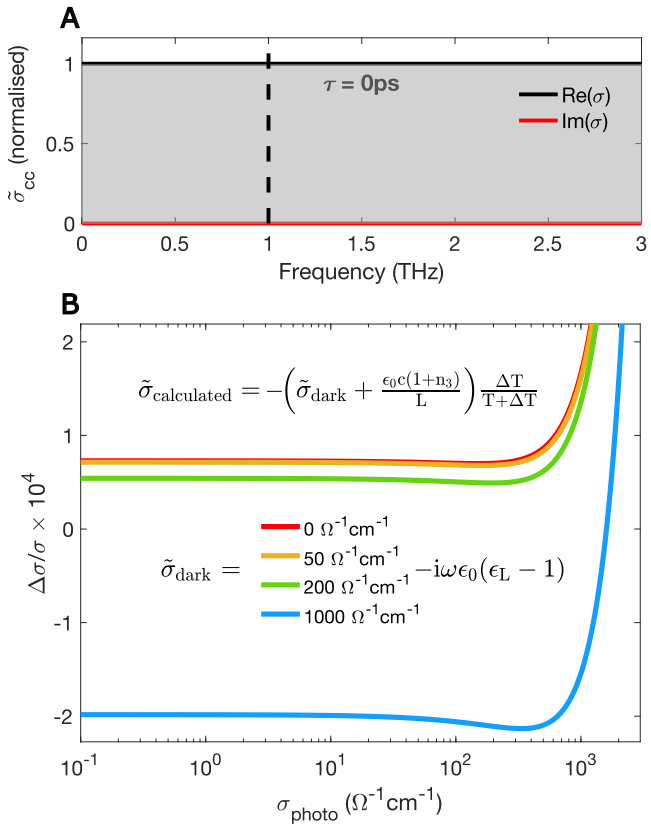


Figure 4.5: (A) Charge-carrier conductivity spectrum used for the assessment of Equation 4.17 for photoconductivity calculations. As illustrated in the figure, for Drude conductivity with very short charge-carrier scattering times, the conductivity due to carriers is purely real and spectrally flat. (B) The accuracy of the analytical expression for photoconductivity of highly doped thin films, shown in the figure and in Equation 4.17, calculated as the relative error of the real part of photoconductivity $\Delta\sigma/\sigma = (\sigma_{\mathrm{photo}} - \sigma_{\mathrm{calculated}})/\sigma_{\mathrm{photo}}$, similarly to the inset in Figure 4.4. The deviation was calculated for a 400 nm thin film with dielectric constant of $\epsilon_L = 10$ in the absence of free charge carriers, deposited on quartz, at frequency of 1 THz (indicated in panel A with black dotted line).

The analytical formula given by Equation 4.17, provides especially high accuracy of the calculated photoconductivity for semiconductors with short charge-carrier scattering time (and hence purely real charge-carrier conductivity), as evident from Figure 4.5 and Figure 4.7. Such short carrier scattering times have been observed in perovskite semiconductors [30], which together with the reported high dark conductivity values of tin-based perovskites ($\sim 150\,\Omega^{-1}\mathrm{cm}^{-1}$) [75] makes the approach presented in this

chapter particularly relevant to the field of electrically and chemically doped perovskites, discussed in the next two chapters.

4.4 Experimental Implementation

In this section, a simple experimental technique of estimating the apparent dark conductivity is discussed. The dark conductivity is necessary to calculate the time resolved photoconductivity of doped thin films in a optical-pump–THz-probe study. As discussed by Zhao and Chia [154], OPTP measurement is a 1D THz-TDS scan, in which the magnitude of a single-cycle THz pulse is measured at its peak for different pump-probe time delays. The measurement provides a frequency-averaged, time-dependent real part of the photoconductivity [154] of the sample.

In such experiment, Equation 4.17 can be used for photoconductivity calculations, with σ_{dark} estimated from relative THz transmission through the sample in the dark, as shown in Equation 4.10. In this equation, the electric field transmission through the sample T_{sample} is equal to the transmission in the dark in OPTP measurements, $T_{\text{dark}} = T$, leading to

$$\tilde{\sigma}_{\text{photo}} = -\left[\tilde{\sigma}_{\text{dark}} + \frac{\epsilon_0 c(n_1 + n_3)}{L}\right]\frac{\Delta T}{T + \Delta T} = -\frac{T_{\text{substrate}}}{T}\left[\frac{\epsilon_0 c(n_1 + n_3)}{L}\right]\frac{\Delta T}{T + \Delta T}. \quad (4.18)$$

Figure 4.6 shows the experimental transmission function of a THz pulse through perovskite thin films of different compositions (shown in coloured solid lines) and through a quartz substrate reference (shown by the black dotted line). The field strength of the transmitted pulse through tin-iodide perovskite (shown in red) is significantly reduced compared to lead-iodide perovskite (green). This difference in magnitude is caused by background hole doping present in tin-based perovskites [74, 75], which increases significantly the conductivity of the film in the dark. Upon addition of tin-fluoride to tin perovskite during deposition (shown to reduce the background doping [75, 79]), the THz electric

field transmission through the film increases (indicated by the yellow solid line), as expected for a less conductive sample.

The inset in the figure shows the real part of the Fourier-transformed transmission functions in the frequency space, shown in the colour corresponding to the relevant transmissions in the time domain. These data are presented as the relative transmission $\frac{T_{\text{reference}}(\omega)-T_{\text{sample}}(\omega)}{T_{\text{sample}}(\omega)}$, which is proportional to the real part of dark conductivity (see Equation 4.10). The relative transmission in the presented spectral region is relatively spectrally flat, owing to very short charge-carrier scattering time reported for these materials, about 1.7 fs [75]. According to Drude model of conductivity (Equation 4.8), the characteristic frequency (frequency for which the real part of conductivity decreases from its maximum DC value by a factor of 2) for such a material is of the order of 100 THz. As this frequency lies in the mid-IR range of the electromagnetic spectrum, unreachable by most THz spectroscopy setups, the THz TDS measurement in transmission mode probes directly the DC conductivity of perovskites (and similar materials with fs charge-carrier scattering time).

Next, the real dark conductivity of the thin films is estimated using only the magnitude of the transmitted THz pulse at its peak position, and the quantity $\frac{\max\left(E_{\text{reference}}(t)\right)-\max\left(E_{\text{sample}}(t)\right)}{\max\left(E_{\text{sample}}(t)\right)}$ is plotted in the inset of Figure 4.6 in dotted lines. Since the conductivity calculated from the peak of the transmitted time-domain THz pulse closely follows the frequency-averaged real part of the frequency-depended conductivity (weighted by the power spectrum of the probe - see Section 4.5.2), it is expected that the plotted quantity would approximate the spectrally flat conductivity of perovskites well. Indeed, a good agreement between this estimate and the frequency-averaged dark conductivity of the samples is found and recognise that this method of determining the real dark conductivity is sufficient to be used in OPTP measurements for samples with relatively short charge-carrier scattering time. Equation 4.18 can therefore be used with the $\frac{T_{\text{substrate}}}{T}$ term evaluated at the peak of the THz

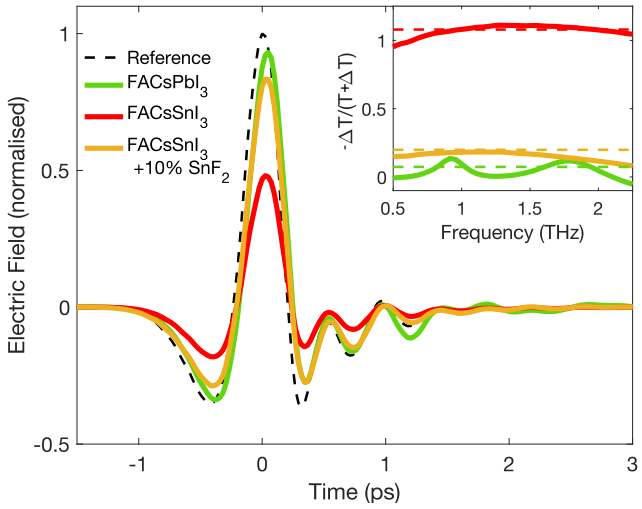


Figure 4.6: The dependence of time-domain THz field transmission through perovskite thin films on the chemical composition of the materials. The films of lead-based (green) and tin-based (red and yellow) metal-halide perovskites were deposited on quartz substrate. The field transmitted through tin-iodide perovskite with 10% tin fluoride added to the precursor solution is shown in yellow. Dotted black line represents the field transmitted through the bare substrate. All transmission functions were normalised with respect to the transmission through the quartz substrate reference, whose magnitude was set to 1 at the peak of THz pulse. The inset shows in solid lines the real part of relative complex transmission change, $\frac{-\Delta T}{T+\Delta T} = \frac{T_{\text{reference}} - T_{\text{sample}}}{T_{\text{sample}}}$, proportional to the real dark conductivity of the film. The dotted lines represent the relative transmission calculated from the field strength at the peak of the THz pulse.

pulse transmitted through the substrate and the sample, without the need for calculating the dark conductivity explicitly to account for its influence on photoconductivity.

Although this method provides very good accuracy when estimating frequency-averaged, real part of photoconductivity in OPTP experiment of semiconductors with short charge-carrier scattering time, more careful treatment is necessary when calculating the photoconductivity spectrum of samples with strong resonances in the THz spectral region [136]. To calculate the photoconductivity of such thin films, numerical fitting of the data using Equation 4.5 might be necessary [138], although in some cases one can follow the treatment presented by La et al.[136] It is also found that estimating the dark conductivity from the time-domain THz peak leads to a significant underestimate of the DC Drude conductivity in semiconductors with relatively long scattering times ($2\pi\tau > 1\,\text{ps}$, which includes inorganic semiconductors such as Si and GaAs), as discussed

in Section 4.5, and therefore spectral analysis of dark conductivity has to be performed in these materials. The method presented in this chapter, however, can be successfully used when investigating materials with short scattering times, making it particularly relevant to OPTP measurements of perovskites thin films and doped organic semiconducors.

Finally, the relative error of photoconductivity value calculated from Equation 4.11 is evaluated (caused by the assumption of negligible dark conductivity), using the example of tin-iodide perovskite $FACsSnI_3$. TDS data of this perovskite thin film is presented in Figure 4.6 in red solid line. Equation 4.18 is used to calculate the exact value of photoconductivity σ_{exact} (which provides a very good approximation as discussed in Section 4.3.3) and the exact value is compared with the approximated value σ_{approx}, calculated from Equation 4.11. This results in the relative error of photoconductivity σ (which due to the proportionality shown by Equation 4.8 is also the relative error of calculated charge-carrier mobility μ) given by

$$\frac{\Delta\mu}{\mu} = \frac{\Delta\sigma}{\sigma} = \frac{\sigma_{\text{approx}} - \sigma_{\text{exact}}}{\sigma_{\text{exact}}} = \frac{T}{T_{\text{substrate}}} - 1 \simeq -0.52, \tag{4.19}$$

where T represents the THz field transmission through the sample in the dark, here estimated from the peak of time-domain electric field transmission, shown in Figure 4.6 in red solid line. For this tin-iodide perovskite thin-film sample, assuming negligible dark conductivity and using Equation 4.11 for the calculation of photoconductivity would result in a large, 52% underestimate of photoconductivity (and therefore charge-carrier mobility), compared to its true value. This shows the significance of adapting more precise data analysis techniques, through either numerical data fitting or more precise approximations (such as Equations 4.17 and 4.18) when investigating properties of conductive thin films.

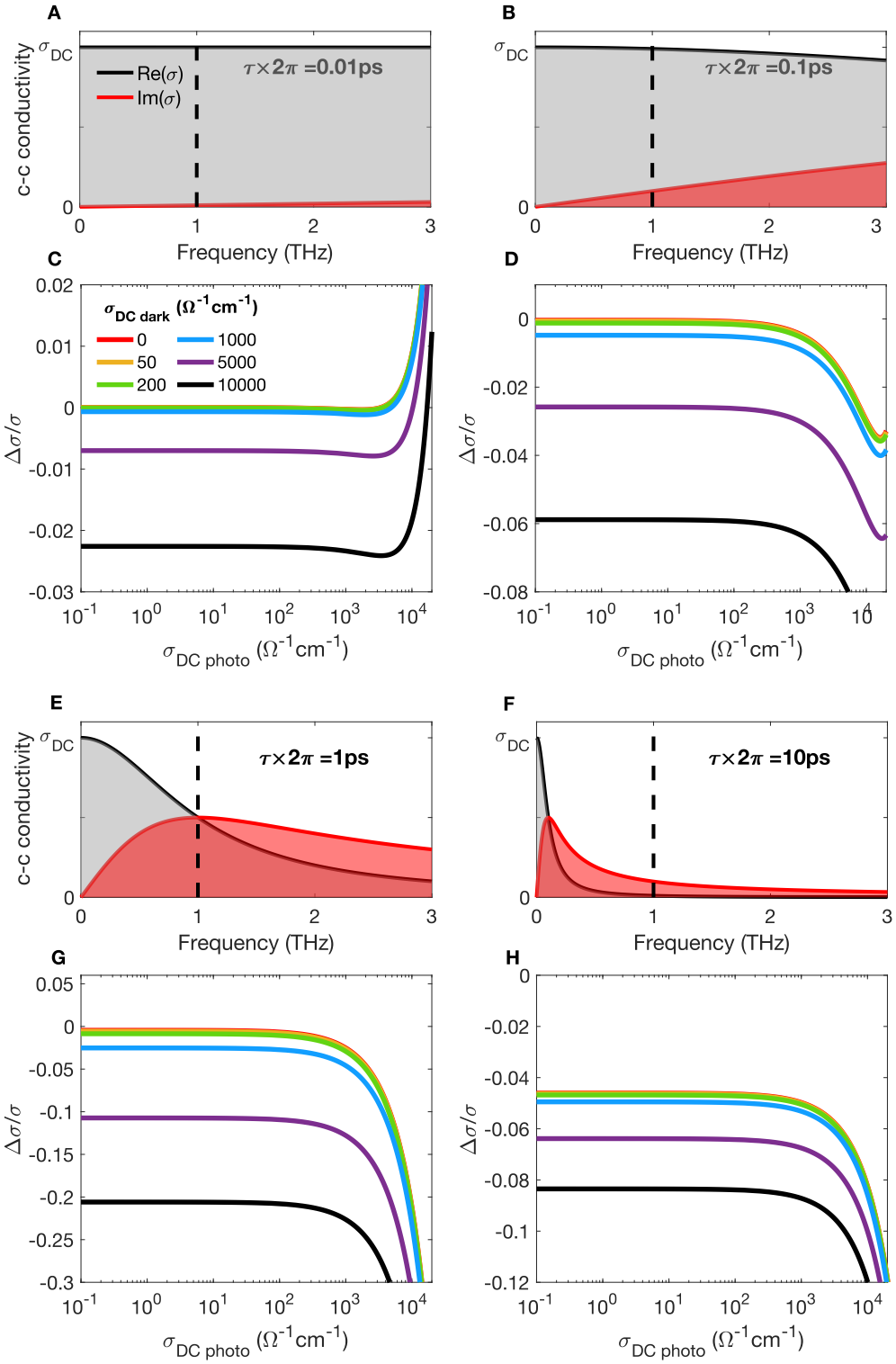


Figure 4.7: The effect of charge-carrier scattering time and dark conductivity value on the error of calculated photoconductivity. (A,B,E,F) Drude-type conductivity spectra of charge carriers and (C,D,G,H) the corresponding relative errors of photoconductivity calculated from Equation 4.17 are shown for thin films with different charge-carrier scattering times, varying between $2\pi\tau = 0.01$ ps and $2\pi\tau = 10$ ps. The relative error of the real part of photoconductivity, $\Delta\sigma/\sigma = (\sigma_{\text{photo}} - \sigma_{\text{calculated}})/\sigma_{\text{photo}}$, was calculated at frequency of 1 THz (marked with dotted line in the Drude conductivity spectra), for 400 nm thin films with dark DC charge-carrier conductivities indicated by the legend. A dielectric constant of $\epsilon_L = 10$ was used in the absence of charge carries. The errors are shown as functions of the DC conductivity of photoexcited charge carriers, which exhibit the same Drude conductivity as the background carriers introduced by doping.

4.5 Effects of Charge-Carrier Scattering Time

This section summarises the effects of charge-carrier scattering time on the transmitted spectra of THz radiation through semiconducting films. It shows the validity of equations derived in the previous sections for a wide range of semiconductors and assesses the accuracy of common photoconductivity extraction methods for various scattering times.

4.5.1 Assessment of Photoconductivity Estimates

In Section 4.3 the formula given by Equation 4.17 is validated using the example of a thin film, exhibiting Drude-type photoconductivity with very short charge-carrier scattering time ($\tau \to 0$). The conductivity of the charge carriers in such a semiconductor is purely real, and the only imaginary contribution to the apparent conductivity originates from the dielectric constant $\epsilon_L = 10$ (see Equation 4.7).

Here, the validity of this approximation is validated for a range of charge-carrier scattering times, to investigate the influence of the imaginary conductivity on the accuracy of the derived expression for photoconductivity. Figure 4.7 (C,D,G,H) shows the relative errors of the calculated real part of the photoconductivity, together with Drude conductivity spectra (A,B,E,F) used in the calculations. For the large range of charge-carrier scattering times, spanning 4 orders of magnitude, the new approximated expression for photoconductivity provides an accurate value of its real part up to a total conductivity of $\sim 10^3\,\Omega^{-1}\mathrm{cm}^{-1}$. Additionally, for very short scattering times, $2\pi\tau < 0.1\,\mathrm{ps}$, the expression is valid for dark- and photoconductivity values up to $\sim 10^4\,\Omega^{-1}\mathrm{cm}^{-1}$, above which the assumption of negligible optical thickness breaks down (as discussed in Section 4.3.1).

These findings imply that the presented approach can be used for a range of doped semiconducting thin films, with large background charge-carrier densities and various

charge-carrier scattering rates, making it extremely useful for investigating photoexcited charge-carrier dynamics of novel doped semiconducting materials.

4.5.2 Simulated Transmission Functions

Section 4.4 outlines a method of obtaining the real part of the dark conductivity from the peak of the time-domain THz pulse, using the example of perovskite thin films, which show relatively flat spectral response due to short charge-carrier scattering times. This method of estimating the dark conductivity for thin films with various conductivity spectra is evaluated, by simulating the time-domain transmission through thin-films and comparing the value obtained from the peak of the pulse to the DC Drude conductivity. Figure 4.8 shows the calculated time-domain transmissions and the spectra used in the simulations. The real conductivity extracted from the time-domain peak follows closely the spectral average (weighted by the power spectrum of THz pulse) of the real part of conductivity, but agrees with the DC conductivity only for the case of short charge-carrier scattering time ($2\pi\tau < 0.1\,\mathrm{ps}$). For semiconductors with longer scattering times this method leads to an underestimate of the DC conductivity value. Therefore, full spectral analysis of the photoconductivity is necessary to obtain the charge-carrier mobility in materials with long charge-carrier scattering time, although a time-dependent measurement of the peak's intensity (1D OPTP measurement) would still result in accurate estimates of charge-carrier decay dynamics.

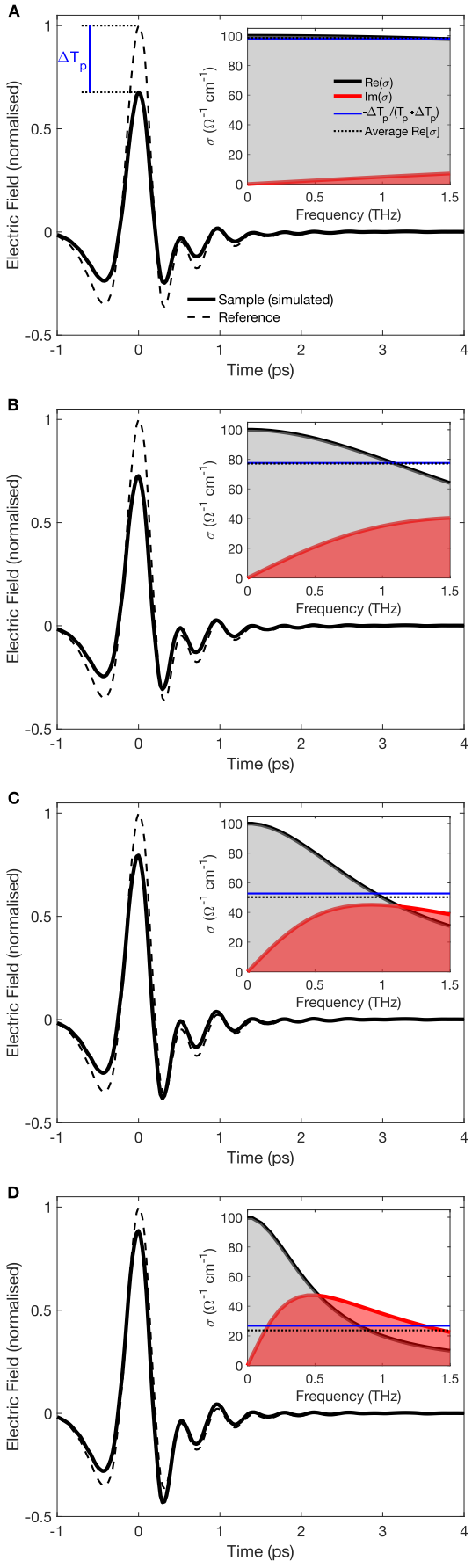


Figure 4.8: Simulated time-domain transmission function (black solid line) through 400 nm thin films with Drude conductivity, shown for charge-carrier scattering times of (A) $2\pi\tau = 0.1$ ps, (B) $2\pi\tau = 0.5$ ps, (C) $2\pi\tau = 1$ ps, and (D) $2\pi\tau = 2$ ps. The black dotted line represents the experimental transmission through bare quartz, used to calculate the time-domain field transmitted through the sample. The insets show the complex conductivity of the sample used in the calculations. In the insets, the blue straight line represents the real conductivity, estimated using $-\Delta T/(T+\Delta T)$ value from the peak of the THz pulse. The black dotted line shows the averaged value of the real part of conductivity, weighted by power spectrum of the terahertz pulse used in the experiment. The lattice contribution to the dielectric response of $\epsilon_L = 10$ was used for all samples.

4.6 Conclusions

In this chapter, the validity of approximations commonly used to calculate conductivity of thin films from THz-TDS data has been assessed. It was found that the simple analytical expression for complex conductivity, shown by Equation 4.10, provides a highly accurate approximation of the real dark conductivity of thin films with low dielectric constant, up to conductivity values of the order of $10^4\,\Omega^{-1}\mathrm{cm}^{-1}$. However, when calculating the photoconductivity of highly doped thin films (with conductivity comparable to $\sim 100\,\Omega^{-1}\mathrm{cm}^{-1}$), the expression commonly used in the literature (Equation 4.11) results in a significant deviation of the calculated quantity from its exact value, leading to an underestimation of photoconductivity and hence the charge-carrier mobility.

A simple correction to the analytical expression (Equations 4.17 & 4.18) was derived, that eliminates this deviation and can be used for photoconductivity calculations of doped semiconductors, within the regime of optically thin films (up to a conductivity of $10^4\,\Omega^{-1}\mathrm{cm}^{-1}$). An experimental method of implementing this correction was found for semiconductors with sub-picosecond charge-carrier scattering times, which can be used in OPTP experiments to provide the frequency-averaged photoconductivity response, accounting for even very high background dark conductivity of the material.

This computational study gives practical insights into the limitations of commonly used assumptions when calculating the conductivity of thin films from THz-TDS data, and provides an approximation yielding highly accurate values of photoconductivity in doped semiconductive thin films. These results are extremely relevant when investigating properties of novel materials, allowing much higher precision of photoconductivity calculations without the need for numerical fitting of data. This investigation can be used as a guide for choosing the best-suited data analysis method for a variety of THz-TDS studies.

5

Hot Carrier Thermalisation Dynamics in Doped Tin-Iodide Perovskites

Contents

5.1 Introduction 84
5.2 Background 84
5.3 Results and Discussion 88
5.3.1 Charge-Carrier Dynamics 90
5.3.2 Chemical Doping 95
5.3.3 Push Energy Dependence 99
5.3.4 Spectral Analysis of Conductivity 101
5.4 Conclusion 105

The work presented in this chapter has been published in: A. M. Ulatowski, M. D. Farrar, H. J. Snaith, M. B. Johnston, L. M. Herz. 'Revealing Ultrafast Charge-Carrier Thermalization in Tin-Iodide Perovskites through Novel Pump–Push–Probe Terahertz Spectroscopy', *ACS Photonics*, **2021**, *8* (8) 2509-2518 (Ref. [83]).

5.1 Introduction

In this chapter of the thesis, the effect of doping on the charge-carrier cooling dynamics in perovskite semiconductors is investigated in detail through novel pump-push-probe (PPP) spectroscopy. As explained in Section 2.2.2 of Chapter 2, tin-iodide perovskites exhibit spontaneous hole doping, which originates from tin-vacancies, common point defects in these materials. Using tin fluoride during thin film deposition can reduce the propensity to defect formation (and therefore dopant concentration), making tin-iodide perovskite an ideal system to investigate the influence of doping on hot-carrier dynamics, highly relevant for future-generation hot carrier PV.

The novel experimental scheme, PPP spectroscopy with THz conductivity probe (described in detail in Chapter 3), allows for investigation of the dynamics of charge carriers brought into non-equilibrium by an infrared "push" pulse. It is found that in both chemically- and photo-doped $FA_{0.83}Cs_{0.17}SnI_3$ thin films the IR push pulse illumination (and the ensuing increase in hot carrier population density) leads to reduced THz conductivity due to stimulated THz emission. This chapter reveals that hot carriers dissipate their energy on a sub-picosecond timescale through carrier-carrier scattering events, largely enhanced by the presence of cold ocean of holes, currently unavoidable in $FA_{0.83}Cs_{0.17}SnI_3$ perovskites.

5.2 Background

As outlined in Chapter 2, metal-halide perovskites have received significant attention from the scientific community over the last decade because of their excellent optoelectronic properties, including high absorption coefficients [156], long charge-carrier diffusion lengths [40, 80, 90] and low exciton binding energies [34–36], which make them well suited to photovoltaic (PV) applications. Since the first implementation of lead-free perovskites

in PV [74, 157], intense research has investigated the properties of tin-iodide perovskites, which promise higher fundamental charge-carrier mobilities than archetypal $MAPbI_3$ [25, 158] as well as an absence of toxic lead. However, the most significant challenge for tin-containing perovskites is the formation of tin vacancies and iodide interstitials [46, 159–161], which induce hole self-doping of the material and promote oxidation of Sn^{2+} to Sn^{4+}, commonly reported in the literature [82, 162]. This self-doping effect increases the recombination rate of photoexcited charge carriers and reduces the charge-carrier mobility of the perovskite through the introduction of additional charge-scattering processes [51, 75]. Several additives have been shown to reduce tin vacancy formation and tin oxidation [79, 81, 161, 163–166], which has led to efficient tin-iodide perovskite PV devices. Interestingly, these investigations have also yielded perovskite semiconductors with controllable hole doping levels [51, 75, 166], which is still an elusive goal in most lead halide perovskites because of their low barriers to ionic migration and the associated phase segregation [167, 168], as well as defect compensation effect described in Chapter 2.

In addition to their advantageous properties of non-toxicity and high charge-carrier mobility, tin halide perovskites have also been postulated to exhibit slow cooling of hot charge carriers following above-gap excitation, lasting tens of picoseconds [111] to nanoseconds [110, 112]. Slow carrier cooling times may potentially allow for more efficient harvesting of the energy of hot carriers [12] in suitably designed hot-carrier solar cell architectures with efficiencies that could exceed the standard efficiency limit for a device operating in thermal equilibrium [169] (see Chapter 2 for details). However, to assess the potential of this technology, the full dynamic energy exchange and loss processes of hot carriers needs to be understood as they ultimately define the intrinsic voltage losses that could be averted in a non-standard device geometry. Following above-bandgap photoexcitation, charge carriers quickly exchange their energy through carrier-carrier scattering, leading to a broad Maxwell-Boltzmann distribution of charge carriers in their

respective bands that is characterised by a temperature T_c, higher than that of the lattice [87]. This so-called thermalization process has been investigated in lead-halide perovskites through two-dimensional electronic spectroscopy and was shown to last tens of femtoseconds. An increased charge-carrier concentration and excess energy of the excitation was shown to accelerate the dynamics because of the concomitant increase in carrier-carrier scattering rates [121]. Following this thermalization process, charge carriers cool to the lattice temperature in a slower process dominated by interactions with optical and acoustic phonons. During this process, the excess energy of carriers in the high-energy tail of the Maxwell-Boltzmann distribution can be extracted in a suitably designed hot-carrier device, [12] indicating that materials with slow carrier cooling would allow for higher efficiency of this energy harvesting process. Such charge-carrier cooling times have been investigated for metal-halide perovskites with ultrafast photoluminescence and transient absorption spectroscopy, with reported timescales ranging from hundreds of femtoseconds [93] to tens of picoseconds [111], with some reports of nanoseconds lifetimes [97, 110, 112]. Importantly, cooling timescales were prolonged by higher charge-carrier densities through carrier-carrier scattering, and by excess excitation energies because of the phonon bottleneck effect, for which a build-up of hot phonons prevents effective transfer of thermal energy from charge carriers to the surrounding lattice.

While the abovementioned investigations of charge-carrier thermalization and subsequent cooling dynamics have provided interesting fundamental insights, they unfortunately do not fully reflect the intraband relaxation processes encountered in a photovoltaic cell operating under solar illumination conditions. The majority of studies investigating hot-carrier relaxation dynamics have utilized short excitation pulses with a relatively narrow spectrum (compared with sun light) to create a substantially larger population of non-equilibrium charge carriers than present in a photovoltaic device during operation, with a sharp energy distribution above the bandgap [97, 110–112, 121]. This scenario

is fundamentally different to hot-carrier relaxation processes in photovoltaic devices, in which any charge carrier newly created with excess energy above the band gap encounters an already present thermalized population of cooled carriers that had been created by the continuous, broad-band illumination of sunlight some time ago. As pointed out by Richter et al., [121] newly created non-equilibrium charge-carrier pairs may therefore scatter effectively with an already present ocean of cold electrons and holes, meaning that their excess energy will be transferred to a larger population of carriers through a fast thermalization processes, reducing the overall temperature of the carrier gas much quicker than any study using a narrowband resonant excitation would imply. Such interactions of hot carriers with cold carriers have been studied in perovskites only at very high non-equilibrium photoexcitation densities [170–173], for which relaxation rates may still be dominated by carrier-phonon interactions, slowed down by the hot phonon bottleneck effect. Moreover, no such studies have been performed on tin-iodide perovskites, in which the inevitable self-doping and the ensuing thermalized hole population in the valence band can exacerbate scattering processes between hot and cold carriers. Such materials with a high propensity towards self-doping therefore require a particularly careful assessment of their suitability for hot-carrier extraction devices, as the very large population of cold holes on the top of the valence band can effectively absorb the energy of a relatively small population of hot carriers photoexcited by solar illumination. Because of the large imbalance between the charge-carrier density injected under solar illumination conditions ($\sim 10^{16}\,\mathrm{cm}^{-3}$) [80], and the background doping density typically present in tin iodide perovskites ($\sim 10^{17}$ – $10^{20}\,\mathrm{cm}^{-3}$) [21] rapid thermalization of photoinjected charge carriers would be expected to only marginally increase the temperature of the carrier gas available for above-bandgap extraction. Determining the rate at which such interchange occurs is therefore important for the assessment of tin iodide perovskites for hot-carrier photovoltaic applications.

In this chapter, the intraband relaxation processes in $FA_{0.83}Cs_{0.17}SnI_3$ thin films is investigated, for the first time using a novel ultrafast pump-push-probe technique. The controllable level of doping in tin-iodide perovskites through tin-fluoride addition [51, 75] is exploited to examine the impact of cold charge-carrier gas on the relaxation dynamics of hot carriers. This newly developed Optical-Pump–IR-Push–THz-Probe spectroscopy is shown to be a powerful tool that can be used to reveal the effects of intrinsic chemical doping and transient photo-doping on the terahertz conductivity following the illumination of the material with an ultrafast sub-bandgap, infrared excitation pulse. A transient decrease of conductivity upon this IR excitation in both photo- and chemically doped materials is reported and associated with intraband photoexcitation of free charge carriers and their subsequent interaction with the THz probe. Such non-equilibrium charge carriers subsequently relax towards the edges of their respective bands, with timescales of hundreds of femtoseconds depending strongly on the excess energy provided by the IR “push" pulse. For the relatively low densities of generated non-equilibrium charge carriers, the hot-phonon bottleneck effects are absent, with intraband energy loss deriving mostly from scattering with already present cold electrons and holes, which competes with carrier–phonon scattering. Finally, the origin of negative THz photoconductivity is investigated in a literature context [155, 174–178], and stimulated THz emission from pushed charge carriers is found to be most likely responsible for the observed negative photoconductivity response to intraband excitation.

5.3 Results and Discussion

The investigation starts with a determination of the doping level present in thin films of tin-iodide perovskite using terahertz time-domain spectroscopy (THz-TDS), for which single-cycle THz radiation acts as a non-contact probe of the conductivity of the thin film [49]. The transmission of this radiation through a thin film sample is measured using an optical

gating method, described in Chapter 3. By comparing the sample's transmission with the transmission through a bare substrate, the frequency-dependent conductivity of the thin film was calculated using Equation 4.10 from Chapter 4 [137, 138], using L =400 nm as the films' thicknesses, previously determined for these sets of samples [51], and $n_{\text{substrate}}$=2.1 as the refractive index of the z-cut quartz substrate [125] placed in vacuum.

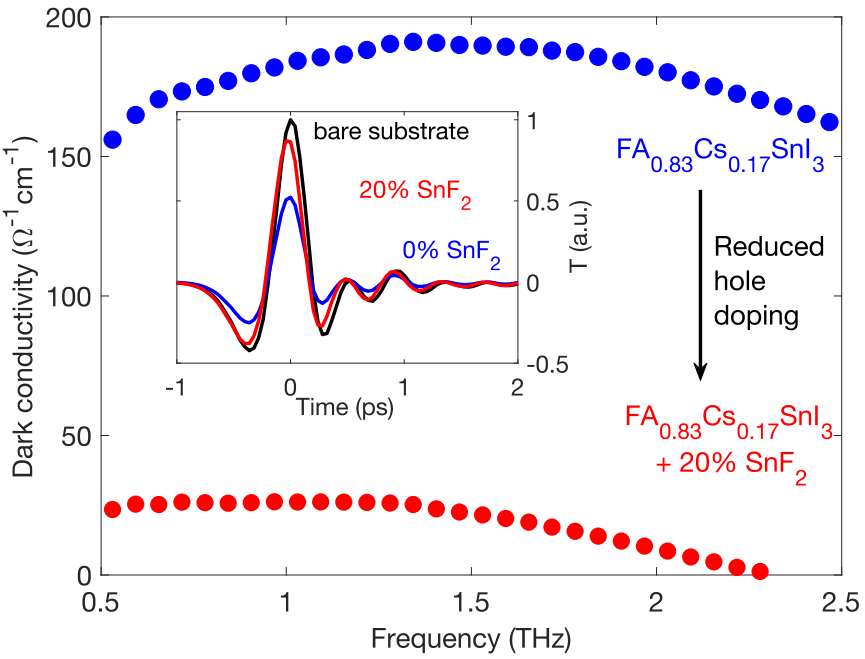


Figure 5.1: The effect of tin-fluoride addition to $FA_{0.83}Cs_{0.17}SnI_3$ perovskite on the THz dark conductivity spectrum of thin films. Filled blue and red circles show the real part of the THz conductivity in the absence of photoexcitation, for $FA_{0.83}Cs_{0.17}SnI_3$ films fabricated when either no or 20% SnF_2 had been added to the precursor solution, respectively. The inset displays the corresponding time-domain electric field strength T of the transmitted THz probe through the thin films (blue and red lines) and through a bare z-cut quartz substrate (black line).

Figure 5.1 shows the calculated conductivity spectra in the dark (no photoexcitation) of $FA_{0.83}Cs_{0.17}SnI_3$ thin films for the two cases of either no (blue filled circles) or 20% (red filled circles) of tin fluoride having been added to the precursor solution during deposition (performed by Michael D. Farrar, Optoelectronic Devices Group, Department of Physics, University of Oxford - see Sample Fabrication in the Appendix A for film processing details). As seen in the figure, the addition of the SnF_2 significantly reduces

the dark conductivity of tin iodide perovskite films by suppressing the presence of tin vacancies and the concomitant hole self-doping of the material [51, 79, 161]. When 20% SnF_2 has been added, the remnant conductivity spectrum mostly reflects contributions from broad optical tin-iodide phonon modes, as discussed previously [51]. The inset of this figure shows that the high conductivity of the $FA_{0.83}Cs_{0.17}SnI_3$ thin film with no tin-fluoride added leads to a reduction of the electric field strength of the transmitted THz probe, here shown in the time-domain. Upon addition of tin fluoride to the perovskite during deposition, a similar transmission to that of the bare quartz substrate is recovered, indicating negligible conductivity of the thin film. Using an analysis of THz transmission through these thin films (discussed in Chapter 4) [51, 128], a background doping density of $5\times10^{19}\text{cm}^{-3}$ is determined for the $FA_{0.83}Cs_{0.17}SnI_3$ film without tin-fluoride additive. Existing studies evaluating tin vacancy suppression methods in tin-halide perovskites have found that the minimal doping levels achievable through tin-fluoride addition in these materials are $>10^{17}\text{cm}^{-3}$ [74–76, 79]. In this case, in the $FA_{0.83}Cs_{0.17}SnI_3$ thin film fabricated with 20% SnF_2 addition, the doping concentration falls below the level detectable within the measurement accuracy ($\sim2\times10^{18}\,\text{cm}^{-3}$) [51], therefore the two samples (with 0% SnF_2 and 20% SnF_2 added) represent two convenient scenarios of the highest and lowest hole doping densities attainable in tin-halide perovskites. It is worth noting, however, that even in the perovskite film to which 20% SnF_2 had been added during fabrication, the doping level is high when compared with the density of photoexcited charge carriers typically present under solar illumination ($\sim10^{16}\,\text{cm}^{-3}$) [80].

5.3.1 Charge-Carrier Dynamics

The dynamics of the transient photoinduced conductivity is next probed for $FA_{0.83}Cs_{0.17}SnI_3$ in the presence of high and low hole doping levels. An extension of the abovementioned THz TDS technique, Optical-Pump–THz-Probe (OPTP) spectroscopy, has been widely

used in recent years to investigate charge-carrier dynamics over picosecond-to-nanosecond timescales in perovskite semiconductors [30, 31, 131–134]. In this type of experiment, a semiconducting perovskite is photoexcited with an ultrafast (tens of fs) optical laser pulse with above-bandgap photon energy, and its photoinduced conductivity subsequently probed with a THz pulse. By using optical delay stages, this method allows mapping of the photoconductivity transient with sub-picosecond time resolution, revealing charge-carrier recombination dynamics and mobility [80], as described in Chapter 3. In this chapter, a novel approach is demonstrated to extend this technique by adding an additional ultrafast infrared pulse, a so-called “push", which induces low-energy optical transitions in an already photoexcited material [170, 172, 173]. A schematic diagram of this experiment is shown in Figure 5.2A, in which a thin film deposited on a quartz substrate is first photoexcited by an optical pump pulse (red), secondly illuminated with an IR push pulse (black) and finally probed with THz radiation (blue). The timings between the pump and push pulse arrival (t_1) and push and probe arrival (t_2) are controlled with optical delay stages. Crucially, such Optical-Pump–IR-Push–THz-Probe (PPP) experiments allow probing intraband transitions, such as those leading to charge-carriers being “pushed” higher within their band, and their subsequent relaxation back towards the band edge.

Figure 5.2B demonstrates the effect of such push pulses on the transient photoconductivity of an $FA_{0.83}Cs_{0.17}SnI_3$ thin film for which self-doping had been suppressed by addition of 20% SnF_2 during the fabrication process [51]. Here, the sample is photoexcited with a 800 nm laser pulse (arriving at a nominal delay of -5 ps) which results in generation of free charge carriers and an associated sharp rise in photoconductivity. The transients were measured for different excitation fluences varying between 16 μJ/cm^2 (red line) and 111 μJ/cm^2 (blue line), with increased initial free charge-carrier generation leading to an expected increase in photoinduced conductivity. An IR push pulse of 1450 nm wavelength arrives 5 ps later, at nominal time=0, and causes a distinct feature, a short drop of

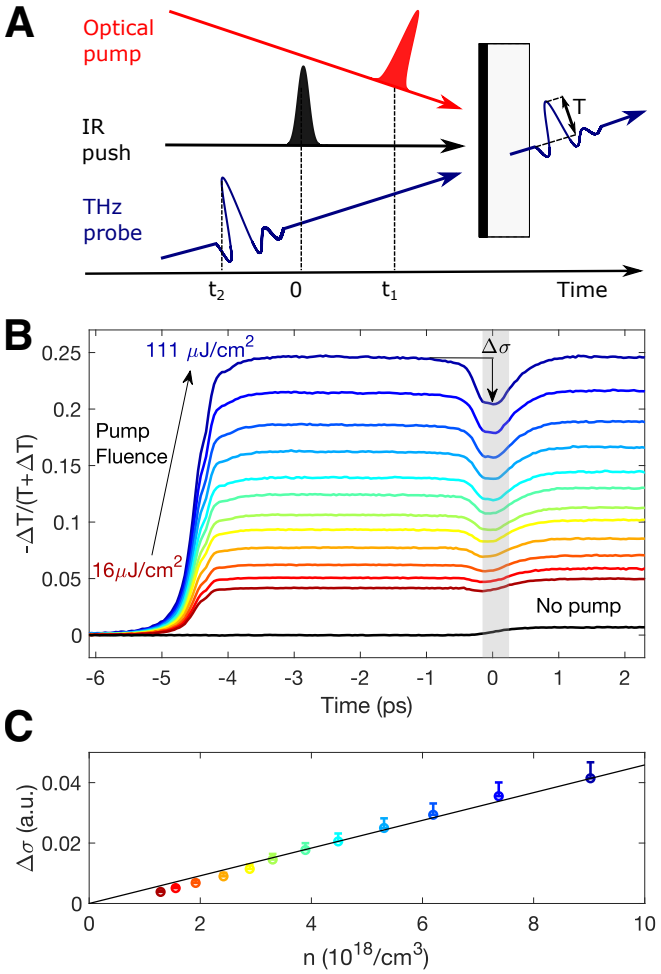


Figure 5.2: Optical-Pump–IR-Push–THz-Probe (PPP) experiments on $FA_{0.83}Cs_{0.17}SnI_3$ thin film with low hole doping (20% SnF_2). **A** Schematic diagram of the PPP experiment featuring a thin-film sample deposited on a transparent substrate, photoexcited with an ultrafast laser pulse of above-bandgap photon energy (the "pump") and subsequently illuminated by an infrared pulse (the "push") and THz radiation (the "probe") in order to determine its time-dependent conductivity. **B** Time-dependent photoconductivity transients measured in such experiment for an $FA_{0.83}Cs_{0.17}SnI_3$ thin film, fabricated with an addition of 20% SnF_2 to the precursor solution. The negative value of the relative change in THz field amplitude transmission ($-\Delta T/(T+\Delta T)$) is proportional to the change in conductivity. The colours of the transients correspond to different fluences of the initial 800 nm wavelength pump photoexcitation, which arrives at time=−5 ps. The IR push pulse of 1450 nm wavelength arrives at time=0. **C** Dependence of the push-induced conductivity change on the initially photoexcited charge-carrier density n. Here, the push-induced decrease in conductivity $\Delta\sigma$ is evaluated as the average photoconductivity change recorded over the grey-shaded region shown in (B) from which the average photoconductivity before the push arrival and the effect of push-pulse excitation only (pump beam blocked - black solid line) had been subtracted. The initially generated charge-carrier density n has been estimated from the fluence of the pump and absorption data, assuming 100% photon to charge-carrier pair conversion. The error bars represent measurement uncertainty due to laser power drift over the time of the experiment.

conductivity, denoted $\Delta\sigma$ in the figure. This negative photoconductivity recovers to the original value (before the IR pulse arrival) on sub-picosecond timescales. As detailed further below, this transient negative conductivity likely results from THz stimulated emission, generated when free electrons are excited higher into the conduction band by the IR push pulse (or in the case of holes, lower into the valence band), after which they interact with the THz radiation, emitting photons of energy matching those of the THz probe. These "pushed" hot carriers subsequently relax towards the edge of the band, reflected by the timescale of the decay of the transient THz conductivity change. The recovery of the original photoconductivity value also demonstrates that such non-equilibrium charge carriers are retained as free carriers in the conduction band, suggesting an absence of hot-carrier trapping mechanisms that has previously been observed through transient absorption spectroscopy in $MAPbBr_3$ and $MAPbI_3$ nanocrystals [172]. It is therefore demonstrated that bulk tin iodide perovskite appears to be less susceptible to such detrimental effects, possibly as it offers lower surface-to-volume ratio than nanocrystalline materials. Furthermore, the attribution of the push-induced conductivity drop $\Delta\sigma$ to intraband optical excitations of free charge carriers is supported by its magnitude being directly proportional to the density of photoexcited charge-carrier pairs n, as shown in Figure 5.2C. A very small rise of conductivity after the push arrival can be seen even if no pump pulse had arrived prior to the push (black curve in Figure 5.2B). The fluence-dependence of this push-induced conductivity change was measured using a variable ND filter wheel in "push-probe" (without pump) experiments to determine its origin. Figure 5.3A shows the photoconductivity onset for a $FA_{0.83}Cs_{0.17}SnI_3$ thin film for which 20% SnF_2 had been added during fabrication (low doping level). The sample was illuminated at time=0 with 1390 nm wavelength IR push pulses. The positive photoconductivity indicates that excitation across the bandgap had occurred, which may be caused by two-photon excitation. Figure 5.3B shows the integrated photoconductivity

from the greyed-out region of figure 5.3A as a function of push pulse fluence. The quadratic dependence of the positive photoconductivity on the excitation fluence indeed indicates that a two-photon absorption process is responsible for the across-bandgap charge-carrier excitation [179, 180]. This two-photon absorption obscures the dynamics of the photoconductivity transient upon IR pulse arrival. In order to fully account for this effect and to extract the lifetime of the decreased conductivity, a full investigation of the dependence of the two-photon absorption on the push-fluence as well as the initial pump-fluence would need to be performed. Fortunately, as shown in Figure 5.4 and as also visible in Figure 5.5, no such two-photon absorption is evident in the highly doped $FA_{0.83}Cs_{0.17}SnI_3$ thin film (no tin fluoride added). This lack of increased conductivity after the IR pulse arrival could be caused by the lower charge-carrier mobility for the highly doped perovskite compared with that of the thin film made with tin-fluoride additive, as well as a blue-shifted absorption spectrum of the doped film resulting from Burstein-Moss effects [51]. A lower charge-carrier mobility implies a lower conductivity for the same amount of two-photon excitation and a blue-shifted absorption spectrum may result in reduced IR absorption. Therefore, a careful assessment of the hot-carrier cooling dynamics was based on the measurements performed on the highly doped tin-based perovskite (no tin-fluoride additive) as detailed below.

In this pump-push-probe scheme, an ultrafast photoexcitation pulse was used, with photon energy just above the measured bandgap of these materials [51]. Because of the sufficiently slow charge-carrier recombination dynamics observed in $FA_{0.83}Cs_{0.17}SnI_3$ with 20% SnF_2 added [51], the photoinduced conductivity of the material is almost constant over timescales of the order of a few picoseconds, as evident from Figure 5.2B. The pulsed excitation ("pump") has benefits in terms of allowing an extraction of charge-carrier mobilities from OPTP, however, an interesting extension of the technique could also

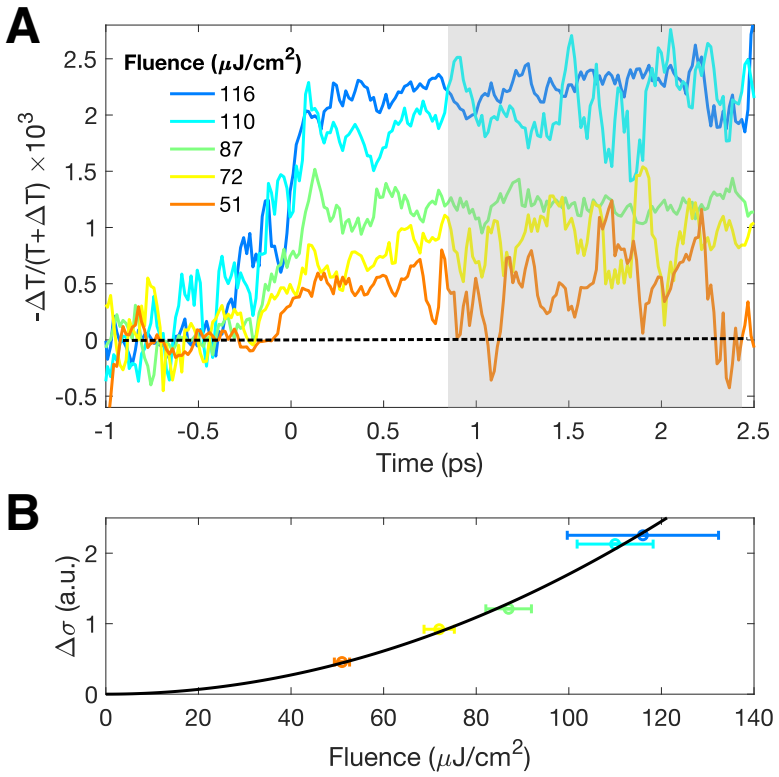


Figure 5.3: **A** Positive photoconductivity onset at the push arrival (time=0) measured for a $FA_{0.83}Cs_{0.17}SnI_3$ thin film produced with 20% SnF_2 added during fabrication (low doping level). The fluence of the IR push pulses is indicated in the legend and the greyed-out region was used to obtain the average photoconductivity value $\Delta\sigma$ after the signal onset. **B** The magnitude $\Delta\sigma$ of the photoconductivity after the arrival of the push pulse is plotted against the excitation fluence. The error bars represent the uncertainty of the laser power measurement and the solid black line shows a quadratic fit passing through the origin, i.e. $\Delta\sigma = a \times \text{Fluence}^2$.

be offered by an implementation of alternate, either continuous wave (CW) or pulsed "pump" excitation, with the former resembling solar illumination even more closely.

5.3.2 Chemical Doping

To examine further such IR-push-induced transitions of free charge carriers within a band, the transient conductivity dynamics is explored for a $FA_{0.83}Cs_{0.17}SnI_3$ thin film produced without tin-fluoride addition during deposition. Since this film exhibits a very high conductivity owing to background hole doping (Figure 5.1), the valence band is already partially filled with holes, obviating the need of initial photoexcitation. The photoconductivity transients were therefore acquired with the pump beam blocked,

measuring solely the effect of an IR push pulse on the conductivity of the sample (push-probe only). Figure 5.4A shows that a negative push-induced photoconductivity is observed, whose recovery dynamics are highly similar to those following the push-induced change in pump-induced conductivity of the $FA_{0.83}Cs_{0.17}SnI_3$ film with low doping density discussed above.

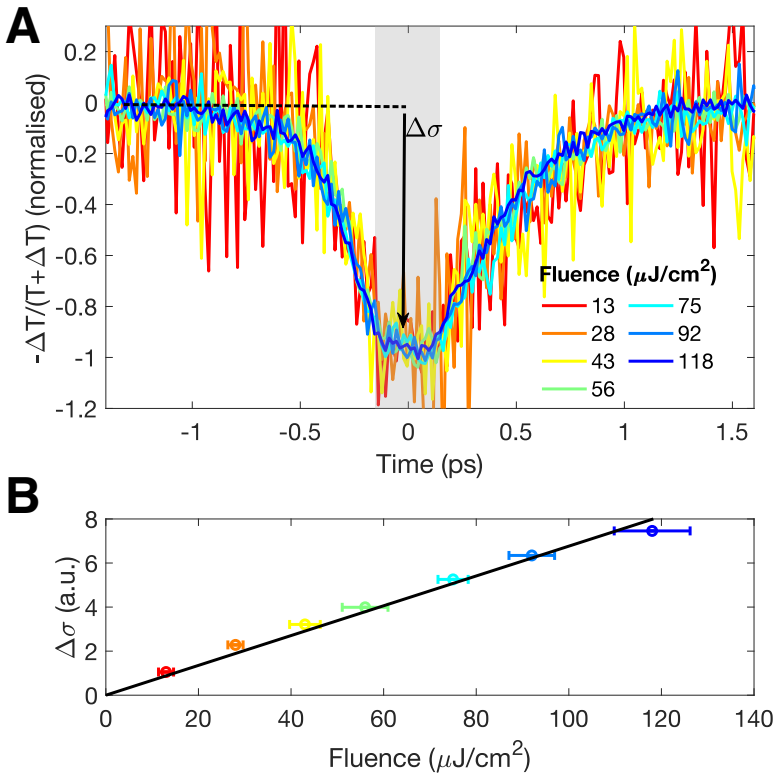


Figure 5.4: Push-only (pump beam blocked) photoconductivity transients for a $FA_{0.83}Cs_{0.17}SnI_3$ thin film with high hole doping (no tin fluoride additive). A Presented transients were induced by sub – bandgap photoexcitation centred at 1390 nm wavelength with excitation fluences indicated in the legend. The relative change in THz field transmission ($-\Delta T/(T+\Delta T)$) is proportional to the change in conductivity of the thin film. Traces were normalised for all fluences to a value of -1 at the peak. The magnitude of the push-induced change of conductivity $\Delta\sigma$ was evaluated by averaging the signal strength over the greyed-out region of the unnormalized traces. **B** The magnitude of the photoconductivity $\Delta\sigma$ after push arrival is plotted against the excitation fluence. The error bars represent the uncertainty of the laser power measurement and the solid black line shows a linear fit passing through the origin ($\Delta\sigma = a \times \text{Fluence}$).

Through variation of the fluence of the IR push pulse between 13 μJ/cm^2 and 118 μJ/cm^2, it is further found that the magnitude of the negative photoconductivity

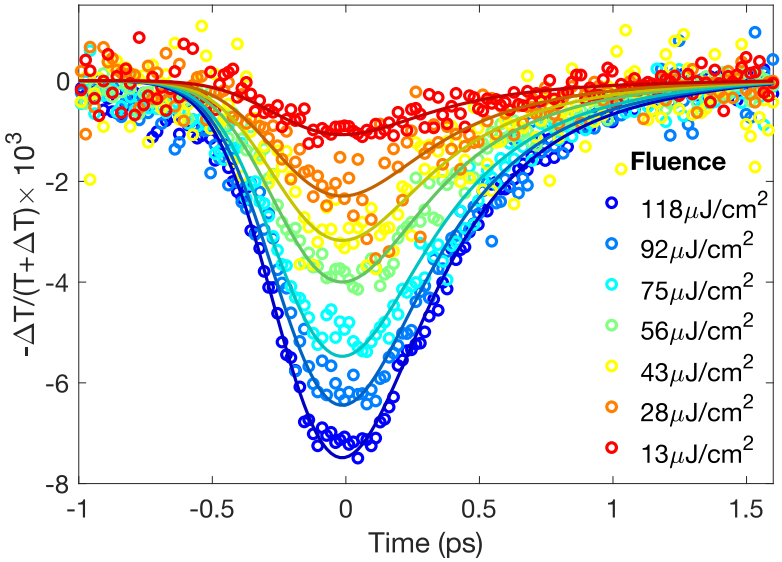


Figure 5.5: Negative photoconductivity transients near time=0 of a $FA_{0.83}Cs_{0.17}SnI_3$ thin film with no SnF_2 added during fabrication (high doping level). The empty hoops represent the measured photoconductivity data and solid lines show fits of a monoexponential decay convoluted with Gaussian broadening. The standard deviation of the Gaussian (representing system resolution) was determined as s=200 fs, as described Appendix A. The fit to the highest fluence data yields a decay time of τ=357 fs±10 fs for the relaxation process. This decay lifetime is then fixed for fitting lower fluence transients due to the lack of decay dynamics dependence on the push fluence demonstrated in Figure 5.4.

is proportional to the intensity of the IR push pulse, as demonstrated Figure 5.4B, indicating a single-photon intraband excitation. Therefore, regardless of the way in which free carriers are generated, whether through photoexcitation or chemical doping, an IR push induces intraband transitions of these charge carriers, leading to a temporal population of non-equilibrium carriers higher in the band.

These transients are further analysed in order to determine the mechanism of the subsequent relaxation process following the IR-push pulse excitation. A mono-exponential decay function is convoluted with Gaussian broadening, reflecting the temporal resolution of the system, to fit to the photoconductivity transients (as detailed in Appendix A). These fits are shown in Figure 5.5 as solid lines, from which the relaxation time of the pushed holes is determined to be 357 fs±10 fs for an IR push of the highest fluence (118 μJ/cm^2) and 1390 nm wavelength (corresponding to 0.89 eV above-gap excess energy).

The hot-carrier relaxation dynamics is push fluence-independent, as clearly shown in Figure 5.4, and the lower-fluence data in Figure 5.5 is fitted with this decay model, fixing the relaxation time to that achieved for the highest fluence transient. The lack of fluence-dependence of hot-carrier relaxation dynamics suggests that, unlike in previous studies, [121] thermalization processes are not dominated by scattering occurring within the freshly generated non-equilibrium hot-carrier distribution. Importantly, such push-fluence independent relaxation times also prove an absence of hot-phonon bottleneck effects, most likely because we employed much lower IR-push fluences here than used in previous investigations of lead-halide perovskites [170]. The energy loss of holes pushed into non-equilibrium is therefore most likely dominated by scattering with the large, thermalized population of holes near the top of the valence band. Any potential contributions from phonon-assisted processes to this thermalization are either negligible or unimpeded by the build-up of a hot-phonon distribution due to relatively low densities of hot carriers, below the hot-phonon bottleneck threshold. Moreover, the dependence of the push-induced signal on the wavelength of the push (discussed further below) suggests that the hot-carrier energy loss predominantly derives from scattering with other charge-carriers, rather than phonons, given that the latter would result in a slowing of the cooling dynamics with higher excess energy of the hot carriers, while the opposite is actually observed. [93, 121] Notably, the energy loss time reported here is slower than thermalization times for lead halide perovskites under high photoexcitation densities, [121] but orders of magnitude faster than the cooling of a hot charge-carrier gas reported for tin triiodide perovskites following non-resonant excitation [110–112]. Therefore, a realistic assessment of the usefulness of such materials in hot-carrier extracting solar cells needs to be performed in terms of the timescales required for interaction of charge-carriers with an already present background density of cooled charge-carriers encountered in a tin-halide perovskite solar cell owing to background hole doping that arises from tin vacancy formation.

5.3.3 Push Energy Dependence

To further elucidate the mechanisms by which non-equilibrium charge carriers relax in the presence of a cooled, already thermalized charge-carrier gas, the dependence of relaxation dynamics on the excess energy provided by the IR push pulse was investigated. For this purpose, the transient push-induced photoconductivity in highly doped $FA_{0.83}Cs_{0.17}SnI_3$ thin film (no tin fluoride added) was measured, while the infrared push pulse wavelength was varied using an optical parametric amplifier. Time-dependent photoconductivity transients of these push-probe experiments (analogous to traces shown in Figure 5.5) are shown in Figure 5.6A for selected push wavelengths between 1400 nm and 2000 nm. The full set of decay traces for wavelengths spanning 1200 nm to 2000 nm is shown in Figure A.2 in the Appendix A. For longer excitation wavelengths (lower excess energy), pushed holes relax more slowly towards the top of the valence band compared to the case of excitation with shorter wavelengths (higher excess energy). Figure 5.6B illustrates the dependence of the relaxation time on the push wavelength, obtained by fitting a convolution of a monoexponential decay with Gaussian broadening to the photoconductivity traces shown here and in Figure A.2 in the Appendix A. These fits demonstrate that the lifetime of the hot carriers indeed increases with increased push wavelength (i.e. the relaxation rate increases with increasing excess energy above the band edge, as shown in the inset). This finding is qualitatively consistent with the early thermalization dynamics reported by Richter et al.[121] for non-equilibrium carriers in lead halide perovskites, who found that higher excess energy increased the average velocity or charge carriers and therefore the carrier-carrier scattering rates. In the case presented in this chapter, this higher excess energy imparted upon pushed charge carrier will therefore lead to faster energy exchange between hot carriers and already thermalized holes at the band edge.

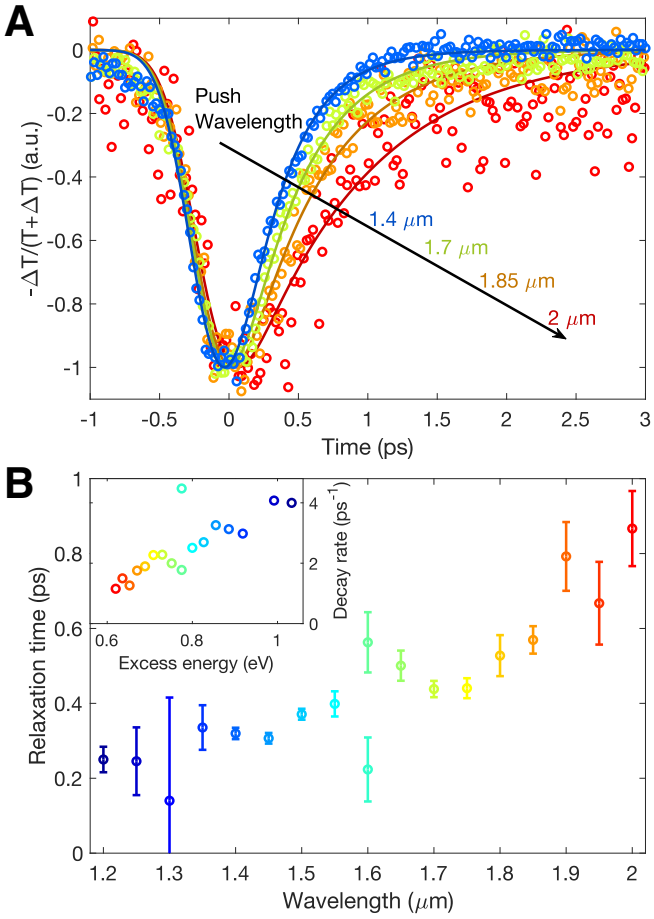


Figure 5.6: Wavelength dependence of push-induced photoconductivity in $FA_{0.83}Cs_{0.17}SnI_3$ thin film with high hole doping. A Push-induced conductivity transients for a highly doped (no SnF_2 additive) $FA_{0.83}Cs_{0.17}SnI_3$ thin film, resulting from sub-bandgap IR push pulses of different wavelengths, indicated by the colour-coded labels. The data (empty hoops) were scaled to -1 at the peak of the negative response and offset temporarily to time=0. The darker solid lines represent fits of a monoexponential decay function convoluted with a Gaussian instrument response, used to determine the decay time associated with re-thermalization and the strength of the signal. **B** Dependence of charge-carrier relaxation times on push wavelength extracted from fits shown in A and in Figure A.2 in the Appendix A. The error bars represent the 95% confidence intervals of the lifetimes, obtained as the optimal fit parameters. The inset shows the equivalent data, presented instead as charge-carrier scattering rate plotted against photon energy of the push pulse, representing the excess energy imparted on carriers upon the push.

The converse effect would be expected to occur if the energy loss of hot carriers were to be dominated by hot-carrier–phonon scattering, which results in slower cooling dynamics being observed for higher excess energies in lead-halide perovskites [93]. It is therefore concluded that for relatively low hot-carrier densities (below the hot-phonon bottleneck

threshold), generated in the presence of a large thermalized gas of already cooled charge carriers, a dominant route for dissipation of the excess energy is through scattering of hot charge carriers with the background of cold charge carriers that are already thermalized to the lattice temperature, causing a negligible rise of the carrier gas temperature.

5.3.4 Spectral Analysis of Conductivity

Finally, the origin of the negative THz photoconductivity after sub-bandgap excitation was investigated by examining its frequency dependence across the THz spectral range. A decreased conductivity of a thin film could originate from a decreased density of free charge carriers or a decreased mobility of the existing carriers. Since the THz probe techniques rely on the interaction of the probe photons in the THz frequency range, spectral changes to that interaction (e.g. the emergence of resonant species, or a change of charge-carrier scattering time) also have to be investigated. Finally, as the THz conductivity is inversely related to the transmission of THz radiation, any mechanisms that enhance the THz radiation (e.g. stimulated THz emission) also must be considered. To disentangle such effects and determine the mechanism for the observed apparent reduction in THz conductivity upon the arrival of the IR push pulse, an analysis of changes in the spectral domain of the THz photoconductivity was performed. A further, more detailed discussion of this topic is available in Appendix A. Figure 5.7A shows that the real (solid circles) and imaginary (empty hoops) parts of the THz photoconductivity spectrum of the highly hole-doped $FA_{0.83}Cs_{0.17}SnI_3$ thin film vary with frequency. The spectral shape of the complex push-induced conductivity change $\Delta\sigma$ can be described by a negative Lorentz resonance function, given by

$$\Delta\sigma \propto \frac{i\omega}{\omega^2 - \omega_0^2 + i\omega\Gamma}\,, \tag{5.1}$$

with the resonant frequency of $f_0{=}\omega_0/2\pi = 1.59\,\mathrm{THz}$ and broadening parameter $\Gamma/2\pi = 3.69\,\mathrm{THz}$, as shown in solid black lines in the Figure 5.7A. A similar negative THz

photoconductivity with Lorentzian spectral lineshape has been previously associated with stimulated THz emission occurring during photoexcited charge-carrier relaxation in graphene [175]. Such stimulated THz emission causes an apparent increase of THz transmission which is interpreted as a reduction of conductivity, therefore providing a reasonable explanation for the observations presented in this chapter. It is therefore concluded that the negative THz conductivity observed here results from the excitation of free electrons (holes) to energetically higher (lower) states within the conduction (valence) band, following which they interact with the THz probe, releasing stimulated THz emission upon their return to the edge of the band. Such stimulated emission processes do not by themselves influence the charge-carrier dynamics provided the probe is sufficiently weak (which has been ascertained), similar to the case of the commonly used transient absorption spectroscopy technique based on IR probe pulses [170]. It is worth noting that although negative THz photoconductivity with similar spectral features can be in principle replicated within the Drude model in association with an increasing effective mass high in a non-harmonic band [155], this explanation is quantitatively incompatible with the very short charge-carrier scattering rates present in perovskite semiconductors, as explained in Appendix A. Other interpretations of negative photoconductivity present in the literature are specific to low-dimensional materials and rely on e.g. a linear dispersion relation of photoexcited charge carriers in graphene near the Dirac point [176–178], which does not apply in this case. It is therefore concluded that the change of photoconductivity observed upon push-pulse arrival is neither related to a change in the free-carrier density (previously proposed to result from hot-carrier trapping [172]), nor to changes in the mobility of charge carriers [155]. These mechanisms would cause a significant change in the DC (0 THz) conductivity that is absent in the data shown in Figure 5.7. Instead, the interaction of hot carriers with the THz pulse results in stimulated emission of THz photons, increasing the apparent transmission of

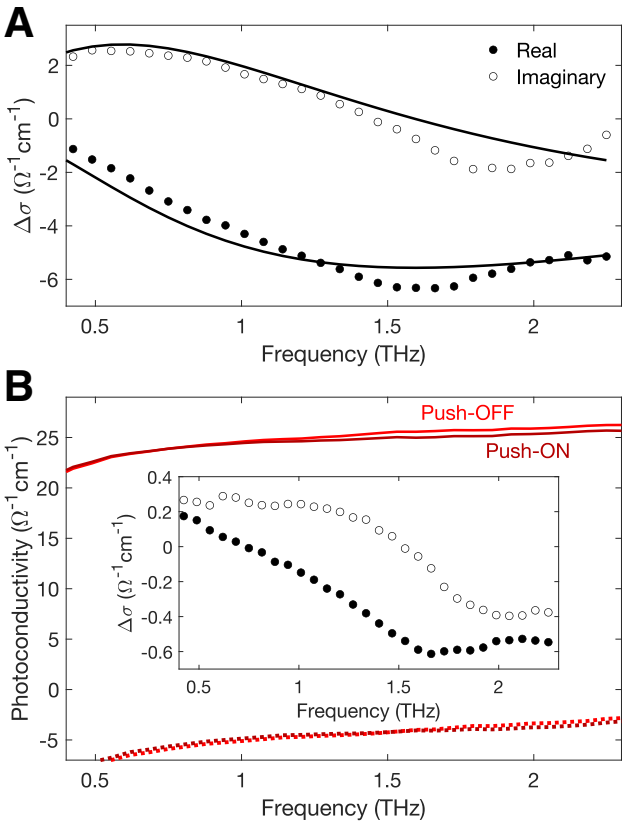


Figure 5.7: Complex THz photoconductivity spectra for $FA_{0.83}Cs_{0.17}SnI_3$ thin films. **A** Complex push-induced THz conductivity spectrum for highly doped (no SnF_2 additive) $FA_{0.83}Cs_{0.17}SnI_3$ generated through an IR push pulse only, using a push fluence of 142 $\mu J/cm^2$. The real part of the push-induced conductivity spectrum is shown by filled circles and the imaginary part by empty hoops. The solid lines represent a negative Lorentzian lineshape fit to the measured photoconductivity, which yields a resonant frequency of f_0= 1.59 THz and spectral broadening of $\Gamma/2\pi$ = 3.69 THz, as defined in Equation 5.1. The push-induced conductivity spectrum was measured about 0.1 ps after push pulse arrival. **B** Changes in the pump-induced THz photoconductivity spectra, resulting from the presence of an IR push pulse, for electrically undoped (20% SnF_2) $FA_{0.83}Cs_{0.17}SnI_3$ photoexcited with a ~40$\mu J/cm^2$ pump pulse at 800 nm wavelength. The real part of the photoconductivity is shown by the solid line and the imaginary part by the dotted line. The push-induced difference in the pump- induced photoconductivity, $\Delta\sigma$, is shown in the inset, and calculated from the difference between the Push-ON spectrum (dark red) and Push-OFF spectrum (light red). Filled black circles represent the real part of the push-induced photoconductivity change and empty hoops show its imaginary part. The conductivity transients shown in Figures 5.2B and 5.5 represent spectral averages of THz conductivity over the probe's bandwidth, as explained in Chapter 4.

the probe and leading to a reduction of the apparent THz conductivity, as calculated directly from the transmission intensity of the probe.

In order to verify whether the same mechanism of THz stimulated emission is responsible for the photoconductivity reduction observed in the PPP transients shown in

Figure 5.2B, the photoconductivity spectrum of $FA_{0.83}Cs_{0.17}SnI_3$ with low level of hole doping (20% SnF_2 added during film fabrication) was measured. To allow determination of just the push-induced spectral component, the complex photoconductivity spectrum was measured shortly after the push arrival with the IR push beam either incident on the sample ("Push-ON" shown in dark red in Figure 5.7B) or blocked ("Push-OFF" shown in light red). The resulting THz spectra with and without the push present both have features expected from a Drude conductivity model with charge-carrier scattering rate much faster than the frequency of the probing radiation, that is, they exhibit a spectrally flat and positive real part (solid lines) and comparably small imaginary contribution (dotted lines) [49]. This behaviour has previously been observed for tin triiodide perovskite thin films for which a charge-carrier scattering time can be estimated to be approximately 1.7 fs [75]. To determine the conductivity change induced solely by the arrival of the push, the "Push-OFF" photoconductivity spectrum was subtracted from the "Push-ON" spectrum. This difference, denoted by $\Delta\sigma$, is shown in the inset of Figure 5.7B and demonstrates the same spectral shape as the push-induced photoconductivity of highly doped (no SnF_2) $FA_{0.83}Cs_{0.17}SnI_3$, shown in Figure 5.7A. The similarity of the push-induced spectral changes in THz conductivity between these two experiments (i.e., push-probe for the highly doped film and pump-push-probe for the less doped semiconductor) strongly indicates that a common mechanism is responsible for the decreased conductivity. Therefore, regardless of whether free charge carriers are present through pulsed photo-excitation or whether they are introduced permanently by hole-doping through tin vacancy formation, a push-pulse of sub-bandgap photon energy creates a population of hot charge carriers in thermal non-equilibrium that returns to the band edge accompanied by stimulated THz emission.

5.4 Conclusion

In conclusion, an ultrafast transient reduction in THz conductivity in photo-excited tin-iodide perovskites was observed upon illumination with an infrared push pulse, exploiting for the first time an Optical-Pump–Infrared-Push–THz-Probe spectroscopic technique. It has been verified that the same negative photoconductivity dynamics occur in heavily hole-doped tin-iodide perovskite, even in the absence of initial photoexcitation across the band gap, which indicates that they are caused by intraband optical transitions of charge carriers. The presence of such intraband, single-photon transitions was confirmed by investigating the dependence of the conductivity reduction amplitude on the initial free charge-carrier density and push-pulse fluence. It was also demonstrated that the spectral shape of the push-induced THz conductivity change is independent of whether the initial free carrier population derives from photoexcitation or chemical doping, confirming a common origin of the transient in intraband transitions of free carriers upon a push. Moreover, the observed Lorentzian lineshape and negative value of the push-induced conductivity change suggest the origin of the signal in stimulated THz emission, which enhances the transmitted THz probe as it interacts with pushed charge carriers. Previous discussions of negative photoconductivity have focused exclusively on low-dimensional materials such as graphene [175–178] and doped nanowires [155]. Therefore, this discovery of negative photoconductivity in a 3D bulk semiconductor such as tin-iodide perovskite will hopefully trigger further discussion about origins of photoinduced conductivity reductions in semiconductors.

Overall, this chapter demonstrated that the Optical-Pump–IR-Push–THz-Probe technique is a facile and powerful approach towards investigating the relaxation of non-equilibrium charge carriers in perovskite semiconductors in the presence of a cold background charge-carrier density, approximating scenarios found under continuous

illumination of sunlight. In this regime, non-equilibrium charge carriers in tin-iodide perovskites relax to the band edges on sub-picosecond timescales. This chapter also reveals that such shorter relaxation dynamics are caused by effective scattering of newly generated non-equilibrium charge carriers with an already present density of cooled, thermalized background charge-carriers, as well as lack of a hot phonon bottleneck effect at the low non-equilibrium carrier densities used in this study. While such thermalized, cooled charge-carriers have rarely been present in studies investigating charge-carrier cooling dynamics after non-resonant photoexcitation, they will dominate under continuous illumination conditions encountered in solar irradiation scenarios, especially in highly doped semiconductors. The propensity of tin iodide perovskites towards self-doping arising from facile tin vacancy formation therefore lowers their prospects as candidate materials for hot-carrier solar cells. Overall, it is proposed that this novel THz pump-push-probe technique may form an important complementary approach to other pump-push-probe and pump-probe schemes (such as infrared probe and transient absorption measurements) [170, 172, 173] used to investigate the relaxation dynamics of non-equilibrium charge carriers. Such approaches will facilitate temporal mapping of the charge-carrier energy exchange and loss dynamics for various background density and excess energy scenarios, which is urgently required for a realistic assessment of the required architecture and the best material contenders for hot-carrier photovoltaic devices.

6

Charge-Carrier Dynamics in Bi-Doped Perovskites

Contents

6.1 Introduction 108
6.2 Results and Discussion 110
6.2.1 Band Structure Changes 110
6.2.2 Energetic Landscape 112
6.2.3 Charge-Carrier Dynamics 114
6.3 Final Remarks and Conclusion 125

The work presented in this chapter has been published in: A. M. Ulatowski, A. D. Wright, B. Wenger, L. R. V. Buizza, S. G. Motti, H. J. Eggimann, K. J. Savill, J. Borchert, H. J. Snaith, M. B. Johnston, L. M. Herz. 'Charge-Carrier Trapping Dynamics in Bismuth-Doped Thin Films of $MAPbBr_3$ Perovskite', *The Journal of Physical Chemistry Letters* , **2020**, *11* (9) 3681-3688 (Ref. [50]). Presented figures were reprinted with permission from [50].

Copyright 2023 American Chemical Society.

6.1 Introduction

The last chapter of this thesis explores the dynamic behaviour of charge carriers generated within $MAPbBr_3$ perovskite thin films chemically doped with bismuth. Although p-type (hole) doping can be observed in tin-halide perovskites due to spontaneous tin-vacancy formation, as described in Chapters 2 and 5, achieving significant n-type (electron) doping in perovskites remains elusive due to the "soft", ionic nature of their crystal lattice. Such behaviour results in migration and phase segregation of ion species, which increases the difficulty of substitutional doping of these materials in the way it is performed in inorganic semiconductors (eg. antimony doping of silicon). Nevertheless, heterovalent doping of perovskite semiconductors has been explored in hope of achieving better performance of photovoltaic devices employing metal-halide perovskites. Heterovalent doping with bismuth has gained particular interest and has been investigated in multiple studies in recent years [57, 66–68, 181–186]. All of the experimental studies followed the same procedure of doping $MAPbBr_3$ single crystals with bismuth ions through the addition of $BiBr_3$ salt to the precursor solution, as described by Abdelhady et al. [57] This method was shown to efficiently incorporate bismuth into the perovskite structure by lead substitution (because of the similarity of ionic radii and electronic structure), as indicated by plasma and flame spectroscopy of Bi-doped single crystals of $MAPbBr_3$ perovskites [57, 68]. Early results indicated positive effects of bismuth additive on the properties of the crystals, such as prolonged stability of inorganic, caesium-based perovskites [182], a rise of electrical conductivity upon bismuth doping of single crystals of $MAPbBr_3$ indicating n-type doping [57, 68], improved visible-light absorption [181], and changes in the absorption spectrum initially identified as bandgap tuning by Abdelhady et al.[57]. However, some investigations have also reported that the addition of bismuth to the perovskite crystal has negative effects on the optoelectronic properties of the semiconductor [67, 183–185].

Subsequent studies of $MAPbBr_3$ crystals revealed an increase of within-gap trap states upon bismuth addition and showed the invalidity of the bandgap tuning effect [66–68, 186]. Such additional traps have also been shown to decrease the performance of the solar cells upon bismuth doping of a mixed-cation, lead mixed-halide perovskite active layer [185]. However, the mechanisms by which bismuth affects the optoelectronic properties of perovskites are still poorly understood, with only a few reports on the topic having been published in recent years [68, 183, 185, 186]. Such an understanding will be critical to the evaluation of the positive and negative trade-offs for chemical doping of metal halide perovskites with heterovalent metals, and will further the general understanding of how different additives may alter the properties of these materials.

In this chapter, the effects of chemical doping of $MAPbBr_3$ perovskite thin films with bismuth are investigated and discussed. A variety of techniques, including photoluminescence (PL) and absorption measurements, as well as time-resolved, ultrafast THz photoconductivity studies, were employed to examine the energetics and dynamics of bismuth-induced charge-carrier trapping in films of different doping levels. An increased density of mid-bandgap, luminescent trap states as well as a rise of energetic disorder were observed upon bismuth doping of $MAPbBr_3$, by examining steady-state absorption and emission spectra of the thin films. The presence of these traps leads to faster recombination of photoexcited charge carriers, as evident from the significant reductions in band-edge photoluminescence and THz photoconductivity lifetimes. A significant decrease of the charge-carrier mobility is reported when bismuth is added to the films, in accordance with the accompanying rise in energetic disorder. Finally, it is deduced that ultrafast trapping of electrons contributes significantly to the worsening of the optoelectronic properties, as indicated by the time-dependent dynamics of the THz photoconductivity. Therefore, the addition of bismuth leads to a significant rise in trap-state density and

energetic disorder that manifests itself in quenched PL, lowered charge-carrier mobility and extended band tails below the absorption onset.

6.2 Results and Discussion

6.2.1 Band Structure Changes

The investigation begins through a careful analysis of the steady-state absorption spectra of thin films of bismuth-doped $MAPbBr_3$. Figure 6.1 displays absorption spectra for a range of bismuth dopant percentages corresponding to the concentration of bismuth salt in the precursor solution, as outlined in Appendix B. The observed changes in the absorption spectra of Bi-doped $MAPbBr_3$ films include an apparent redshift of the absorption onset, together with a decreased height of the excitonic peak with increased bismuth content. In order to examine the origin of these changes it is worth noting that the absorption spectrum of a semiconductor has both excitonic and free electron-hole contributions, both of which are broadened due to energetic disorder, electron-phonon interactions and natural broadening [114, 117, 187, 188]. While both bound excitonic and free species contribute to the continuum absorption above the band edge, the pronounced peak below the band gap is mostly caused by the absorption from the bound excitonic states alone.

Understanding why bismuth doping causes the observed decrease of the sub-gap excitonic peak intensity requires a detailed examination of the absorption onset according to the theory by Elliott [117]. In general, such changes could originate either from a reduction in the strength of bound excitonic transitions because of a decrease in the exciton binding energy, or from an increased broadening of the spectrum, which reduces the maximum intensity of the exciton peak through spectral spreading of the excitonic oscillator strength [189]. While a reduction in excitonic binding energy will lead to an apparent blueshift of the absorption offset, spectral broadening will conversely cause the presence of extended sub-gap tails resulting from increased energetic disorder. It

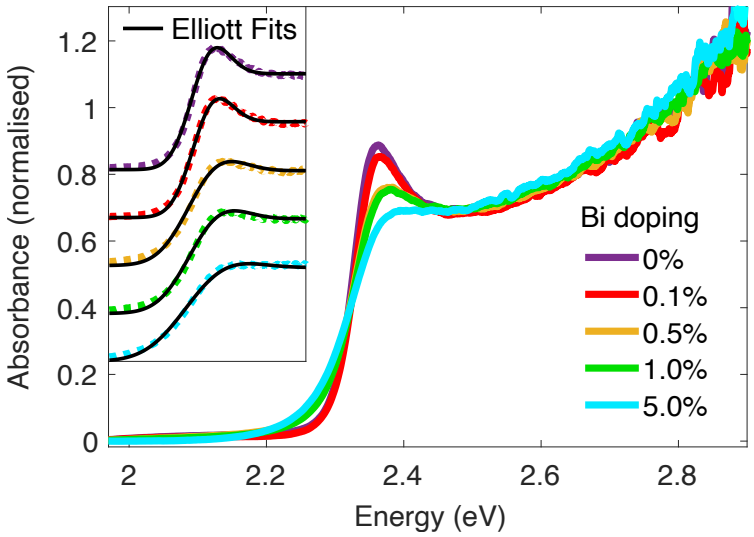


Figure 6.1: The absorbance (negative base-10 logarithm of transmittance) of $MAPbBr_3$ thin films with different bismuth doping levels. The inset shows Elliott fits plotted in black on top of the experimental data for the energy range 2.2 eV-2.5 eV, offset vertically for each sample for better visibility. The parameters obtained from the fits are shown in Table 6.1. Full details of the fitting procedure can be found in Chapter 3.

is therefore apparent from Figure 6.1 that the latter applies, but to confirm this and dispel the previous notion of a doping-induced band shift [57], a full modelling of the absorption onset was carried out with Elliott theory to distinguish clearly between such effects [189]. Elliott fitting was performed by Dr Adam D. Wright (Semiconductors Group, Department of Physics, University of Oxford). This Elliott analysis has been previously applied to undoped metal halide perovskites [114, 189] in order to reveal information about the bandgap of the semiconductor E_g and the exciton binding energy E_b, as well as the broadening of the absorption spectrum (characterised by Γ as explained in Chapter 3) associated with energetic disorder.

The inset to Figure 6.1 displays as solid lines fits to the absorption onset of bismuth-doped $MAPbBr_3$ films, based on the theory by Elliott [117] and outlined in Chapter 3. The extracted fitting parameters are listed in Table 6.1 and reveal a significant increase in the broadening (Γ) of the absorption spectrum with increasing bismuth doping.

Bi doping	E_b (meV)	E_g (eV)	Γ (meV)
0%	34.8	2.38	30.1
0.1%	33.3	2.38	30.7
0.5%	33.3	2.38	42.7
1.0%	32.6	2.38	43.7
5.0%	33.5	2.38	55.1

Table 6.1: Fitting parameters obtained from Elliott fits to the absorption onset spectra of Bi-doped $MAPbBr_3$ films shown in the inset of Figure 6.1. The bandgap energy E_g was optimised globally for all samples, with exciton binding energy E_b and broadening parameter Γ left as free parameters for each doping concentration.

Importantly, the exciton binding energy is essentially unchanged across the range of Bi concentrations investigated, and the spectra are well described by a single value of bandgap energy E_g, here globally optimised for all samples. Although the initial report by Abdelhady et al. concluded that bandgap narrowing occurs upon bismuth doping [57], the results presented in this chapter clearly indicate that the effect of bismuth is in fact limited to a broadening of the absorption onset due to energetic disorder, in agreement with previous reports investigating single crystal absorption via sensitive ellipsometry measurements [67]. These detailed Elliott fits further prove that intrinsic parameters such as exciton binding energy and band gap energy are unaffected by Bi-doping of $MAPbBr_3$, making the observed changes an entirely extrinsic effect.

6.2.2 Energetic Landscape

To further investigate whether the increase in energetic broadening with bismuth doping may be correlated with the introduction of additional defect states, the steady-state photoluminescence spectra were recorded from photoexcited films. Figure 6.2 reveals that for $MAPbBr_3$ thin films measured in vacuum, bismuth doping leads to a quenching of the band-edge PL emission, a small blueshift of this emission peak (shifting by about 10 nm across the sample set), as well as a significant enhancement of an infrared (IR) emission band associated with radiative recombination of charge carriers from states within the band gap. The observation of the band-edge PL blueshift reinforces the

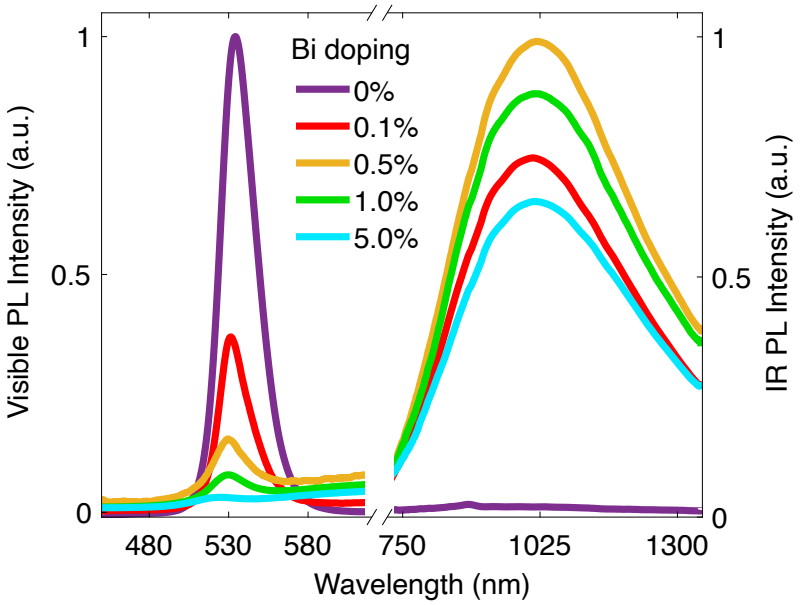


Figure 6.2: PL spectra of Bi-doped $MAPbBr_3$ thin films photoexcited at 400 nm, measured in vacuum. The band-edge emission can be seen at 530 nm and the sub-bandgap emission band from trap states at around 1000 nm. Significant quenching of the band-edge PL with bismuth doping can be observed, together with an overall enhancement of IR emission in the doped films. The relative intensities of the IR to visible peaks are arbitrary.

conclusion that no bandgap narrowing occurs upon bismuth doping of the perovskite crystal. The observed blueshift is instead most likely associated with lowered photon reabsorption in the doped films [186, 190], given that bismuth doping induces faster charge-carrier trapping (see below), and therefore carriers generated initially nearer the front surface have insufficient time to diffuse deeper into the bulk of the thin film.

To examine the origin of the observed below-gap infrared PL emission band, it is essential to note that PL spectra measured in air and shown in Figure 6.3 clearly reveal this band to be present for both the bismuth doped films as well as the undoped material, although its intensity is considerably stronger in the former. This observation suggests that the trapping mechanism is not exclusively caused by the chemical bismuth doping, but rather originates from traps that can generally be present in $MAPbBr_3$ and are strongly enhanced through the bismuth-doping process. Motti et al. [43] previously investigated such broadband IR emission from $MAPbBr_3$ perovskites in the absence of

bismuth doping and found it to be associated with the recombination of charge carriers trapped by native point defects in the crystal structure. Their work identified electron-trapping defects originating from lead vacancies and halide interstitials as the cause of the IR emission, based on density functional theory (DFT) calculations and analysis of the dynamics of charge-carrier trapping in $MAPbBr_3$ films interfaced with either hole- or electron-extraction layers. Since for the case of Bi-doped $MAPbBr_3$ films under investigation here, the intensity of such IR emission is enhanced following bismuth doping, it is proposed in this chapter that the preparation pathway of these bismuth-doped materials leads to enhanced electron traps of a similar origin, although a new defect band directly attributable to bismuth cannot be entirely excluded as a cause [184].

As a final comment, the spectra in Figure 6.3 (measured in air) differ from the ones presented in Figure 6.2 (measured in vacuum). The main difference relates to the intensity of the emission from the undoped $MAPbBr_3$ sample, which is much stronger for the measurement in air. This effect was also investigated previously by Motti et al. [43, 45] and originates from trap passivation by molecular oxygen in the air, which reduces trap-mediated recombination pathways in the undoped films, allowing stronger band-edge emission as well as IR emission from the electron trapping defects. The presence of oxygen does not have a strong effect on the emission from doped samples, which could indicate that the electron trapping mechanism, proposed in this chapter to be the main source of trap-mediated recombination in Bi-doped $MAPbBr_3$ thin films, is not influenced by the presence of oxygen.

6.2.3 Charge-Carrier Dynamics

The observed energetic disorder and enhanced trap-state emission upon bismuth doping of $MAPbBr_3$ perovskites may be linked with the short lifetimes of photoluminescence observed for bismuth-doped $MAPbBr_3$ [68, 183, 186]. To investigate such correlations,

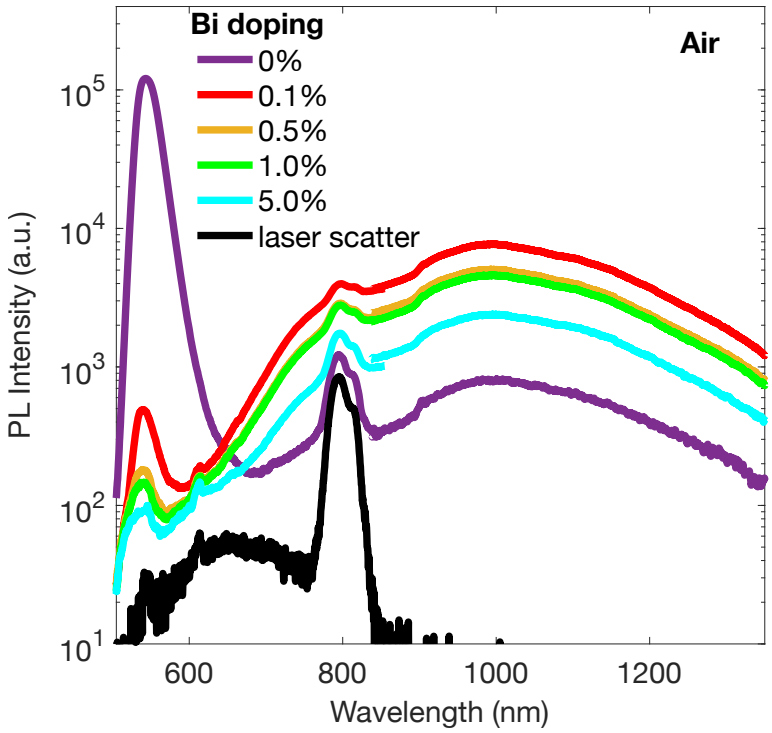


Figure 6.3: PL spectra of Bi-doped $MAPbBr_3$ thin films measured in air, shown on a logarithmic scale. The IR part of the spectrum, measured with InGaAs detector, was scaled to match the measurements of the Si CCD for the overlap region (800 nm-1000 nm). The films were excited at 470 nm with continuous wave diode laser. The feature visible at 800 nm originated from scattered light from a Ti-Sapphire laser operating in the background at the time of the measurement and does not originate from the samples. The spectrum plotted in black was measured with the 470 nm excitation laser turned off, showing the Ti-Sapphire scatter and a weak remaining background signal (at 700 nm) caused by room lights.

the charge-carrier dynamics in these bismuth-doped perovskite films was investigated as the next step of this study. The temporal behaviour of the photoluminescence was examined using the time-correlated single photon counting (TCSPC) technique (described in Chapter 3). The decay of the band-edge photoluminescence displayed in Figure 6.4 shows a shortening of the PL lifetimes in the bismuth-doped films compared to the pristine perovskite, to time scales that are limited by the response of the detector (shown in Figure 6.5). Therefore, the lack of variation of PL lifetimes between films with different doping levels likely originates from the limited time resolution of the measurement. In the inset of Figure 6.4, the dynamics of the band-edge emission is contrasted with those observed

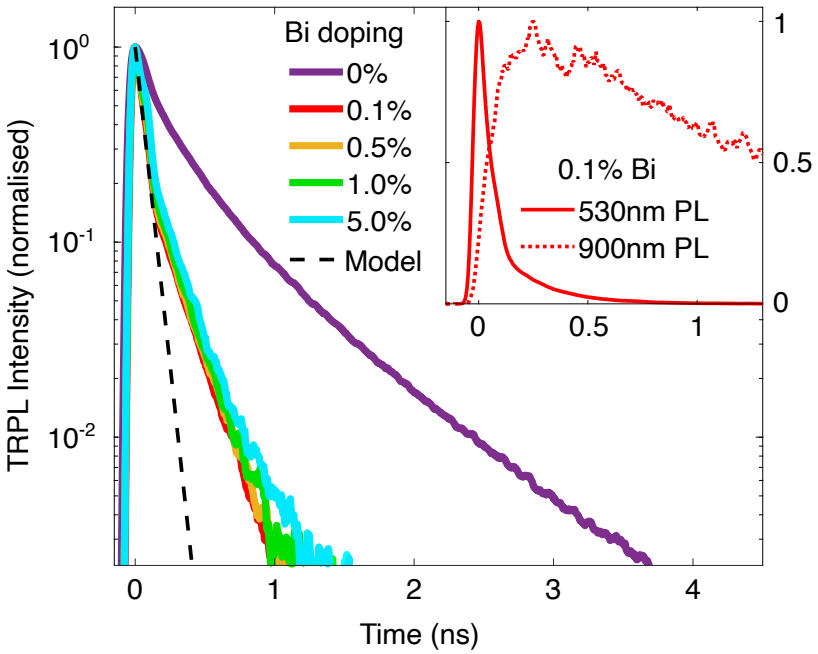


Figure 6.4: Time-resolved photoluminescence (TRPL) of bismuth-doped $MAPbBr_3$ thin films measured in vacuum with time-correlated single photon counting (TCSPC) setup, following a photoexcitation at 400 nm at a fluence of 40 nJ/cm^2. The decay traces are limited by the instrument response function of the detector, shown in Figure 6.5. The dotted black line represents the modelled PL decay as discussed in the main text. The inset shows a comparison of TRPL measured at 530 nm (band-edge) and 900 nm (sub-bandgap) for $MAPbBr_3$ doped with 0.1% Bi, shown on a linear vertical scale for clarity.

for the below-gap, broad IR emission band, for the 0.1% bismuth-doped $MAPbBr_3$ film. Similar to previous observations for $MAPbBr_3$ perovskite in the absence of bismuth doping [43], the IR emission transient exhibits a slowly rising onset and a relatively long lifetime. The slow rise matches the timescale of the decay of the band-edge emission, suggesting that the population of charge carriers emitting in the IR is fed by trapping of free charge carriers emitting just below the band edge. It is also evident that this electron trapping mechanism makes a significant contribution to the overall decay of the photoexcited charge-carrier population. Overall, these transients support the hypothesis that the enhanced IR emission in the doped films is caused by the selective trapping of electrons and their subsequent radiative recombination with free holes.

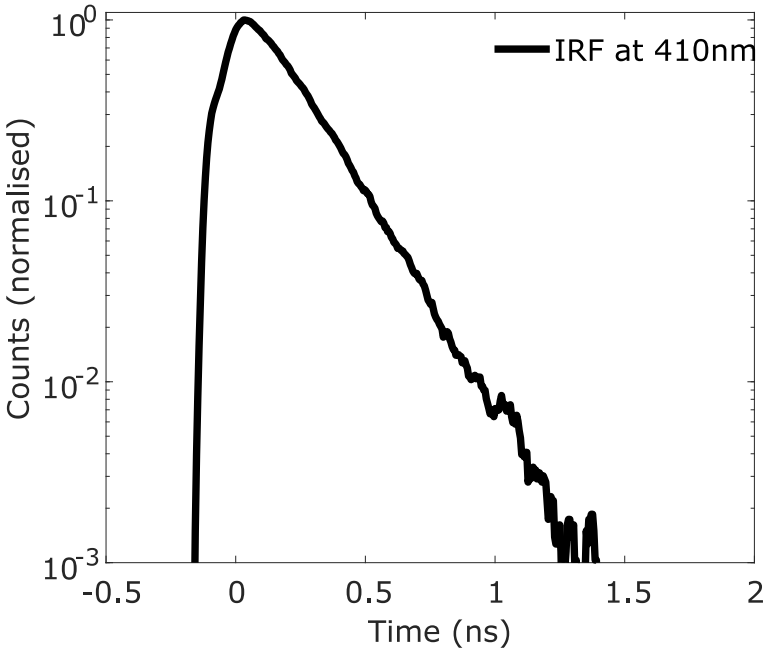


Figure 6.5: Instrument response function (IRF) of the TCSPC setup (for detection of 410 nm pulses) used to measure the time-resolved PL shown in Figure 6.4. The IRF was measured by directing scattered light from the ultrafast laser used for photoexcitation onto the SPAD detector and recording the photon arrival histogram, which resulted in much slower decay (picoseconds FWHM) than expected for the laser pulse (80 fs FWHM). Note: The IRF of the TCSPC setup was measured and provided by Kimberley J. Savill and Hannah J. Eggimann (Semiconductors Group, Department of Physics, University of Oxford).

As the next step, the dynamics of the photoexcited charge carriers was examined with higher temporal resolution, employing the Optical-Pump THz-Probe (OPTP) technique, outlined previously by Wehrenfennig et al. [30] and described in detail in Chapter 3. This approach allows the recording of the time-resolved THz photoconductivity following excitation with short (35 fs) laser pulses for a range of fluences, as shown in Figure 6.6 for $MAPbBr_3$ films with bismuth doping levels of 0%, 0.1% and 5%. Since the measured photoconductivity of the sample is proportional to the charge-carrier density, OPTP is a direct, non-contact probe of the photoexcited charge-carrier population in the perovskite thin films.

As previously described by Herz [87], and discussed in Chapter 3, in hybrid perovskites, the room-temperature decay dynamics of a charge-carrier population (n_{cc}) after

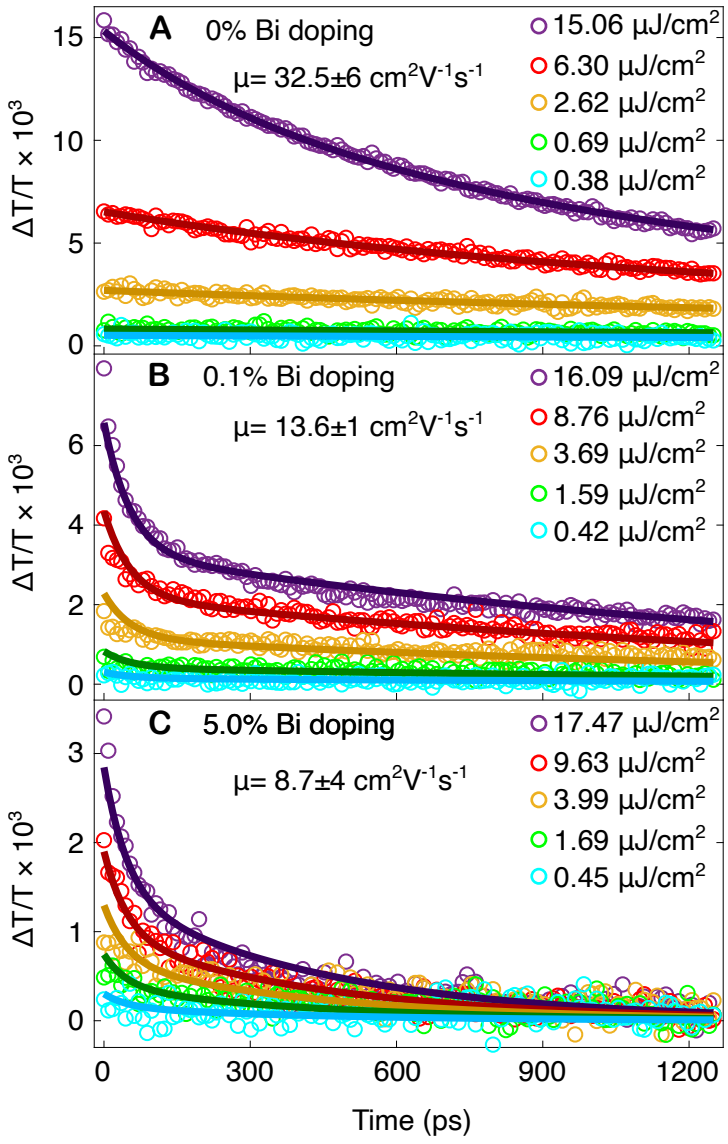


Figure 6.6: THz photoconductivity decays obtained from OPTP measurements in vacuum for Bi-doped $MAPbBr_3$ thin films. The data (hoops) for the (A) undoped (0% Bi doping) sample were globally fitted with a solution to Equation 6.3 (given by Equation 6.4). Equation 6.10 (a bi-exponential decay) was used for the doped samples containing 0.1% (B) and 5% (C) bismuth doping. The fits are shown as solid lines. The indicated effective charge-carrier mobilities (μ) are extracted from the time = 0 onset of the photocoductivity and represent the sum of effective electron and hole mobilities. The indicated uncertainty is calculated from the standard deviation of the values recorded for different pump fluences. The normalised decay traces for all samples are shown in Figure 6.7 and the fits can be found in Appendix B.

photoexcitation mostly depend on the contribution from three recombination pathways: monomolecular (trap-assisted) recombination with rate k_1, bimolecular (band-to-band) electron-hole recombination (with rate $k_2 n_{cc}$), and many-body (Auger) recombination ($k_3 n_{cc}^2$). However, as Auger recombination is a higher-order process, its contribution can often be neglected for hybrid perovskites when relatively low charge-carrier densities of $n_{cc} < 10^{20}\text{cm}^{-3}$ are employed (since for these densities, the rate $k_3 n_{cc}^2 << k_2 n_{cc}$ for typical values of k_2 and k_3 measured for lead-halide perovskites) [74, 75, 191]. This condition is satisfied for the excitation fluences used in this study (since the highest used fluence of $17.5\,\mu\text{J/cm}^2$ corresponds to a photoexcited charge-carrier density of $\sim 10^{18}\,\text{cm}^{-3}$) and therefore the Auger recombination was neglected in the analysis of the charge-carrier dynamics below.

Given that the previous considerations in this chapter suggest the occurrence of selective fast trapping of electrons in bismuth-doped $MAPbBr_3$ films, the model of the observed recombination dynamics needs to account for different rates of trap-mediated decays for photoexcited electrons and holes. In this case, the population densities of electrons (n) and holes (p) can be described by the coupled differential equations:

$$\frac{\partial n}{\partial t} = -k_1^{\text{e}} n - k_2 np \tag{6.1}$$

$$\frac{\partial p}{\partial t} = -k_1^{\text{h}} p - k_2 np \tag{6.2}$$

where k_1^{e} and k_1^{h} are the trap-assisted recombination rates for electrons and holes, respectively, and k_2 is the bimolecular recombination rate constant. However, these equations can be simplified further for the two cases of undoped, and bismuth-doped $MAPbBr_3$, given that clear changes occur in the shape of the transients (see Figure 6.6) and their fluence dependence (as can be clearly seen in Figure 6.7) upon bismuth doping.

First, for the case of the undoped (0% Bi) $MAPbBr_3$ film the charge-carrier dynamics exhibit large fluence dependence, as seen in Figure 6.7 where the decay traces have been

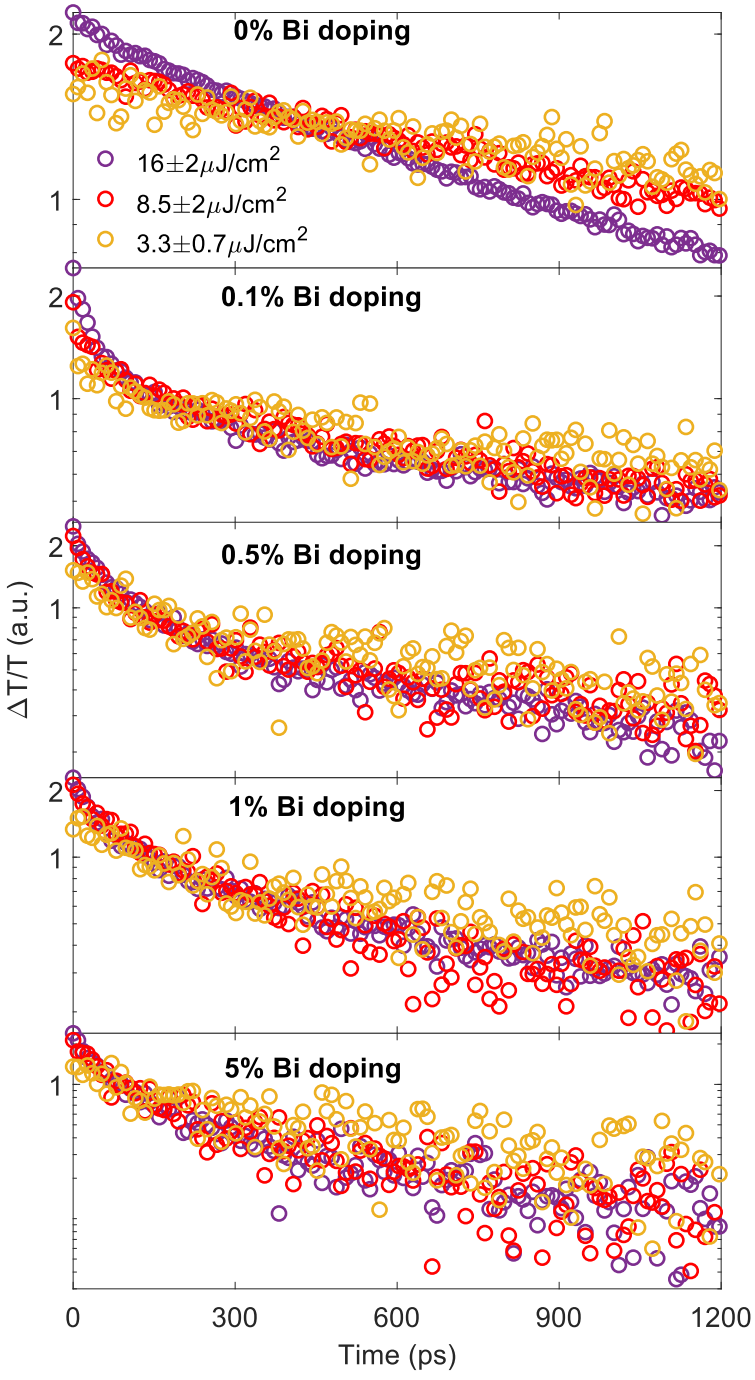


Figure 6.7: Photoconductivity decays in bismuth-doped $MAPbBr_3$ thin-films, shown on a logarithmic scale. The data were scaled using fits presented in Figure 6.6, in order to avoid uncertainty caused by scaling the data to the first datapoint. The lowest measured pump fluence data were removed for clarity, as the relative noise for these decays was the largest. The excitation fluences are indicated by the legend.

normalised, suggesting a significant contribution of bimolecular electron-hole recombination to the overall decay dynamics. Furthermore, at low pump fluences, the transients exhibit a monoexponential decay, indicating that the electron and hole monomolecular recombination constants can be approximated to be identical, $k_1^e = k_1^h = k_1$, resulting in Equations 6.1 and 6.2 being reduced to a single equation:

$$\frac{dn_{cc}}{dt} = -k_1 n_{cc} - k_2 n_{cc}^2 \tag{6.3}$$

where $n_{cc} = n = p$ is the charge-carrier population density of either electrons or holes. The solution to this differential equation turns out to be an analytical expression of the form:

$$n_{cc}(t) = \frac{k_1}{(k_2 + \frac{k_1}{n_0}) \exp(k_1 t) - k_2} \tag{6.4}$$

where n_0 is the initial number density of photoexcited electron-hole pairs at $t = 0$. Figure 6.6 shows that fits to the photoconductivity ($\propto n_{cc}$) transients of the undoped (0% Bi) $MAPbBr_3$ film (solid lines) based on Equation 6.4, assuming global values of k_1 and k_2 across all fluences, provide an excellent match with the experimental data, confirming the assumptions of balanced electron and hole recombination rates.

Second, for the case of bismuth-doped $MAPbBr_3$ films, the charge-carrier dynamics exhibit very little dependence on excitation fluence as proven by almost identical normalised traces in Figure 6.7, which indicates that trap-mediated (monomolecular) recombination now dominates over bimolecular recombination pathways, in agreement with the observed severe suppression of the PL intensity for doped films (see Figures 6.2 and 6.3). In this case, the bimolecular recombination pathway can be neglected, simplifying Equations 6.1 and 6.2 to:

$$\frac{dn}{dt} = -k_1^{\mathrm{e}} n \tag{6.5}$$

$$\frac{dp}{dt} = -k_1^{\mathrm{h}} p \tag{6.6}$$

Equations 6.5 and 6.6 have simple monoexponential solutions for the charge-carrier populations, given by:

$$n = n_0 \exp(-k_1^{\mathrm{e}} t) \tag{6.7}$$

$$p = n_0 \exp(-k_1^{\mathrm{h}} t) \tag{6.8}$$

where n_0 is the initial number of electron-hole pairs straight after photoexcitation. Within the simple Drude model, the electron-hole sum photoconductivity σ determined in the OPTP measurements [30] is equal to the sum of the individual products of electron and hole population densities and their respective mobilities:

$$\sigma(t) = \mu_{\mathrm{e}} n(t) e + \mu_{\mathrm{h}} p(t) e \tag{6.9}$$

where μ_{e} and μ_{h} are the mobilities of electrons and holes respectively, assumed to be unchanged over the timescales of the measurements. Equations 6.7, 6.8 and 6.9 thus imply a bi-exponential decay of the THz photoconductivity in the case of bismuth-doped $MAPbBr_3$ thin films:

$$\sigma(t) = n_0 e[\mu_{\mathrm{e}} \exp\left(-k_1^{\mathrm{e}} t\right) + \mu_{\mathrm{h}} \exp\left(-k_1^{\mathrm{h}} t\right)] \tag{6.10}$$

As Figure 6.7 illustrates, the photoconductivity in bismuth-doped films indeed deviates from a simple monoexponential behaviour, even at low pump fluences, showing that doping leads to imbalanced electron and hole decay dynamics, through an enhancement of selective, ultrafast electron trapping. This selective trapping, together with slow recombination dynamics with free holes manifests itself in bi-exponential photoconductivity decays. It is important to note, however, that the shape of the photoconductivity transients significantly differs from that observed for time-resolved band-edge PL decays. This difference originates from the fact that while the photoconductivity measurement is sensitive to the sum of the contributions of electron and hole populations (whose

different decay rates result in bi-exponential photoconductivity decay), the band-edge PL originates from the radiative recombination of free electrons with holes. Therefore, the PL intensity I_{PL} is proportional to the product of electron and hole populations, which, even for imbalanced trapping, results in monoexponential PL intensity transients with rate equal to the sum of the individual decay rates of electrons and holes ($k_1^{\mathrm{e}} + k_1^{\mathrm{h}}$):

$$I_{\mathrm{PL}}(t) \propto k_2 n(t) p(t) = k_2 \exp\left(-[k_1^{\mathrm{e}} + k_1^{\mathrm{h}}]t\right). \tag{6.11}$$

To probe the validity of the fast, selective trapping model for bismuth-doped $MAPbBr_3$ thin films, the OPTP photoconductivity transients were fitted with Eqn. 6.10 in order to obtain the decay constants k_1^{e} and k_1^{h}, which were then verified to also accurately reflect the PL dynamics according to Eqn. 6.11. Figure 6.6 B and C shows excellent agreement between the selective trapping model and the photoconductivity data, which reflects the strongly bi-exponential decay of the photoconductivity according to Equation 6.10. Values for the extracted decay constants k_1^{e} and k_1^{h} have been plotted against the percentage of bismuth doping in Figure 6.8. The faster decay component was assigned to the rapid trapping of electrons (k_1^{e}), based on existing literature investigating the nature of native defects in undoped $MAPbBr_3$ thin films [43]. It was then ascertained that these extracted monomolecular rate constants are consistent with the time-resolved photoluminescence transients shown in Figure 6.4. For this purpose, the dotted black line in Figure 6.4 represents the expected decay of the PL signal for the doped films, as calculated from Equation 6.11 using the monomolecular constants extracted from OPTP data. This predicted PL decay generally reflects the data well but is slightly faster because the TCSPC measurements are limited by the instrument response of the detector (sub-nanosecond, as shown in Figure 6.5). The observations of the temporal behaviour of the photoconductivity and the photoluminescence in doped and undoped $MAPbBr_3$ thin films thus support the notion that bismuth doping enhances selective trapping of one

charge-carrier species following photoexcitation. Such fast electron trapping leads to an initial rapid decrease of the photoconductivity ($\propto [\mu_e n + \mu_h p]$), which subsequently decays slowly due to hole trapping as well as recombination of trapped electrons with free holes. These effects together lead, however, to a rapid quenching of PL intensity ($\propto k_2 pn$).

The OPTP photoconductivity measurements not only enabled the investigation of the dynamics of charge-carrier populations but also their mobilities, since the photoconductivity of the thin film depends on the product of these two quantities. By estimating the initial density of charge-carrier pairs n_0, the sum of the electron and hole mobilities were obtained from the onset of the photoconductivity at time $t = 0$, according to Equation 6.10. Here, the initial density n_0 is determined from the absorption of the films at the excitation wavelength, under the assumption that each absorbed photon photoexcites one electron-hole pair [30]. Figure 6.8 displays the extracted values of the electron-hole sum mobilities. A significant decrease of charge-carrier mobility is observed with bismuth doping, which is attributed to an increased presence of charged defects in the doped films that enhance the scattering rate of charge carriers. This reduction of charge-carrier mobility correlates with the observed broadening of the absorption spectra discussed earlier (see Figure 6.8 A&B), which is expected, given that the presence of charged defects will also lead to additional energetic disorder in the bismuth-doped perovskite films.

In addition, it is found that the photoconductivity transients of the doped perovskite films presented in this chapter also allow one to deduce the ratio of electron to hole mobilities, by exploiting the different dynamics of the photoexcited charge-carrier species. As Equation 6.10 shows, this electron-hole mobility ratio is determined by the relative amplitudes of the two monoexponential decay components of the individual carrier species that comprise the overall bi-exponential photoconductivity transient. To obtain an accurate value for the mobility ratio, a globally optimised fitting procedure was performed for transients recorded for all the doped samples and excitation fluences as

outlined in Appendix B. A ratio of $\frac{\mu_e}{\mu_h} = 1.0 \pm 0.2$ was determined, indicating highly balanced electron and hole mobilities in $MAPbBr_3$ with relatively strong experimental accuracy. A value of $\frac{\mu_e}{\mu_h} = 1$ has been therefore used for all fits to the presented OPTP transients of the doped perovskites. To put these findings into literature context, for lead-halide perovskites, numerous theoretical calculations indicate similarity of electron and hole effective masses [26, 192–195], implying balanced mobilities under the assumption that scattering rates for the charge carriers are also similar. Thus, the findings shown in this chapter provide experimental evidence that bromide perovskites exhibit balanced mobilities, which, together with existing calculations on their masses, suggests that scattering rates are also similar for the two species.

6.3 Final Remarks and Conclusion

Overall, based on the observations presented herein, it is deduced that bismuth doping increases the density of point defect states in thin films of $MAPbBr_3$ perovskites. These defects trap the majority of photoexcited electrons on ultrafast timescales (10^{-10} s) and act as scattering centres for the photoexcited charge carriers, reducing their lifetimes and mobilities. Unfortunately, bismuth also cannot be used as a tool for bandgap engineering in these materials, as its presence affects neither the exciton binding energy nor the bandgap energy of the semiconductor. These conclusions can be drawn from the observations summarised in Figure 6.8, which shows an increase of the absorption edge broadening (Γ) indicating enhanced energetic disorder in the films and a decrease of charge-carrier mobility (μ), originating from higher scattering rates from defects with increasing bismuth doping of $MAPbBr_3$. The exciton binding energy (E_b) and bandgap of the semiconductors remain unaffected by doping. The trap-assisted recombination rates for electrons (k_1^e) and holes (k_1^h) increase sharply upon doping $MAPbBr_3$ even when a small amount (0.1%) of the chemical dopant is used. Upon further increase of doping

level, k_1^e and k_1^h do not rise significantly more, indicating that the number of defects introduced into the films is not directly proportional to the amount of dopant added. Since Abdelhady et al. have shown that the number of Bi ions incorporated into the crystalline structure of the perovskite grows linearly with the concentration of added $BiBr_3$ salt, [57] it is suspected that the heterovalent ions are not directly acting as electron-trapping defects. It is rather proposed that a halide excess associated with $BiBr_3$ addition leads to an enhancement of bromide interstitial formation. These halide interstitials have been shown by Motti et al. [43] to trap electrons on ultrafast timescales and to result in weak IR emission caused by slow recombination of trapped electrons with free holes, even in undoped $MAPbBr_3$ perovskites. Because the IR emission in the undoped $MAPbBr_3$ film has the same spectral shape as the sub-bandgap PL in the doped films, it is suggested that these native halide interstitials are responsible for enhanced electron trapping observed in bismuth-doped perovskites, resulting in the observed bi-exponential decay of the photoconductivity, quenching of steady-state PL intensity and time-resolved PL lifetimes and significant enhancement of IR photoluminescence. Although one cannot definitively exclude the possibility of bismuth ions forming new defect states of similar energy [184], it is believed these data provide strong evidence that the deterioration is instead caused by an associated presence of halide interstitials.

Finally, this chapter comments on the question of the influence of structural disorder on increasing the charge-carrier recombination rates in Bi-doped perovskites, which still has not been answered in the literature [67, 68, 183, 185, 186]. It is found that both the crystallinity of the films and the lattice constant of the perovskite crystals remain unaltered upon bismuth doping of $MAPbBr_3$. The analysis of the films' XRD spectra, shown in Appendix B, reveal no broadening or shifts of the diffraction peaks when bismuth is added. Moreover, the optical phonon modes of the lead-bromide lattice remain unaffected by doping, as can be seen from THz dark conductivity measurement shown in

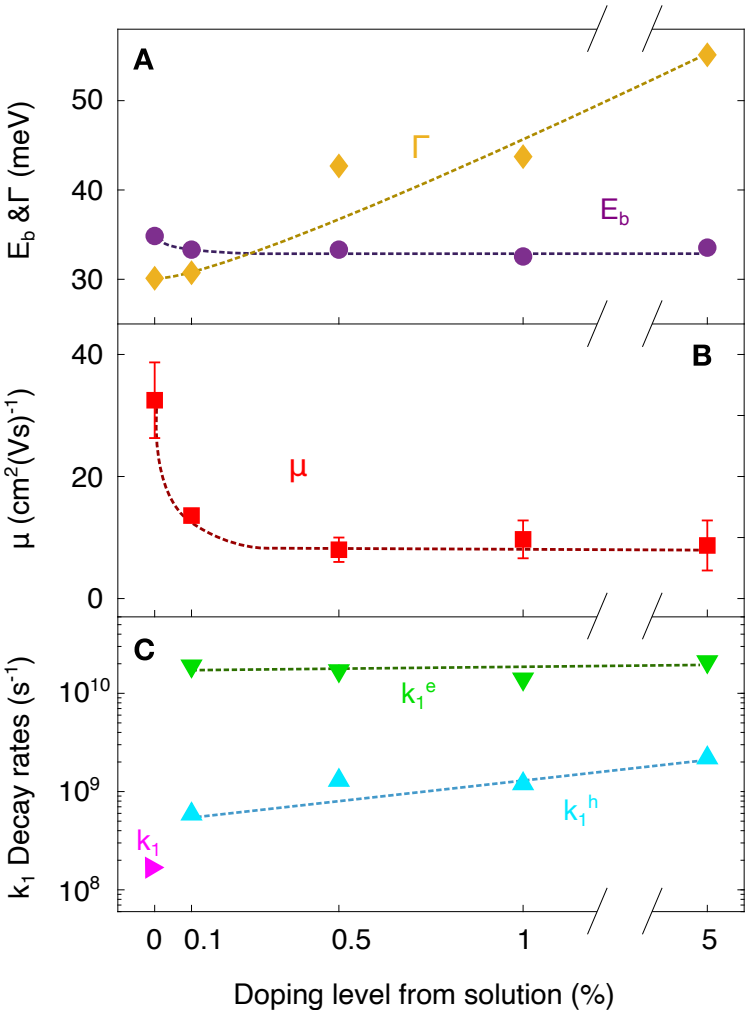


Figure 6.8: Dependence of structural and dynamical parameters on Bi doping of $MAPbBr_3$ thin films. (A) Broadening of the absorption spectrum Γ (yellow diamonds) and the exciton binding energy E_b (purple circles), obtained from fits of the Elliott model to FTIR absorption spectra. (B) Electron-hole sum mobility μ (red squares), extracted from the initial value of the photoconductivity. The error corresponds to the standard deviation of the values obtained for different excitation fluences. (C) Monomolecular decay rates extracted from fits to the OPTP transients. For the undoped $MAPbBr_3$ films, a single value of k_1 (magenta right-pointing triangle) was extracted for both electrons and holes, based on the fits of Equation 6.4 to the OPTP transients. For bismuth-doped $MAPbBr_3$ films, decay rates k_1^e (blue up-pointing triangle) and k_1^h (green down-pointing triangle) were extracted from fits of a bi-exponential function according to Equation 6.10. The monomolecular decay rates k_1^e and k_1^h were assigned to initial fast trapping of electrons and slow decay of photoexcited holes population respectively. Dotted lines are a guide to the eye only.

Appendix B. These data suggest that bismuth doping induces few structural changes, and the observed energetic broadening and accelerated charge-carrier decay must instead derive from an introduction of point defect states into the perovskite films.

In conclusion, the penultimate chapter of this thesis investigated the effect of bismuth doping on thin films of $MAPbBr_3$ perovskite. As the thin film technology is commonly used in solar cell devices, these results are directly relevant to the rapidly evolving field of perovskite photovoltaics and light-emitting applications. The initial reports of successful bismuth incorporation into perovskites indicated that bismuth doping can improve the properties of the semiconductor [181, 182] and could be used as a tool for bandgap tuning in $MAPbBr_3$ crystals [57]. However, it is here found that the addition of bismuth to the $MAPbBr_3$ thin films increases the energetic disorder in these semiconductors, without affecting the bandgap, exciton binding energy or structural properties of the crystal. Bismuth doping also lowers charge-carrier mobilities and increases monomolecular recombination rates, which in turn decreases the charge-carrier diffusion length. Such effects are potentially detrimental to the performance of the perovskite layer, raising concerns over the use of bismuth doping for PV applications of perovskite semiconductors.

Although these results present bismuth-doped $MAPbBr_3$ as a poorly performing material for the absorption layer in solar cells, they also provide valuable insights into the mechanism of charge-carrier trapping in these semiconductors. This understanding may lead to a performance improvement of doped perovskites used in photovoltaics. As the main route of charge-carrier recombination in Bi-doped $MAPbBr_3$ is through a selective trapping of electrons, reducing the density of the point defects could result in prolonged charge-carrier lifetimes, enhanced charge-carrier mobilities and diffusion lengths. Such an improvement of the optoelectronic properties of Bi-doped perovskites, together with previously reported stability and doping-induced rise of conductivity, would make bismuth a potentially interesting additive. Therefore, it is essential to find additional agents to

prevent the formation of point defects, such as halide interstitials, in these materials. In this context, all recent studies used the addition of $BiBr_3$ salt to the precursor solution as a route of bismuth doping [57, 67, 68, 181, 183], which, as suggested by Abdelhady et al. [57], results in a controlled incorporation of Bi into the perovskite crystal. However, since this method results in a bromide excess during deposition, this study found that other ways of Bi doping should be investigated to avoid the potential enhancement of bromide interstitial formation. Different heterovalent doping schemes should also be investigated in order to identify dopants that do not reduce the optoelectronic performance – as for example Ce_3^+ used in inorganic perovskites [196] or SnF_2 for tin perovskites [75]. Overall, the study summarised in this chapter provides a framework for the analysis of doping effects in hybrid perovskites, which will further the assessment of such schemes for tuning the optoelectronic properties of the active layer in perovskite solar cells.

7

Conclusion and Outlook

In this thesis, the effects of doping on the optoelectronic properties of metal-halide perovskites were investigated, unravelling important questions about the defect chemistry of doped perovskites, the impact of doping on charge-carrier cooling rate and applicability of existing terahertz data analysis framework in studying high-conductivity doped semiconductors. The importance of achieving reliable doping schemes in metal-halide perovskites was summarised in Chapter 2, which highlighted the potential benefit of achieving perovskite homojunctions on the efficiency of solar cells, currently largely limited by the selective transfer layer materials [62]. The research on the possible ways to dope metal-halide perovskites with heterovalent ions was also presented, proving that, so far, none of the existing strategies allowed obtaining higher densities of majority charge carriers than those achieved through controlling the intrinsic point defect formation in the crystal [48]. The defect chemistry was shown to be crucial in determining the optoelectronic properties of a semiconductor, as it affects the position of the Fermi level, the charge-carrier mobility and the lifetime of free carriers in the material. Moreover, since introducing additional species during the deposition process can affect this defect chemistry and lead to unwanted effects, the chapter highlighted the need for further

research into the impact of dopants on the properties of perovskites. Later, the chapter laid out the principles of operation of hot carrier photovoltaic cells, emphasising that materials with very slow charge-carrier cooling must be found to form these efficient devices. Perovskites were shown to exhibit such slow hot-carrier cooling, especially at high charge-carrier density, forming an exciting group of materials for this application [11]. The slow cooling dynamics were found to be due to the hot-phonon bottleneck effect which reduces the efficiency of the energy transfer from hot carriers to the lattice. However, some research suggested that electronic doping, especially self-doping in tin-based perovskites, can affect the charge-carrier cooling dynamics, accentuating the need for further research into charge-carrier cooling in tin-iodide perovskites [112].

Chapter 3 outlined the spectroscopic techniques and their principles of operation, proving that optical spectroscopy is an invaluable tool for assessing the applicability of novel materials for optoelectronic devices and giving details of the optical setups used in the studies described throughout the thesis. The absorption spectroscopy was shown to give a detailed insight into the energetic landscape of the investigated material, revealing its bandgap, excitonic states, energetic disorder and sometimes energetic trap states. Time-resolved and steady-state photoluminescence measurements can be used to further investigate the energetics and dynamics of the photogenerated charge carriers, which emit light during radiative band-to-band recombination (allowing for bandgap estimates from spectrally-resolved data and charge-carrier lifetime assessment from time-resolved traces) but also occasionally during the trap-assisted recombination (which again provides the information on the energy levels of these states and the dynamics of the electronic transitions). Finally, terahertz spectroscopy, the core technique of the experimental investigations presented herein, was introduced and its importance for the novel semiconductor research was explained. Knowing the optical conductivity of the material allows for the detection of free charge carriers present in the material due to

either photoexcitation or chemical doping, as well as optically-active resonant species, such as phonons and excitons. The extension of the terahertz time-domain spectroscopy (THz-TDS), the optical-pump–THz-probe (OPTP), was further shown to allow for charge-carrier mobility calculation and tracking of the free charge-carrier population temporal evolution. The charge-carrier lifetime and mobility extraction are essential for recognising the potential of a semiconductor for photovoltaic applications by allowing the calculation of the charge-carrier diffusion length, the mean distance charge carriers can travel within their lifetime, which is a great figure of merit for active-layer materials in solar cells.

The experimental part of the thesis starts with Chapter 4, a description of a computational study of the terahertz spectroscopy data analysis framework. In that chapter, it was found that approximations commonly assumed when calculating mobility in THz transmission data might not be accurate for highly doped thin films of semiconductors. The widespread Tinkham formula, allowing for calculation of the film's conductivity without photoexcitation (given by Equation 4.10 in that chapter) was shown to be applicable in thin films with conductivity up to $10^4\,\Omega^{-1}\mathrm{cm}^{-1}$, above which the optical thickness of the sample violates the thin-film approximation. This high conductivity is rarely reached by doped semiconductors, only causing issues when metallic films are studied. However, the analytical expression for photo-induced conductivity of thin films most commonly used in the field was found to be highly inaccurate when a high density of photoexcited charge-carriers is used, specifically when photoconductivity reaches about $10\,\Omega^{-1}\mathrm{cm}^{-1}$. In perovskite semiconductors, such conductivity can be easily achieved using excitations of the order $10^{17}\mathrm{cm}^{-3}$ charge-carrier pairs making this finding very important for the field. The chapter further found that in the studies of perovskite semiconductors using OPTP technique, the negligible conductivity of the un-excited sample is also assumed, which clearly is not the case when investigating properties of doped perovskite thin films. In order to account for the background conductivity of the

semiconducting films, a new analytical expression was proposed (given by Equation 4.17 in Chapter 4). The newly proposed expression proved to be highly accurate in estimating the photo-induced change of conductivity in doped semiconductors up to the background conductivity of $10^4\,\Omega^{-1}\mathrm{cm}^{-1}$, above which the thin-film approximation breaks down and numerical methods must be used for conductivity extraction from THz transmission data.

With the new tools for accurate determination of photoconductivity in doped semiconducting thin films, Chapter 5 explored the impact of high background doping on the hot-carrier relaxation dynamics in $FA_{0.83}Cs_{0.17}SnI_3$ perovskites, using a novel pump-push-probe technique described in Chapter 3. In the described study, the heating of the photoexcited (or chemically induced) charge-carrier gas resulted in a temporary drop of conductivity, found to be likely caused by stimulated THz emission from hot carriers. This change of conductivity was tracked on ultrafast timescales to obtain the hot-carrier cooling rate in the presence of the background dopants. A fast, sub-picosecond hot carrier cooling timescale was found to be independent of the density of the introduced hot carriers. This showed that the novel method can be used for measuring hot-carrier dynamics in the low hot-carrier density regime, below the hot-phonon bottleneck effect, which slows down the carrier cooling at high excitation densities. Pump–push–THz-probe can therefore extract cooling dynamics more representative of those occurring under solar illumination. Under such conditions of low hot-carrier density, the dependence of the cooling dynamics on the provided excess excitation energy (which showed faster cooling for the shorter wavelength of push pulse) helped to identify the hot-carrier–cold-carrier scattering as the main mechanism responsible for such ultrafast energy loss. The chapter concluded that in order to realise hot carrier solar cells with tin-iodide perovskites, suitable doping-suppression methods must be found to reduce the density of free holes in these materials and further prolong their hot carrier cooling dynamics.

The final experimental chapter of this thesis, Chapter 6, investigated the effect of bismuth doping on the optoelectronic properties of $MAPbBr_3$ perovskite thin films. The addition of bismuth in the form of $BiBr_3$ salt to the precursor solution during the deposition process was found to increase the energetic disorder in the films, apparent as a broadening of the spectral absorption onset of the films. The closer evaluation uncovered an infrared emission, likely stemming from the electron trapping and recombination process mediated by bromide interstitial defect states. These defects appeared to be enhanced either by the presence of bismuth or by the method of bismuth incorporation, which could have created bromine excess during perovskite formation. The dynamic evolution of the charge-carrier dynamics studied using OPTP spectroscopy and TRPL traces further confirmed the selective electron trapping mechanism and estimated the electron trapping timescale to be of the order of hundreds of picoseconds. The following radiative relaxation of the trapped electrons to the valence band was found to be around one order of magnitude slower. The research presented in that chapter highlighted the need for a holistic assessment of metal-halide perovskite doping schemes looking at the effects of doping on both structural and optoelectronic properties of the semiconductor and ensuring that benefits gained by the successful doping on the active layer are not outweighed by the deterioration of the material's performance.

Overall, this thesis presented research into the electrical doping of metal-halide perovskites and its effect on the fundamental properties of these materials. Further investigations should assess the effects of other dopants on the optoelectronic properties of metal-halide perovskites, especially of heterovalent metals like silver and antimony, which showed promising effects on the efficiency of the PV devices [59, 71, 72]. A detailed investigation of the impact of doping on the charge-carrier cooling rate should also be conducted in order to identify the critical density of dopants for which the main energy loss pathway changes from phonon scattering to carrier-carrier scattering. This knowledge

could further inform the efforts of doping suppression in tin-iodide perovskites to enable these semiconductors to be incorporated into hot-carrier photovoltaics. Furthermore, novel doping schemes that extend beyond impurity inclusions should be developed. The encouraging results of using molecular dopants in perovskite semiconductors suggest that further investigation of this approach may yield significant improvements in the efficiencies of perovskite-based solar cells [197–199]. This strategy of depositing highly doped molecules on top of a perovskite film leads to a Fermi level shift near the interface [197], without significantly affecting the bulk properties of the active layer (in contrast to heterovalent ion doping) therefore promising robust electrical doping schemes that could improve charge-carrier extraction efficiency.

Appendices

A

Supplementary Characterisation and Data for Chapter 5

A.1 Absorption Measurements

The measurements of the absorbance of the thin film samples used for estimates of photoexcited charge-carrier density were performed as described in Section 3.1.1 of Chapter 3. The fraction of absorbed photons ψ at 800 nm wavelength (wavelength of the pump in photoconductivity experiments) was estimated as $\psi = 1 - R - T$ for both films, obtaining ~81% photon absorption in $FA_{0.83}Cs_{0.17}SnI_3$ with 20% SnF_2 and ~58% in the $FA_{0.83}Cs_{0.17}SnI_3$ thin film with no tin-fluoride added.

A.2 Sample Fabrication

Note: sample fabrication was performed by Michael D. Farrar, Optoelectronic Devices Group, Department of Physics, University of Oxford.

A 1.2 M parent solution of $FA_{0.83}Cs_{0.17}SnI_3$ was prepared 12 hours before sample fabrication, in the mixed solvent of dimethylformamide (DMF) and dimethyl sulfoxide (DMSO) in volumetric ratio of 4:1. 3 mL solution of $FA_{0.83}Cs_{0.17}SnI_3$ was prepared using 513.85 mg of FAI, 159.00 mg of CsI, 1341.07 mg of tin (II) iodide (SnI_2, Alfa Aesar,

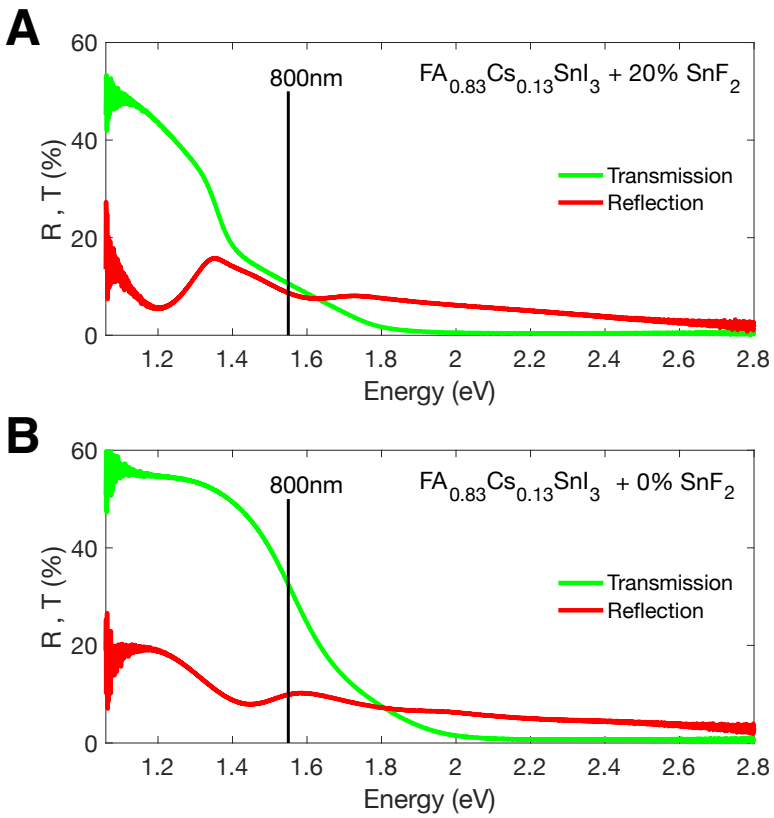


Figure A.1: The fraction of the transmitted (green) and reflected (red) light through thin films of $FA_{0.83}Cs_{0.17}SnI_3$ perovskite with either **A** 20% or **B** 0% SnF_2 added during the fabrication process. The photon energy of the 800 nm wavelength pump pulses used for photoexcitation in the PPP experiments is indicated by a solid black line.

99.999% mesh beads), and tin (II) fluoride (SnF_2, Sigma Aldrich) corresponding to 0 or 20 mol% as indicated in the discussion in the main text. Previous studies have demonstrated that the tin fraction in mixed tin-lead perovskites is well controlled by the stoichiometry of the precursor solution, independent of whether SnF_2 additive is used.[25, 74, 200–203]

Z-cut quartz substrates (2 mm thick, 13 mm diameter discs) were prepared by sonicating sequentially in Decon 90 detergent (1% vol. in deionized (DI) water), DI water, acetone and ethanol for 10 min followed by O_2 plasma treatment for 15 min. Films were deposited onto quartz using a single-step antisolvent quenching method in a nitrogen-filled glovebox ($H_2O \leq 0.1$ ppm, $O_2 \leq 1.0$ ppm). 20 μL of the required solution was dispensed onto a static substrate and spun at 4000 rpm with an acceleration of 500 rpm for a

total of 60 s. At 35 s, 100μL of anisole was dispensed into the center of the substrate at a height of roughly 5 mm from the surface in a steady stream taking around 1 s to fully dispense. The films turned very dark brown to black instantly. Substrates were then transferred straight onto a hotplate and annealed for 10 min at 100 °C resulting in specular black films. All film preparation parameters were kept constant for each sample. After annealing, all samples were stored in a nitrogen-filled glovebox.

A.3 Photoconductivity Calculation

The photo-induced change of conductivity (called just "photoconductivity") can be calculated using the formula described by Equation 4.18 in Chapter 4,

$$\sigma_{\text{photoconductivity}} = -\frac{\Delta T}{T+\Delta T}\left[\frac{\epsilon_0 c(1+n_{\text{substrate}})}{L}\right]\frac{T_{\text{substrate}}}{T}, \tag{A.1}$$

where T represents the strength of the transmitted THz field through the sample in the dark and ΔT is the photo-induced change of transmission upon photoexcitation ($\Delta T = T_{\text{photoexcited}} - T_{\text{dark}}$). Equation A.1 was used to calculate the spectral conductivities shown in Figure 5.7 A and B of Chapter 5, with the term $\frac{T_{\text{substrate}}}{T}$ set to 1 when calculating the photoconductivity of $FA_{0.83}Cs_{0.17}SnI_3$ perovskite with 20% SnF_2 included in the fabrication, because of its low dark conductivity and in order to avoid the additional introduction of experimental uncertainties caused by phase errors in the THz-TDS measurements [136].

Because of the proportionality between the photoconductivity and the experimentally determined quantity $-\frac{\Delta T}{T+\Delta T}$, this relative change of frequency-averaged THz transmission was used (measured at the time-domain peak of the THz probe) to illustrate the photoconductivity transients in Chapter 5, following the methodology developed in Chapter 4.

A.4 Push-Wavelength Dependence and Decay Fitting

The wavelength dependence of the push-induced photoconductivity transient was measured in a push-probe (no pump) experiment using the highly hole-doped thin film of $FA_{0.83}Cs_{0.17}SnI_3$ (no SnF_2).

Figure A.2 shows the push-induced photoconductivity traces for excitation wavelengths varied between 1200 nm and 2000 nm. All decay traces of the photoinduced conductivity change $\Delta\sigma$ have been fitted with monoexponential decay curves that were convoluted with a Gaussian broadening representing the temporal resolution of the setup:

$$\Delta\sigma = \left[\exp\frac{-(t+t_{\text{offset}})^2}{2s^2}\right] * \left[a\exp\left(\frac{-t}{\tau}\right)\frac{\text{sgn}(t)+1}{2}\right] \tag{A.2}$$

where t_{offset} is an arbitrary time offset to the push pulse arrival, s is the standard deviation of the Gaussian function representing the system time resolution, a is the magnitude of the signal strength and τ is the monoexponential lifetime of the decay. The sign function sgn(t) has a value of -1 for t<0 and +1 for t>0, such that the last factor represents the step-like onset of a photoconductivity transient for the case of instantaneous photoexcitation. The temporal resolution of the system s had been first determined as 200 fs by fitting all presented traces with Equation A.2 and setting an average resolution from values obtained from these fits. For the presented fitting curves drawn in darker solid lines in Figure A.2, a fixed value of $s = 200$ fs was therefore used. The same Equation A.2 was used for fitting the photoconductivity transients shown in Figure 5.5 in Chapter 5, with the decay time determined from the fit to the highest fluence data (to minimise the effect of the noise at low fluences) which was then subsequently fixed for all fits to lower-fluence curves.

Figure A.3 shows the dependence of the push-induced conductivity decrease (evaluated in terms of the signal strength parameter a, as defined in Equation A.2) on the wavelength

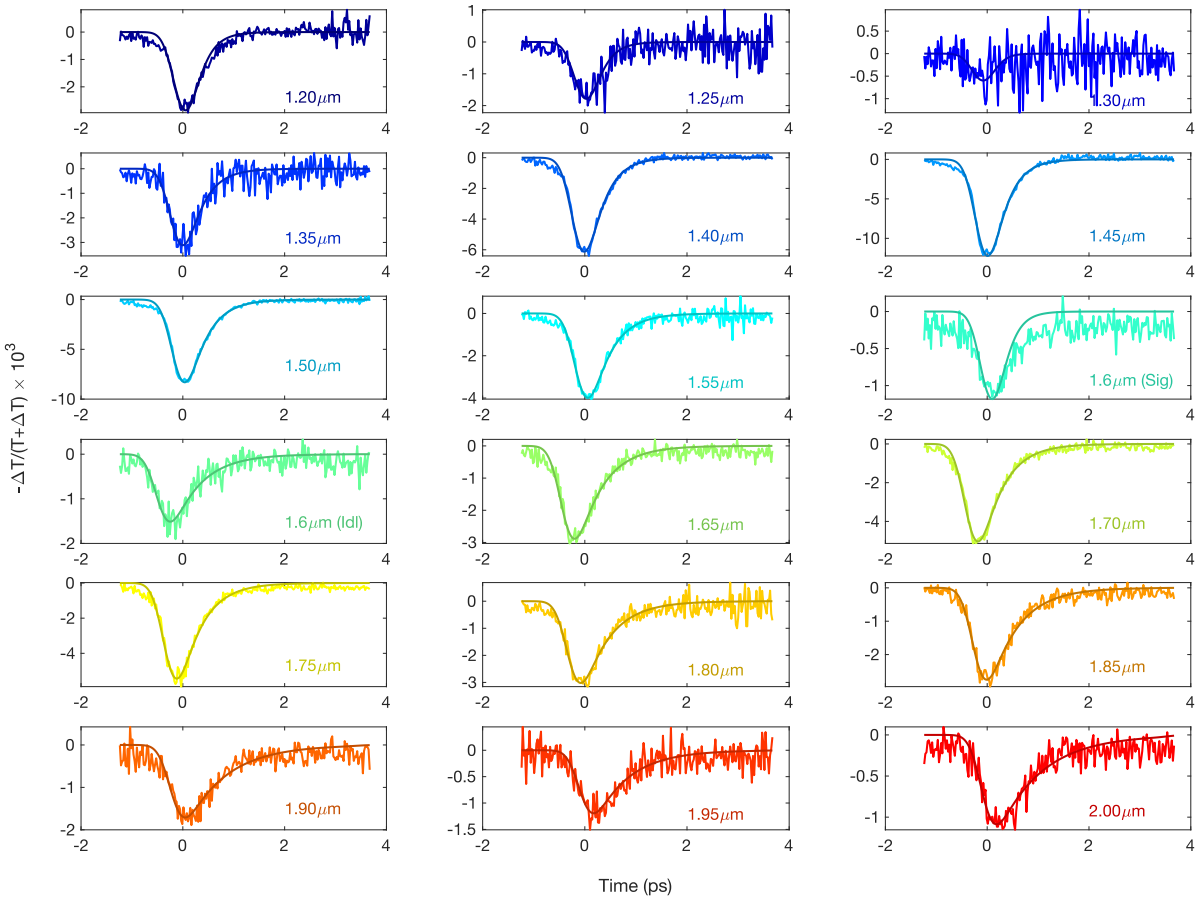


Figure A.2: Negative photoconductivity transients following sub-bandgap IR excitation of a hole-doped thin film of $FA_{0.83}Cs_{0.17}SnI_3$ (no tin fluoride added during fabrication). The wavelength of the IR push pulse was varied between 1200 nm (dark blue) and 2000 nm (red), with the 1600 nm wavelength experiment taken once each for the two possible sources of the pulse (originating either from idler or signal beam of the optical parametric amplifier). The fits according to Equation A.2 are shown in darker solid lines on top of the data and the obtained monoexponential decay times of the transients are shown in Figure 5.6 in Chapter 5.

of the push pulse used. The signal strength was normalized by the fluence of the push pulse and shows no strong wavelength dependence compared to the measurement uncertainty.

A.5 Investigation of the Origin of the Negative Photoconductivity

A light-induced decrease in THz conductivity has previously been observed in low-dimensional doped semiconductors [155, 175–178]. However, existing reports of this negative photoconductivity attributed the phenomenon to a range of different mech-

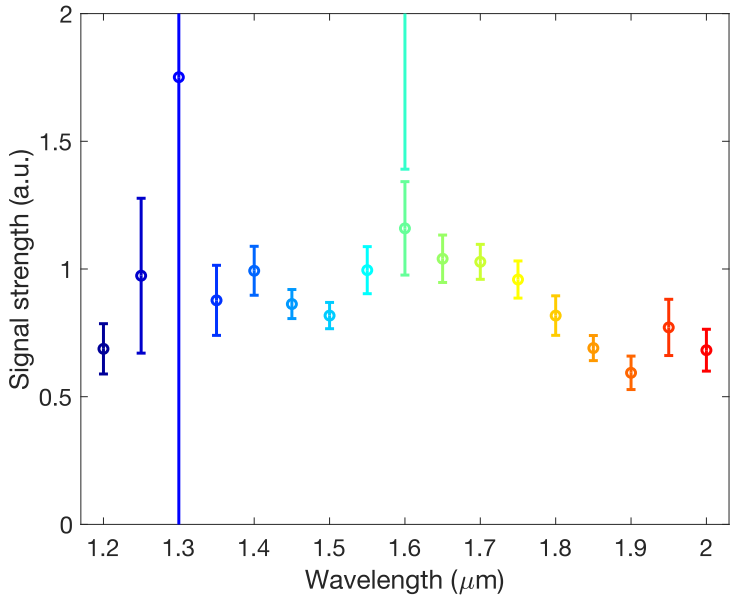


Figure A.3: Magnitude of the negative photoconductivity strength a, defined in Equation A.2, normalized by fluence of the push pulse. The error bars represent the uncertainty of the laser power measurement combined with 95% confidence intervals of the fitting parameter obtained from fitting Equation A.2 to data shown in Figure A.2 .

anisms, even when the same material was considered [175–178], exposing the lack of agreement in the field about the origin of this effect. In the study presented in Chapter 5, thin films of three-dimensional bulk perovskite semiconductors were investigated. Therefore, the proposed mechanisms were considered in the context of the presented data, excluding previously proposed negative photoconductivity origins that are specific to low-dimensional systems [178].

One of the proposed mechanisms resulting in negative photoconductivity is a decrease of charge-carrier scattering rate upon the incidence of light, with a simultaneous increase of the charge-carrier effective mass [155]. This effect would result in Drude conductivity that decreases faster with increasing probe frequency as a result of the lowered charge-carrier scattering rate but remains unchanged for low probe frequencies because the increase of charge-carrier effective mass compensates for the increased mobility. The

frequency dependence of Drude-like conductivity is described by

$$\sigma_{\mathrm{Drude}}(\omega) = \frac{\sigma_{\mathrm{DC}}}{1 - i\omega\tau}\,, \tag{A.3}$$

where τ is the charge-carrier scattering time (or the inverse of the momentum relaxation rate) and σ_{DC} is the low-frequency value of the conductivity. The DC conductivity itself depends on the density of charge carriers n, their effective mass m^* and scattering time: $\sigma_{\mathrm{DC}} = ne^2\tau/m^*$. This model of negative photoconductivity assumes that although the charge-carrier scattering time increases, the overall DC conductivity remains fortuitously unchanged as a result of an exactly compensating rise of effective mass.

Figure A.4 shows the simulated Drude conductivity spectra, before (Push-OFF) and after (Push-ON) IR excitation of the thin film. Figure A.4A displays in a light-red (Push-OFF) solid line the real part and in a dotted line the imaginary part of a Drude conductivity spectrum for a hybrid-perovskite-like semiconductor. The charge-carrier scattering rate was set to $\tau_{\mathrm{Push-OFF}}$ =1.7 fs as determined previously for tin-iodide perovskites [75]. The calculated conductivity spectrum after IR excitation (Push-ON) is shown in dark-red lines and it features unchanged DC conductivity and increased charge-carrier scattering time. The inset in this figure shows the push-induced change of the conductivity spectra, $\Delta\sigma = \sigma^{\mathrm{Push-ON}} - \sigma^{\mathrm{Push-OFF}}$, with the empty hoops and filled circles representing the imaginary and real parts of the measured push-induced photoconductivity respectively and solid lines showing fits to the data based on the model described above. The charge-carrier scattering time after IR photoexcitation was determined using a least-squares fitting method as $\tau_{\mathrm{Push-ON}} = 0.29$ ps. However, such a change in charge-carrier scattering rate would increase the mobility, and therefore the DC conductivity by a factor of $\tau_{\mathrm{Push-ON}}/\tau_{\mathrm{Push-OFF}} = 170$, requiring a rise of the effective mass by the same amount to explain the observed unchanged value of the conductivity at low probe frequencies ($\Delta\sigma \sim 0$ at $\omega = 0$). Figure A.4B shows the same

calculation as shown in subfigure A, relaxing the condition of the initial scattering time being set to $\tau_{\mathrm{Push-OFF}}$ =1.7 fs but limiting the relative change of scattering time to 20%. Although this model shows improved quality of the fits in comparison to data, replicating important spectral features, such as the zero-crossing of the imaginary part, the obtained charge-carrier scattering times are $\tau_{\mathrm{Push-OFF}}$ =65.7 fs and $\tau_{\mathrm{Push-ON}}$ =78.8 fs, which is incompatible with the measured photoconductivity spectra presented in Figure 5.7 in Chapter 5, which reveal much shorter charge-carrier scattering times (flatter spectral responses). This explanation is therefore excluded as a possibility for the negative photoconductivity in the case of the tin-iodide perovskite thin films investigated here.

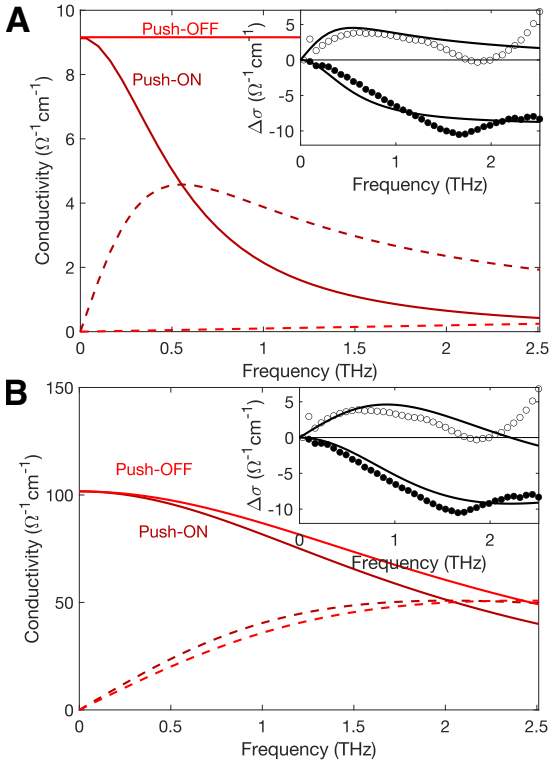


Figure A.4: **A** Conductivity spectrum of a hybrid-perovskite-like semiconductor calculated without the presence of an IR pulse (Push-OFF: light-red lines) and after IR excitation (Push-ON: dark-red lines). The real part of the conductivity is shown in solid and the imaginary part in dotted lines. The spectrum was calculated using Equation A.3, setting $\tau = \tau_{\text{Push-OFF}}$ =1.7 fs for the Push-OFF spectrum and leaving σ_{DC} as a free parameter, which was evaluated together with the scattering time of the charge-carriers after IR excitation ($\tau_{\text{Push-ON}}$) by fitting the push-induced change in the conductivity spectra, $\Delta\sigma = \sigma^{\text{Push-ON}} - \sigma^{\text{Push-OFF}}$, to the data shown in the inset. The inset contains the real (filled circles) and imaginary (empty hoops) parts of the photoconductivity spectrum of for $FA_{0.83}Cs_{0.17}SnI_3$ thin film to which no SnF_2 had been added during fabrication (high doping levels), measured in the same way as the spectrum shown in Figure 5A in the main text. The solid black lines show the fit to data, resulting in $\tau_{\text{Push-ON}}$ = 0.29 ps and σ_{DC}=9.16 Ω^{-1}cm^{-1}. **B** Calculated conductivity spectra equivalent to those displayed in (A) but with the relative change of charge-carrier scattering time limited to 20%, resulting in an optimal fit for σ_{DC}=101.7 Ω^{-1}cm^{-1}, $\tau_{\text{Push-OFF}}$ =65.7 fs and $\tau_{\text{Push-ON}}$ =78.8 fs.

B

Supplementary Data for Chapter 6

Contents

B.1 Sample Preparation 147
B.2 THz Photoconductivity 148
B.2.1 Determination of the Ratio of Electron to Hole Mobility 148
B.2.2 OPTP-Full Dataset 149
B.3 Structural Characterisation 150
B.3.1 X-Ray Diffraction 150
B.3.2 Phonon Modes 152

This appendix provides details of sample preparation and characterisation relevant to Chapter 6. It also describes methods used for data fitting in Chapter 6 and presents additional data to back the conclusions made in that chapter.

B.1 Sample Preparation

Note: Sample preparation was performed by Dr Bernard Wenger (Photovoltaic and Optoelectronic Device Group, Department of Physics, University of Oxford).

To obtain the precursor solutions, a 1.25 M $MAPbBr_3$ stock solution was prepared by dissolving 140 mg of MABr (Dyesol) and 459 mg of $PbBr_2$ (Alfa Aesar) per 1 mL of a solvent mixture of N'N-Dimethyl Formamide (DMF) and Dimethyl sulfoxide (DMSO) (in 4:1 volume ratio), and separately another stock solution of 1.25 M $BiBr_3$ (Sigma-Aldrich) was made in the same solvent (DMF/DMSO 4:1). The stock solutions were heated at 60°C for 15 min to accelerate the dissolution of the salts. The doped precursor solutions were made from the stock solutions with the following volumetric ratios: 0.1:99.9, 0.5:99.5, 1:99 and 5:95 ($BiBr_3$:$MAPbBr_3$, 1.25 M stock solutions). Despite the slightly decreasing concentration, the changes in thickness of the deposited films were negligible, according to their similar optical transmittance.

Thin films of $MAPbBr_3$ were deposited on z-cut quartz, 13 mm-diameter, 2 mm-thick disks. The substrates were cleaned in an ultrasonic bath with a sequence of soap (2% Hellmanex in deionised water), acetone and isopropanol, and finally treated under oxygen plasma for 10 min to remove organic residues. The solutions were spin-coated onto the substrates (1000 rpm for 10 s, then 6000 rpm for 35 s). A solvent-quenching step was then performed by quickly dropping 100 μL of anisole 10 s before the end of the spin-coating program. The films were then annealed at 100°C for 60 min on a hotplate and allowed to cool to room temperature.

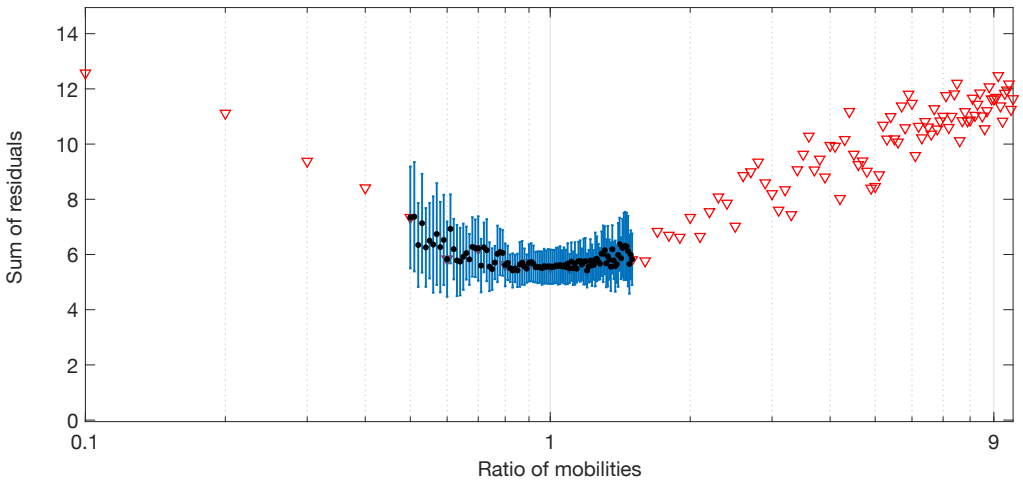


Figure B.1: Global optimisation of the fitting parameter 'r', representing the ratio of electron and hole mobilities, used in modelling photoconductivity decays. Two optimisation procedures have been used: coarse (red triangles) and fine (black dots) to find the optimal value of the parameter that minimises the sum of residuals for all fits to OPTP data for the doped samples. The value of $r = 1 \pm 0.2$ results in the lowest sum of residuals, therefore providing the best fit quality. The blue errorbars represent the standard deviation of the sums of residuals across all fits for the fine scan.

B.2 THz Photoconductivity

B.2.1 Determination of the Ratio of Electron to Hole Mobility

Due to the fast, selective trapping of electrons in bismuth-doped $MAPbBr_3$ thin films, the monomolecular decay constants of electrons and holes are significantly different, resulting in a bi-exponential decay of the photoconductivity (as seen in Equation 6.9 in Chapter 6). Since the electric conductivity is proportional to the number density and mobility of the charge carriers, the contribution of each exponential component to that bi-exponential decay is weighted by the mobility of electron and hole respectively. Hence, the ratio of the electron to hole mobility, $r = \frac{\mu_e}{\mu_h}$ has to be determined in order to fit the bi-exponential function to the photoconductivity decay traces.

In order to determine the ratio of the electron to hole mobility, a computational fitting procedure was performed, stepping through the values of $r = \frac{\mu_e}{\mu_h}$ while fitting globally all the measured photoconductivity decay traces of the doped samples. For each value of r, the

program calculates the sum of residuals of all the fits, representing the overall goodness of fits. This output has been plotted as a function of r in Figure B.1. The value of $r = 1$ was used globally for all fits presented in Chapter B, as it results in the lowest sum of residuals.

The de-coupled behaviour of the electron and hole photoconductivity caused by selective electron trapping provides a unique insight into the mobility differences between the different charge carriers. These are usually obstructed by the similar decay rates of electrons and holes and only the total sum of mobilities can therefore typically be determined using OPTP measurements.

B.2.2 OPTP-Full Dataset

The photoconductivity decay traces for all samples are shown in Figure B.2. Note that Figure 6.6 in Chapter 6 only showed a selected subset of these decays. Data for each doped sample were globally fitted for all excitation fluences with the bi-exponential decay function according to Equation 6.9 in Chapter 6 and the ratio of electron to hole mobilities $r = 1$ was used for all doped samples. The data for the undoped sample were fitted with a solution to Equation 6.3, given by Equation 6.4. The samples were photoexcited at 400 nm with fluences given in the legends using laser system described by Section 3.4 in Chapter 3.

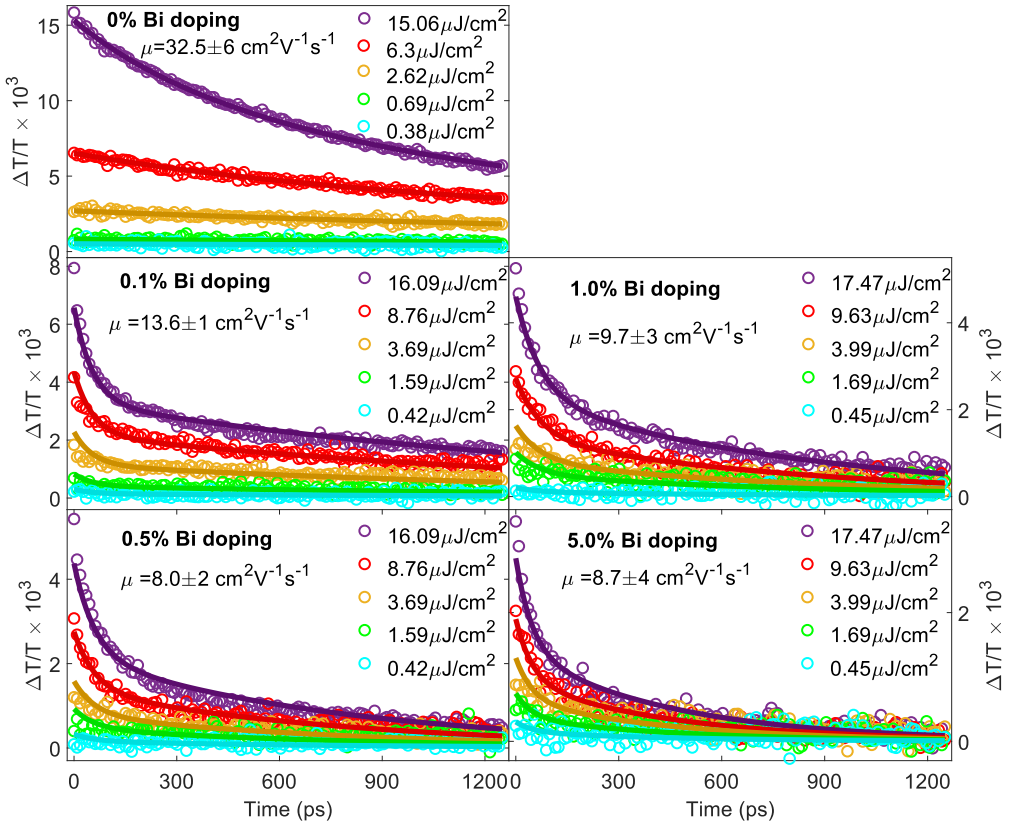


Figure B.2: Photoconductivity decay traces for bismuth-doped thin films of $MAPbBr_3$ following excitation with a 35 fs duration, 400 nm wavelength laser pulse. The solid lines represent fit to the data (open circles) as explained in the main text. Excitation fluences are shown in the legends for each sample.

B.3 Structural Characterisation

B.3.1 X-Ray Diffraction

The crystallinity of the thin films was characterised using an X-Ray Diffraction (XRD) measurement. A '$\theta : 2\theta$' scan was used with a copper K_α X-ray source. The diffraction patterns are shown in Figure B.3. The spectra were corrected for tilt of the sample using the quartz substrate diffraction peak at 16.43° as a reference [204].

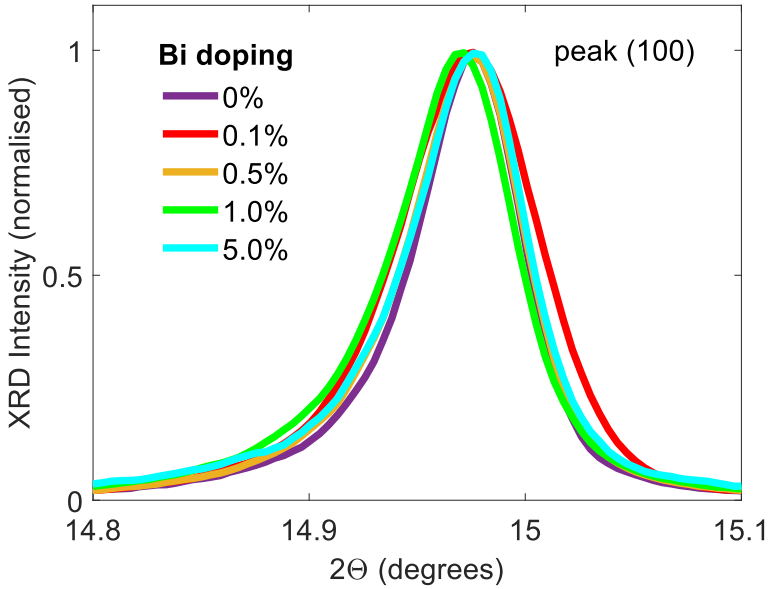


Figure B.4: Normalised (100) X-ray diffraction peak, showing no correlation of peak broadening or position with bismuth doping level.

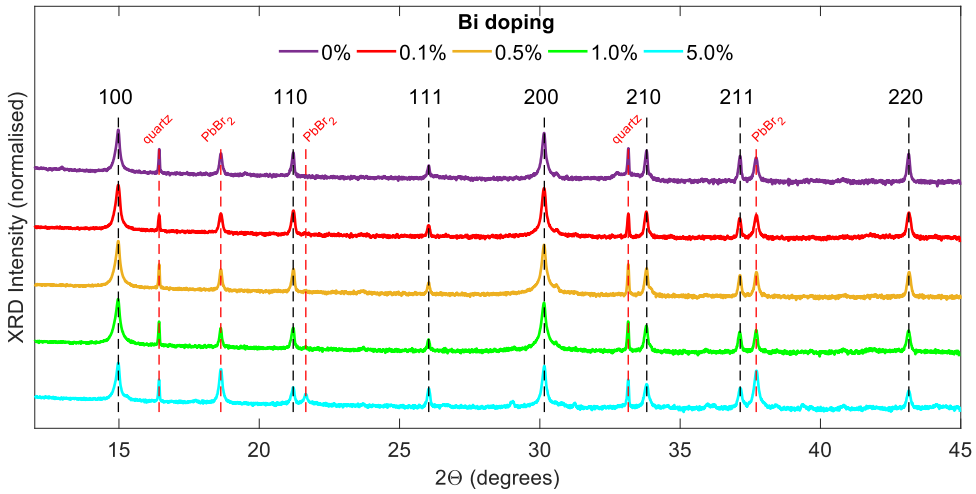


Figure B.3: XRD spectra of bismuth-doped thin films of $MAPbBr_3$. The position of the peaks is unaffected by bismuth doping and closely resembles powder diffraction spectra of $MAPbBr_3$ reported by Wang et al. [205] Diffraction patterns are shown on a logarithmic scale and are offset from each other vertically for better visibility of the diffraction peaks.

Independently of the doping level, all spectra show peaks at the diffraction angles that are consistent with previous reports of XRD spectra for $MAPbBr_3$ [205]. To further investigate the effect of bismuth doping on the structure of the material, both the intensity and broadening of the (100) diffraction peaks was compared for different doping levels.

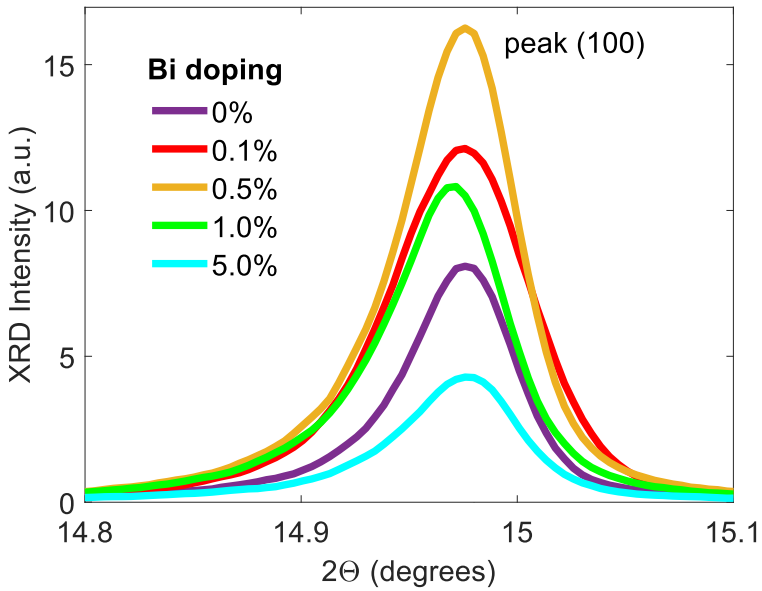


Figure B.5: Unnormalised (raw) (100) X-ray difration peak, showing no correlation of intensity of the peak with doping level.

From Figures B.4 and B.5 one can see that neither intensity nor broadening of the peak correlates with the doping level. The presence of bismuth has therefore a negligible effect on the crystallinity of these perovskite thin films, as larger crystallites would result in sharper diffraction peaks. The incorporation of bismuth into the perovskite crystals also does not change the lattice parameter, which would have caused shifts of the peak positions in the diffraction pattern. Therefore, in agreement with the observation that the bandgap is unaffected by doping, the presence of bismuth doping most likely leads to the introduction of point defects, either by enhancing the point defects already present in the $MAPbBr_3$ crystals [43] or by introducing new trapping energy states of very similar energetics to the halide interstitials [184].

B.3.2 Phonon Modes

In order to further examine the potential structural changes upon bismuth doping, the THz transmission spectra of the perovskite thin films were measured in the dark (no photoexcitation) to investigate the optical phonon modes of the lead-bromide lattice

present in this spectral region, which had previously been observed by Zhao et al. [206] for undoped $MAPbBr_3$. Figure B.6 shows the THz transmission spectra, presented as imaginary and real parts of the complex dark conductivity of the thin films. Bismuth doping has no effect on the spectral position and intensity of the peaks, and therefore it has no significant effects on the perovskite structure.

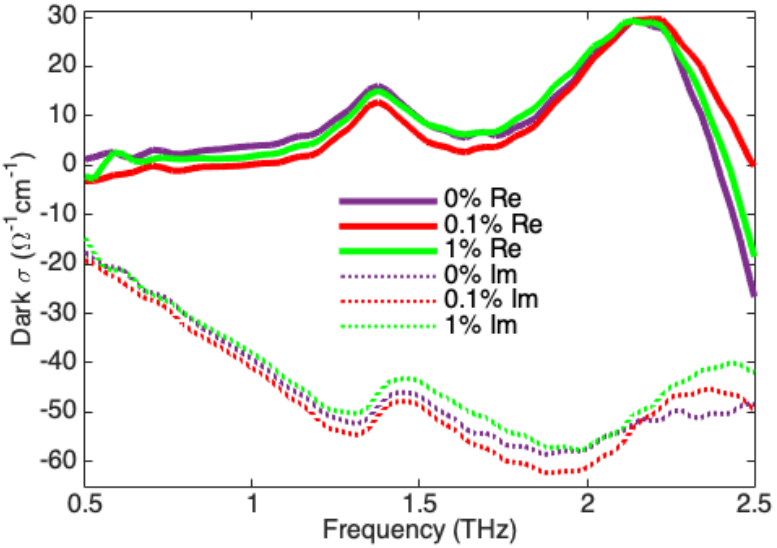


Figure B.6: The position of the optical phonon modes of the lead-bromide lattice in $MAPbBr_3$ films, revealed by THz dark conductivity study show no changes when bismuth is added. This suggests bismuth doping does not result in significant changes to the crystal structure.

References

[1] United Nations, Department of Economic and Social Affairs, Population Division (2022). 'World Population Prospects 2022: Ten Key Messages'. https://population.un.org/wpp/Publications (accessed 12 Jan 2023).

[2] IEA (2022). 'World Energy Outlook 2022'. License: CC BY 4.0 (report); CC BY NC SA 4.0 (Annex A), Paris, www.iea.org/reports/world-energy-outlook-2022 (accessed 12 Jan 2023).

[3] Shukla, P.; Skea, J.; Slade, R.; Al Khourdajie, A.; Van Diemen, R.; McCollum, D.; Pathak, M.; Some, S.; Vyas, P.; Fradera, R.; Belkacemi, M.; Hasija, A.; Lisboa, G.; Luz, S. and Malley, J. 'Climate Change 2022: Mitigation of Climate Change. Contribution of Working Group III to the Sixth Assessment Report of the Intergovernmental Panel on Climate Change'. *IPCC. Cambridge University Press, Cambridge, UK and New York, NY, USA*, 2022.

[4] Shukla, P.; Skea, J.; Calvo Buendia, E.; Masson-Delmotte, V.; Pörtner, H.-O.; Roberts, D. C.; Zhai, P.; Slade, R.; Connors, S.; Van Diemen, R.; Ferrat, M.; Haughey, E.; Luz, S.; Neogi, S.; Pathak, M.; Petzold, J.; Portugal Pereira, J.; Vyas, P.; Huntley, E.; Kissick, K.; Belkacemi, M. and Malley, J. 'Summary for Policymakers. In: Climate Change and Land: an IPCC special report on climate change, desertification, land degradation, sustainable land management, food security, and greenhouse gas fluxes in terrestrial ecosystems'. *IPCC. In press*, 2019.

[5] Arafa, M. I. A. and Said, E.-S. S. A. 'A different vision for uninterruptible load using hybrid solar-grid energy'. *International Journal of Power Electronics and Drive System*, 2019, **10**, 381–387.

[6] Kilgore, G. 'Solar Farm Income Per Acre Calculator: See Profit Margin, Costs, Money Made'. https://8billiontrees.com/solar-panels/solar-farm-income-per-acre/ (accessed 12 Jan 2023).

[7] National Renewable Energy Laboratory. 'NREL Efficiency Chart'. www.nrel.gov/pv/cell-efficiency.html (accessed 12 Jan 2023).

[8] Snaith, H. J. 'Present status and future prospects of perovskite photovoltaics'. *Nature Materials*, 2018, **17**, 372–376.

[9] Kim, H.-S.; Lee, C.-R.; Im, J.-H.; Lee, K.-B.; Moehl, T.; Marchioro, A.; Moon, S.-J.; Humphry-Baker, R.; Yum, J.-H.; Moser, J. E. *et al.* 'Lead iodide perovskite sensitized all-solid-state submicron thin film mesoscopic solar cell with efficiency exceeding 9%'. *Scientific reports*, 2012, **2**, 1–7.

[10] Lee, M. M.; Teuscher, J.; Miyasaka, T.; Murakami, T. N. and Snaith, H. J. 'Efficient hybrid solar cells based on meso-superstructured organometal halide perovskites'. *Science*, 2012, **338**, 643–647.

[11] Li, M.; Fu, J.; Xu, Q. and Sum, T. C. 'Slow hot-carrier cooling in halide perovskites: prospects for hot-carrier solar cells'. *Advanced Materials*, 2019, **31**, 1802486.

[12] Ross, R. T. and Nozik, A. J. 'Efficiency of hot-carrier solar energy converters'. *J. Appl. Phys.*, 1982, **53**, 3813–3818.

[13] Kim, H.-S.; Im, S. H. and Park, N.-G. 'Organolead halide perovskite: new horizons in solar cell research'. *The Journal of Physical Chemistry C*, 2014, **118**, 5615–5625.

[14] O'regan, B. and Grätzel, M. 'A low-cost, high-efficiency solar cell based on dye-sensitized colloidal TiO_2 films'. *nature*, 1991, **353**, 737–740.

[15] Grätzel, M. 'Photoelectrochemical cells'. *Nature*, 2001, **414**, 338–344.

[16] Kojima, A.; Teshima, K.; Shirai, Y. and Miyasaka, T. 'Organometal halide perovskites as visible-light sensitizers for photovoltaic cells'. *Journal of the American Chemical Society*, 2009, **131**, 6050–6051.

[17] Im, J.-H.; Lee, C.-R.; Lee, J.-W.; Park, S.-W. and Park, N.-G. '6.5% efficient perovskite quantum-dot-sensitized solar cell'. *Nanoscale*, 2011, **3**, 4088–4093.

[18] Green, M. A.; Ho-Baillie, A. and Snaith, H. J. 'The emergence of perovskite solar cells'. *Nature photonics*, 2014, **8**, 506.

[19] Byranvand, M. M.; Otero-Martínez, C.; Ye, J.; Zuo, W.; Manna, L.; Saliba, M.; Hoye, R. L. and Polavarapu, L. 'Recent Progress in Mixed A-Site Cation Halide Perovskite Thin-films and Nanocrystals for Solar Cells and Light-Emitting Diodes'. *Advanced Optical Materials*, 2022, **10**, 2200423.

[20] Prasanna, R.; Gold-Parker, A.; Leijtens, T.; Conings, B.; Babayigit, A.; Boyen, H.-G.; Toney, M. F. and McGehee, M. D. 'Band gap tuning via lattice contraction and octahedral tilting in perovskite materials for photovoltaics'. *Journal of the American Chemical Society*, 2017, **139**, 11117–11124.

[21] Savill, K. J.; Ulatowski, A. M. and Herz, L. M. 'Optoelectronic properties of tin–lead halide perovskites'. *ACS Energy Letters*, 2021, **6**, 2413–2426.

[22] Goldschmidt, V. M. 'Die gesetze der krystallochemie'. *Naturwissenschaften*, 1926, **14**, 477–485.

[23] Li, Z.; Yang, M.; Park, J.-S.; Wei, S.-H.; Berry, J. J. and Zhu, K. 'Stabilizing perovskite structures by tuning tolerance factor: formation of formamidinium and cesium lead iodide solid-state alloys'. *Chemistry of Materials*, 2016, **28**, 284–292.

[24] Turren-Cruz, S.-H.; Hagfeldt, A. and Saliba, M. 'Methylammonium-free, high-performance, and stable perovskite solar cells on a planar architecture'. *Science*, 2018, **362**, 449–453.

[25] Stoumpos, C. C.; Malliakas, C. D. and Kanatzidis, M. G. 'Semiconducting tin and lead iodide perovskites with organic cations: phase transitions, high mobilities, and near-infrared photoluminescent properties'. *Inorg. Chem.*, 2013, **52**, 9019–9038.

[26] Protesescu, L.; Yakunin, S.; Bodnarchuk, M. I.; Krieg, F.; Caputo, R.; Hendon, C. H.; Yang, R. X.; Walsh, A. and Kovalenko, M. V. 'Nanocrystals of cesium lead halide perovskites ($CsPbX_3$, X= Cl, Br, and I): novel optoelectronic materials showing bright emission with wide color gamut'. *Nano Letters*, 2015, **15**, 3692–3696.

[27] Noh, J. H.; Im, S. H.; Heo, J. H.; Mandal, T. N. and Seok, S. I. 'Chemical management for colorful, efficient, and stable inorganic–organic hybrid nanostructured solar cells'. *Nano Letters*, 2013, **13**, 1764–1769.

[28] Kulkarni, S. A.; Baikie, T.; Boix, P. P.; Yantara, N.; Mathews, N. and Mhaisalkar, S. 'Band-gap tuning of lead halide perovskites using a sequential deposition process'. *Journal of Materials Chemistry A*, 2014, **2**, 9221–9225.

[29] Gholipour, S. and Saliba, M. 'Bandgap tuning and compositional exchange for lead halide perovskite materials'. *Characterization Techniques for Perovskite Solar Cell Materials*. Elsevier, 2020, 1–22.

[30] Wehrenfennig, C.; Liu, M.; Snaith, H. J.; Johnston, M. B. and Herz, L. M. 'Charge-carrier dynamics in vapour-deposited films of the organolead halide perovskite $CH_3NH_3PbI_{3-x}Cl_x$'. *Energy & Environmental Science*, 2014, **7**, 2269–2275.

[31] Ponseca Jr, C. S.; Savenije, T. J.; Abdellah, M.; Zheng, K.; Yartsev, A.; Pascher, T.; Harlang, T.; Chabera, P.; Pullerits, T.; Stepanov, A. *et al.* 'Organometal halide perovskite solar cell materials rationalized: ultrafast charge generation, high and microsecond-long balanced mobilities, and slow recombination'. *Journal of the American Chemical Society*, 2014, **136**, 5189–5192.

[32] Green, M. A.; Jiang, Y.; Soufiani, A. M. and Ho-Baillie, A. 'Optical properties of photovoltaic organic–inorganic lead halide perovskites'. *The Journal of Physical Chemistry Letters*, 2015, **6**, 4774–4785.

[33] Green, M. A. and Keevers, M. J. 'Optical properties of intrinsic silicon at 300 K'. *Progress in Photovoltaics: Research and applications*, 1995, **3**, 189–192.

[34] D'innocenzo, V.; Grancini, G.; Alcocer, M. J.; Kandada, A. R. S.; Stranks, S. D.; Lee, M. M.; Lanzani, G.; Snaith, H. J. and Petrozza, A. 'Excitons versus free charges in organo-lead tri-halide perovskites'. *Nat. Commun.*, 2014, **5**, 3586.

[35] Galkowski, K.; Mitioglu, A.; Miyata, A.; Plochocka, P.; Portugall, O.; Eperon, G. E.; Wang, J. T.-W.; Stergiopoulos, T.; Stranks, S. D.; Snaith, H. J. *et al.* 'Determination of the exciton binding energy and effective masses for methylammonium and formamidinium lead tri-halide perovskite semiconductors'. *Energy Environ. Sci.*, 2016, **9**, 962–970.

[36] Miyata, A.; Mitioglu, A.; Plochocka, P.; Portugall, O.; Wang, J. T.-W.; Stranks, S. D.; Snaith, H. J. and Nicholas, R. J. 'Direct measurement of the exciton binding energy and effective masses for charge carriers in organic–inorganic tri-halide perovskites'. *Nat. Phys.*, 2015, **11**, 582.

[37] Hoppe, H. and Sariciftci, N. S. 'Organic solar cells: An overview'. *Journal of Materials Research*, 2004, **19**, 1924–1945.

[38] Yin, W.-J.; Shi, T. and Yan, Y. 'Unusual defect physics in $CH_3NH_3PbI_3$ perovskite solar cell absorber'. *Applied Physics Letters*, 2014, **104**, 063903.

[39] Ostroverkhova, O. *Handbook of organic materials for electronic and photonic devices*. Woodhead Publishing, 2018.

[40] Stranks, S. D.; Eperon, G. E.; Grancini, G.; Menelaou, C.; Alcocer, M. J.; Leijtens, T.; Herz, L. M.; Petrozza, A. and Snaith, H. J. 'Electron-hole diffusion lengths exceeding 1 micrometer in an organometal trihalide perovskite absorber'. *Science*, 2013, **342**, 341–344.

[41] Goetzberger, A.; Knobloch, J. and Voss, B. *Crystalline silicon solar cells*. Vol. 1. Wiley Online Library, 1998.

[42] Brandt, R. E.; Poindexter, J. R.; Gorai, P.; Kurchin, R. C.; Hoye, R. L.; Nienhaus, L.; Wilson, M. W.; Polizzotti, J. A.; Sereika, R.; Zaltauskas, R. *et al.* 'Searching for "defect-tolerant" photovoltaic materials: combined theoretical and experimental screening'. *Chemistry of Materials*, 2017, **29**, 4667–4674.

[43] Motti, S. G.; Meggiolaro, D.; Martani, S.; Sorrentino, R.; Barker, A. J.; De Angelis, F. and Petrozza, A. 'Defect Activity in Lead Halide Perovskites'. *Advanced Materials*, 2019, **31**, 1901183.

[44] Meggiolaro, D.; Motti, S. G.; Mosconi, E.; Barker, A. J.; Ball, J.; Perini, C. A. R.; Deschler, F.; Petrozza, A. and De Angelis, F. 'Iodine chemistry determines the defect tolerance of lead-halide perovskites'. *Energy & Environmental Science*, 2018, **11**, 702–713.

[45] Motti, S. G.; Gandini, M.; Barker, A. J.; Ball, J. M.; Srimath Kandada, A. R. and Petrozza, A. 'Photoinduced emissive trap states in lead halide perovskite semiconductors'. *ACS Energy Letters*, 2016, **1**, 726–730.

[46] Meggiolaro, D.; Ricciarelli, D.; Alasmari, A. A.; Alasmary, F. A. and De Angelis, F. 'Tin versus lead redox chemistry modulates charge trapping and self-doping in tin/lead iodide perovskites'. *J. Phys. Chem. Lett.*, 2020, **11**, 3546–3556.

[47] Lim, V. J.-Y.; Ulatowski, A. M.; Kamaraki, C.; Klug, M. T.; Miranda Perez, L.; Johnston, M. B. and Herz, L. M. 'Air-Degradation Mechanisms in Mixed Lead-Tin Halide Perovskites for Solar Cells'. *Advanced Energy Materials*, 2022, 2200847.

[48] Euvrard, J.; Yan, Y. and Mitzi, D. B. 'Electrical doping in halide perovskites'. *Nature Reviews Materials*, 2021, **6**, 531–549.

[49] Lloyd-Hughes, J. and Jeon, T.-I. 'A review of the terahertz conductivity of bulk and nano-materials'. *Journal of Infrared, Millimeter, and Terahertz Waves*, 2012, **33**, 871–925.

[50] Ulatowski, A. M.; Wright, A. D.; Wenger, B.; Buizza, L. R.; Motti, S. G.; Eggimann, H. J.; Savill, K. J.; Borchert, J.; Snaith, H. J.; Johnston, M. B. *et al.* 'Charge-Carrier Trapping Dynamics in Bismuth-Doped Thin Films of $MAPbBr_3$ Perovskite'. *J. Phys. Chem. Lett.*, 2020, **11**, 3681–3688.

[51] Savill, K. J.; Ulatowski, A. M.; Farrar, M. D.; Johnston, M. B.; Snaith, H. J. and Herz, L. M. 'Impact of Tin Fluoride Additive on the Properties of Mixed Tin-Lead Iodide Perovskite Semiconductors'. *Advanced Functional Materials*, 2020, **30**, 2005594.

[52] Wang, Q.; Shao, Y.; Xie, H.; Lyu, L.; Liu, X.; Gao, Y. and Huang, J. 'Qualifying composition dependent p and n self-doping in $CH_3NH_3PbI_3$'. *Applied Physics Letters*, 2014, **105**, 163508.

[53] Neamen, D. A. *Semiconductor physics and devices: basic principles*. McGraw-hill, 2003.

[54] Rubin, L. and Poate, J. 'Ion implantation in silicon technology'. *Industrial Physicist*, 2003, **9**, 12–15.

[55] Azpiroz, J. M.; Mosconi, E.; Bisquert, J. and De Angelis, F. 'Defect migration in methylammonium lead iodide and its role in perovskite solar cell operation'. *Energy & Environmental Science*, 2015, **8**, 2118–2127.

[56] Yang, Y.; Zou, X.; Pei, Y.; Bai, X.; Jin, W. and Chen, D. 'Effect of doping of NaI monovalent cation halide on the structural, morphological, optical and optoelectronic properties of $MAPbI_3$ perovskite'. *Journal of Materials Science: Materials in Electronics*, 2018, **29**, 205–210.

[57] Abdelhady, A. L.; Saidaminov, M. I.; Murali, B.; Adinolfi, V.; Voznyy, O.; Katsiev, K.; Alarousu, E.; Comin, R.; Dursun, I.; Sinatra, L. *et al.* 'Heterovalent dopant incorporation for bandgap and type engineering of perovskite crystals'. *The Journal of Physical Chemistry Letters*, 2016, **7**, 295–301.

[58] Chatterjee, S.; Dasgupta, U. and Pal, A. J. 'Sequentially deposited antimony-doped $CH_3NH_3PbI_3$ films in inverted planar heterojunction solar cells with a high open-circuit voltage'. *The Journal of Physical Chemistry C*, 2017, **121**, 20177–20187.

[59] Chen, Q.; Chen, L.; Ye, F.; Zhao, T.; Tang, F.; Rajagopal, A.; Jiang, Z.; Jiang, S.; Jen, A. K.-Y.; Xie, Y. *et al.* 'Ag-incorporated organic–inorganic perovskite films and planar heterojunction solar cells'. *Nano Letters*, 2017, **17**, 3231–3237.

[60] Zhou, S.; Ma, Y.; Zhou, G.; Xu, X.; Qin, M.; Li, Y.; Hsu, Y.-J.; Hu, H.; Li, G.; Zhao, N. *et al.* 'Ag-doped halide perovskite nanocrystals for tunable band structure and efficient charge transport'. *ACS Energy Letters*, 2019, **4**, 534–541.

[61] Chen, Y.; Jing, H.; Ling, F.; Kang, W.; Zhou, T.; Liu, X.; Zeng, W.; Zhang, Y.; Qi, L.; Fang, L. *et al.* 'Tuning the electronic structures of all-inorganic lead halide perovskite $CsPbI_3$ via heterovalent doping: A first-principles investigation'. *Chemical Physics Letters*, 2019, **722**, 90–95.

[62] Le Corre, V. M.; Stolterfoht, M.; Perdigon Toro, L.; Feuerstein, M.; Wolff, C.; Gil-Escrig, L.; Bolink, H. J.; Neher, D. and Koster, L. J. A. 'Charge transport layers limiting the efficiency of perovskite solar cells: how to optimize conductivity, doping, and thickness'. *ACS Applied Energy Materials*, 2019, **2**, 6280–6287.

[63] Zhang, X.; Li, L.; Sun, Z. and Luo, J. 'Rational chemical doping of metal halide perovskites'. *Chemical Society Reviews*, 2019, **48**, 517–539.

[64] Jung, C. S.; Kim, H. S.; Jung, G. B.; Gong, K. J.; Cho, Y. J.; Jang, S. Y.; Kim, C. H.; Lee, C.-W. and Park, J. 'Composition and phase tuned InGaAs alloy nanowires'. *The Journal of Physical Chemistry C*, 2011, **115**, 7843–7850.

[65] Begum, R.; Parida, M. R.; Abdelhady, A. L.; Murali, B.; Alyami, N. M.; Ahmed, G. H.; Hedhili, M. N.; Bakr, O. M. and Mohammed, O. F. 'Engineering interfacial charge transfer in $CsPbBr_3$ perovskite nanocrystals by heterovalent doping'. *Journal of the American Chemical Society*, 2017, **139**, 731–737.

[66] Lozhkina, O. A.; Murashkina, A. A.; Shilovskikh, V. V.; Kapitonov, Y. V.; Ryabchuk, V. K.; Emeline, A. V. and Miyasaka, T. 'Invalidity of Band-Gap Engineering Concept for Bi^{3+} Heterovalent Doping in $CsPbBr_3$ Halide Perovskite'. *The Journal of Physical Chemistry Letters*, 2018, **9**, 5408–5411.

[67] Nayak, P. K.; Sendner, M.; Wenger, B.; Wang, Z.; Sharma, K.; Ramadan, A. J.; Lovrincic, R.; Pucci, A.; Madhu, P. and Snaith, H. J. 'Impact of Bi^{3+} heterovalent doping in organic–inorganic metal halide perovskite crystals'. *Journal of the American Chemical Society*, 2018, **140**, 574–577.

[68] Meng, R.; Wu, G.; Zhou, J.; Zhou, H.; Fang, H.; Loi, M. A. and Zhang, Y. 'Understanding the Impact of Bismuth Heterovalent Doping on the Structural and Photophysical Properties of $CH_3NH_3PbBr_3$ Halide Perovskite Crystals with Near-IR Photoluminescence'. *Chemistry–A European Journal*, 2019, **25**, 5480–5488.

[69] Li, X.; Wang, K.; Lgbari, F.; Dong, C.; Yang, W.; Ma, C.; Ma, H.; Wang, Z.-K. and Liao, L.-S. 'Indium doped $CsPbI_3$ films for inorganic perovskite solar cells with efficiency exceeding 17%'. *Nano Research*, 2020, **13**, 2203–2208.

[70] Tavakoli, M. M.; Fazel, Z.; Tavakoli, R.; Akin, S.; Satapathi, S.; Prochowicz, D. and Yadav, P. 'Efficient and Less-Toxic Indium-Doped $MAPbI_3$ Perovskite Solar Cells Prepared by Metal Alloying Technique'. *Solar RRL*, 2022, **6**, 2200106.

[71] Xu, C.; Liu, Z. and Lee, E.-C. 'Non-equivalent Tl doping for high performance perovskite solar cells: Crystal quality improvement with enhanced p-type character'. *Journal of Power Sources*, 2020, **479**, 228818.

[72] Zhang, J.; Shang, M.-h.; Wang, P.; Huang, X.; Xu, J.; Hu, Z.; Zhu, Y. and Han, L. 'N-type doping and energy states tuning in $CH_3NH_3Pb_{1-x}Sb_{2x/3}I_3$ perovskite solar cells'. *ACS Energy Letters*, 2016, **1**, 535–541.

[73] Ricciarelli, D.; Meggiolaro, D.; Ambrosio, F. and De Angelis, F. 'Instability of tin iodide perovskites: bulk p-doping versus surface tin oxidation'. *ACS Energy Letters*, 2020, **5**, 2787–2795.

[74] Noel, N. K.; Stranks, S. D.; Abate, A.; Wehrenfennig, C.; Guarnera, S.; Haghighirad, A.-A.; Sadhanala, A.; Eperon, G. E.; Pathak, S. K.; Johnston, M. B. *et al.* 'Lead-free organic–inorganic tin halide perovskites for photovoltaic applications'. *Energy & Environmental Science*, 2014, **7**, 3061–3068.

[75] Milot, R. L.; Klug, M. T.; Davies, C. L.; Wang, Z.; Kraus, H.; Snaith, H. J.; Johnston, M. B. and Herz, L. M. 'The effects of doping density and temperature on the optoelectronic properties of formamidinium tin triiodide thin films'. *Advanced Materials*, 2018, **30**, 1804506.

[76] Konstantakou, M. and Stergiopoulos, T. 'A critical review on tin halide perovskite solar cells'. *J. Mater. Chem. A*, 2017, **5**, 11518–11549.

[77] Takahashi, Y.; Obara, R.; Lin, Z.-Z.; Takahashi, Y.; Naito, T.; Inabe, T.; Ishibashi, S. and Terakura, K. 'Charge-transport in tin-iodide perovskite $CH_3NH_3SnI_3$: origin of high conductivity'. *Dalton Transactions*, 2011, **40**, 5563–5568.

[78] Marshall, K. P.; Walton, R. I. and Hatton, R. A. 'Tin perovskite/fullerene planar layer photovoltaics: improving the efficiency and stability of lead-free devices'. *Journal of materials chemistry A*, 2015, **3**, 11631–11640.

[79] Kumar, M. H.; Dharani, S.; Leong, W. L.; Boix, P. P.; Prabhakar, R. R.; Baikie, T.; Shi, C.; Ding, H.; Ramesh, R.; Asta, M. *et al.* 'Lead-free halide perovskite solar cells with high photocurrents realized through vacancy modulation'. *Advanced Materials*, 2014, **26**, 7122–7127.

[80] Johnston, M. B. and Herz, L. M. 'Hybrid perovskites for photovoltaics: charge-carrier recombination, diffusion, and radiative efficiencies'. *Acc. Chem. Res.*, 2016, **49**, 146–154.

[81] Lin, R.; Xiao, K.; Qin, Z.; Han, Q.; Zhang, C.; Wei, M.; Saidaminov, M. I.; Gao, Y.; Xu, J.; Xiao, M. *et al.* 'Monolithic all-perovskite tandem solar cells with 24.8% efficiency exploiting comproportionation to suppress Sn (ii) oxidation in precursor ink'. *Nature Energy*, 2019, **4**, 864–873.

[82] Takahashi, Y.; Hasegawa, H.; Takahashi, Y. and Inabe, T. 'Hall mobility in tin iodide perovskite $CH_3NH_3SnI_3$: evidence for a doped semiconductor'. *J. Solid State Chem.*, 2013, **205**, 39–43.

[83] Ulatowski, A. M.; Farrar, M. D.; Snaith, H. J.; Johnston, M. B. and Herz, L. M. 'Revealing Ultrafast Charge-Carrier Thermalization in Tin-Iodide Perovskites through Novel Pump–Push–Probe Terahertz Spectroscopy'. *ACS photonics*, 2021, **8**, 2509–2518.

[84] Hirst, L. C. and Ekins-Daukes, N. J. 'Fundamental losses in solar cells'. *Progress in Photovoltaics: Research and Applications*, 2011, **19**, 286–293.

[85] Rühle, S. 'Tabulated values of the Shockley–Queisser limit for single junction solar cells'. *Solar Energy*, 2016, **130**, 139–147.

[86] Green, M. A. 'Third generation photovoltaics: Ultra-high conversion efficiency at low cost'. *Progress in Photovoltaics: Research and Applications*, 2001, **9**, 123–135.

[87] Herz, L. M. 'Charge-carrier dynamics in organic-inorganic metal halide perovskites'. *Annu. Rev. Phys. Chem.*, 2016, **67**, 65–89.

[88] Anisimov, S.; Kapeliovich, B.; Perelman, T. *et al.* 'Electron emission from metal surfaces exposed to ultrashort laser pulses'. *Zh. Eksp. Teor. Fiz*, 1974, **66**, 375–377.

[89] Dhouib, A and Filali, S. 'Operating temperatures of photovoltaic panels'. *Energy and the Environment*. Elsevier, 1990, 494–498.

[90] Xing, G.; Mathews, N.; Sun, S.; Lim, S. S.; Lam, Y. M.; Grätzel, M.; Mhaisalkar, S. and Sum, T. C. 'Long-range balanced electron-and hole-transport lengths in organic-inorganic $CH_3NH_3PbI_3$'. *Science*, 2013, **342**, 344–347.

[91] Grancini, G.; Maiuri, M.; Fazzi, D.; Petrozza, A.; Egelhaaf, H.-J.; Brida, D.; Cerullo, G. and Lanzani, G. 'Hot exciton dissociation in polymer solar cells'. *Nature Materials*, 2013, **12**, 29–33.

[92] Jailaubekov, A. E.; Willard, A. P.; Tritsch, J. R.; Chan, W.-L.; Sai, N.; Gearba, R.; Kaake, L. G.; Williams, K. J.; Leung, K.; Rossky, P. J. *et al.* 'Hot charge-transfer excitons set the time limit for charge separation at donor/acceptor interfaces in organic photovoltaics'. *Nature Materials*, 2013, **12**, 66–73.

[93] Yang, Y.; Ostrowski, D. P.; France, R. M.; Zhu, K.; Van De Lagemaat, J.; Luther, J. M. and Beard, M. C. 'Observation of a hot-phonon bottleneck in lead-iodide perovskites'. *Nat. Photonics*, 2016, **10**, 53–59.

[94] Zanato, D; Balkan, N; Ridley, B.; Hill, G and Schaff, W. 'Hot electron cooling rates via the emission of LO-phonons in InN'. *Semiconductor Science and Technology*, 2004, **19**, 1024.

[95] Fu, J.; Xu, Q.; Han, G.; Wu, B.; Huan, C. H. A.; Leek, M. L. and Sum, T. C. 'Hot carrier cooling mechanisms in halide perovskites'. *Nature Communications*, 2017, **8**, 1–9.

[96] Sekiguchi, F.; Hirori, H.; Yumoto, G.; Shimazaki, A.; Nakamura, T.; Wakamiya, A. and Kanemitsu, Y. 'Enhancing the hot-phonon bottleneck effect in a metal halide perovskite by terahertz phonon excitation'. *Physical Review Letters*, 2021, **126**, 077401.

[97] Yang, J.; Wen, X.; Xia, H.; Sheng, R.; Ma, Q.; Kim, J.; Tapping, P.; Harada, T.; Kee, T. W.; Huang, F. *et al.* 'Acoustic-optical phonon up-conversion and hot-phonon bottleneck in lead-halide perovskites'. *Nat. Commun.*, 2017, **8**, 1–9.

[98] Shi, H.; Zhang, X.; Sun, X. and Zhang, X. 'Strong hot-phonon bottleneck effect in all-inorganic perovskite nanocrystals'. *Applied Physics Letters*, 2020, **116**, 151902.

[99] Jia, X.; Jiang, J.; Zhang, Y.; Qiu, J.; Wang, S.; Chen, Z.; Yuan, N. and Ding, J. 'Observation of enhanced hot phonon bottleneck effect in 2D perovskites'. *Applied Physics Letters*, 2018, **112**, 143903.

[100] Lim, J. W. M.; Wang, Y.; Fu, J.; Zhang, Q. and Sum, T. C. 'Spotlight on hot carriers in halide perovskite luminescence'. *ACS Energy Letters*, 2022, **7**, 749–756.

[101] Pérez-Higueras, P; Muñoz, E; Almonacid, G and Vidal, P. 'High Concentrator PhotoVoltaics efficiencies: Present status and forecast'. *Renewable and Sustainable Energy Reviews*, 2011, **15**, 1810–1815.

[102] Zhang, C.-X.; Shen, T.; Guo, D.; Tang, L.-M.; Yang, K. and Deng, H.-X. 'Reviewing and understanding the stability mechanism of halide perovskite solar cells'. *InfoMat*, 2020, **2**, 1034–1056.

[103] Tan, W.; Bowring, A. R.; Meng, A. C.; McGehee, M. D. and McIntyre, P. C. 'Thermal stability of mixed cation metal halide perovskites in air'. *ACS Applied Materials & Interfaces*, 2018, **10**, 5485–5491.

[104] Leijtens, T.; Eperon, G. E.; Noel, N. K.; Habisreutinger, S. N.; Petrozza, A. and Snaith, H. J. 'Stability of metal halide perovskite solar cells'. *Advanced Energy Materials*, 2015, **5**, 1500963.

[105] Lin, Y.; Chen, B.; Fang, Y.; Zhao, J.; Bao, C.; Yu, Z.; Deng, Y.; Rudd, P. N.; Yan, Y.; Yuan, Y. *et al.* 'Excess charge-carrier induced instability of hybrid perovskites'. *Nature Communications*, 2018, **9**, 1–9.

[106] Tang, X.; Brandl, M.; May, B.; Levchuk, I.; Hou, Y.; Richter, M.; Chen, H.; Chen, S.; Kahmann, S.; Osvet, A. *et al.* 'Photoinduced degradation of methylammonium lead triiodide perovskite semiconductors'. *Journal of Materials Chemistry A*, 2016, **4**, 15896–15903.

[107] Li, M.; Bhaumik, S.; Goh, T. W.; Kumar, M. S.; Yantara, N.; Grätzel, M.; Mhaisalkar, S.; Mathews, N. and Sum, T. C. 'Slow cooling and highly efficient extraction of hot carriers in colloidal perovskite nanocrystals'. *Nature Communications*, 2017, **8**, 1–10.

[108] Dai, L.; Deng, Z.; Auras, F.; Goodwin, H.; Zhang, Z.; Walmsley, J. C.; Bristowe, P. D.; Deschler, F. and Greenham, N. C. 'Slow carrier relaxation in tin-based perovskite nanocrystals'. *Nature Photonics*, 2021, **15**, 696–702.

[109] Whalley, L. D.; Skelton, J. M.; Frost, J. M. and Walsh, A. 'Phonon anharmonicity, lifetimes, and thermal transport in $CH_3NH_3PbI_3$ from many-body perturbation theory'. *Physical Review B*, 2016, **94**, 220301.

[110] Fang, H.-H.; Adjokatse, S.; Shao, S.; Even, J. and Loi, M. A. 'Long-lived hot-carrier light emission and large blue shift in formamidinium tin triiodide perovskites'. *Nat. Commun.*, 2018, **9**, 1–8.

[111] Savill, K. J.; Klug, M. T.; Milot, R. L.; Snaith, H. J. and Herz, L. M. 'Charge-Carrier Cooling and Polarization Memory Loss in Formamidinium Tin Triiodide'. *J. Phys. Chem. Lett.*, 2019, **10**, 6038–6047.

[112] Kahmann, S.; Shao, S. and Loi, M. A. 'Cooling, scattering, and recombination—the role of the material quality for the physics of tin halide perovskites'. *Adv. Funct. Mater.*, 2019, **29**, 1902963.

[113] Klingshirn, C. F. *Semiconductor Optics*. Springer Science & Business Media, 2012.

[114] Davies, C. L.; Filip, M. R.; Patel, J. B.; Crothers, T. W.; Verdi, C.; Wright, A. D.; Milot, R. L.; Giustino, F.; Johnston, M. B. and Herz, L. M. 'Bimolecular recombination in methylammonium lead triiodide perovskite is an inverse absorption process'. *Nature Communications*, 2018, **9**, 293.

[115] Peter, Y. and Cardona, M. *Fundamentals of Semiconductors: Physics and Materials Properties*. Springer Science & Business Media, 2010.

[116] Holgate, S. A. *Understanding solid state physics*. cRc Press, 2021.

[117] Elliott, R. 'Intensity of optical absorption by excitons'. *Physical Review*, 1957, **108**, 1384.

[118] Fox, M. *Optical Properties of Solids*. 2001.

[119] Lakowicz, J. R. *Principles of Fluorescence Spectroscopy*. Springer, 2006.

[120] Knight, A. J.; Borchert, J.; Oliver, R. D.; Patel, J. B.; Radaelli, P. G.; Snaith, H. J.; Johnston, M. B. and Herz, L. M. 'Halide segregation in mixed-halide perovskites: influence of A-site cations'. *ACS Energy Letters*, 2021, **6**, 799–808.

[121] Richter, J. M.; Branchi, F.; Almeida Camargo, F. V. de; Zhao, B.; Friend, R. H.; Cerullo, G. and Deschler, F. 'Ultrafast carrier thermalization in lead iodide perovskite probed with two-dimensional electronic spectroscopy'. *Nat. Commun.*, 2017, **8**, 1–7.

[122] Landsberg, P. T. *Recombination in semiconductors*. Cambridge University Press, 2003.

[123] Van Roosbroeck, W and Shockley, W. 'Photon-radiative recombination of electrons and holes in germanium'. *Physical Review*, 1954, **94**, 1558.

[124] Stranks, S. D. and Snaith, H. J. 'Metal-halide perovskites for photovoltaic and light-emitting devices'. *Nature nanotechnology*, 2015, **10**, 391–402.

[125] Davies, C. L.; Patel, J. B.; Xia, C. Q.; Herz, L. M. and Johnston, M. B. 'Temperature-Dependent Refractive Index of Quartz at Terahertz Frequencies'. *Journal of Infrared, Millimeter, and Terahertz Waves*, 2018, **39**, 1236–1248.

[126] Seifert, T.; Jaiswal, S; Martens, U; Hannegan, J; Braun, L.; Maldonado, P.; Freimuth, F; Kronenberg, A; Henrizi, J; Radu, I *et al.* 'Efficient metallic spintronic emitters of ultrabroadband terahertz radiation'. *Nature Photonics*, 2016, **10**, 483.

[127] Auston, D. H. and Nuss, M. C. 'Electrooptical generation and detection of femtosecond electrical transients'. *IEEE Journal of Quantum Electronics*, 1988, **24**, 184–197.

[128] Ulatowski, A. M.; Herz, L. M. and Johnston, M. B. 'Terahertz Conductivity Analysis for Highly Doped Thin-Film Semiconductors'. *J. Infrared, Millimeter, Terahertz Waves*, 2020, **41**, 1431–1449.

[129] Chopra, K.; Paulson, P. and Dutta, V. 'Thin-film solar cells: an overview'. *Progress in Photovoltaics: Research and applications*, 2004, **12**, 69–92.

[130] Lin, Q.; Armin, A.; Nagiri, R. C. R.; Burn, P. L. and Meredith, P. 'Electro-optics of perovskite solar cells'. *Nature Photonics*, 2015, **9**, 106.

[131] Wehrenfennig, C.; Eperon, G. E.; Johnston, M. B.; Snaith, H. J. and Herz, L. M. 'High charge carrier mobilities and lifetimes in organolead trihalide perovskites'. *Advanced materials*, 2014, **26**, 1584–1589.

[132] Rehman, W.; Milot, R. L.; Eperon, G. E.; Wehrenfennig, C.; Boland, J. L.; Snaith, H. J.; Johnston, M. B. and Herz, L. M. 'Charge-carrier dynamics and mobilities in formamidinium lead mixed-halide perovskites'. *Advanced Materials*, 2015, **27**, 7938–7944.

[133] Yettapu, G. R.; Talukdar, D.; Sarkar, S.; Swarnkar, A.; Nag, A.; Ghosh, P. and Mandal, P. 'Terahertz conductivity within colloidal $CsPbBr_3$ perovskite nanocrystals: remarkably high carrier mobilities and large diffusion lengths'. *Nano letters*, 2016, **16**, 4838–4848.

[134] Herz, L. M. 'Charge-carrier mobilities in metal halide perovskites: fundamental mechanisms and limits'. *ACS Energy Letters*, 2017, **2**, 1539–1548.

[135] Nienhuys, H.-K. and Sundström, V. 'Intrinsic complications in the analysis of optical-pump, terahertz probe experiments'. *Physical Review B*, 2005, **71**, 235110.

[136] Vorakiat, C. La-o; Cheng, L.; Salim, T.; Marcus, R. A.; Michel-Beyerle, M.-E.; Lam, Y. M. and Chia, E. E. 'Phonon features in terahertz photoconductivity spectra due to data analysis artifact: A case study on organometallic halide perovskites'. *Applied Physics Letters*, 2017, **110**, 123901.

[137] Ulbricht, R.; Hendry, E.; Shan, J.; Heinz, T. F. and Bonn, M. 'Carrier dynamics in semiconductors studied with time-resolved terahertz spectroscopy'. *Reviews of Modern Physics*, 2011, **83**, 543.

[138] Duvillaret, L.; Garet, F. and Coutaz, J.-L. 'A reliable method for extraction of material parameters in terahertz time-domain spectroscopy'. *IEEE Journal of selected topics in quantum electronics*, 1996, **2**, 739–746.

[139] Neu, J.; Regan, K. P.; Swierk, J. R. and Schmuttenmaer, C. A. 'Applicability of the thin-film approximation in terahertz photoconductivity measurements'. *Applied Physics Letters*, 2018, **113**, 233901.

[140] Withayachumnankul, W.; O'Hara, J. F.; Cao, W.; Al-Naib, I. and Zhang, W. 'Lower bound of sample thickness in terahertz time-domain spectroscopy'. *2014 39th International Conference on Infrared, Millimeter, and Terahertz waves (IRMMW-THz)*. IEEE. 2014, 1–2.

[141] Jo, J.; Jung, E.; Park, J. C. and Hwang, J. 'Comparative study of optical analysis methods for thin films'. *Current Applied Physics*, 2020, **20**, 237–243.

[142] Neu, J. and Schmuttenmaer, C. A. 'Tutorial: An introduction to terahertz time domain spectroscopy (THz-TDS)'. *Journal of Applied Physics*, 2018, **124**, 231101.

[143] Wang, T.; Zalkovskij, M.; Iwaszczuk, K.; Lavrinenko, A. V.; Naik, G. V.; Kim, J.; Boltasseva, A. and Jepsen, P. U. 'Ultrabroadband terahertz conductivity of highly doped ZnO and ITO'. *Optical Materials Express*, 2015, **5**, 566–575.

[144] O'Hara, J. F.; Withayachumnankul, W. and Al-Naib, I. 'A review on thin-film sensing with terahertz waves'. *Journal of Infrared, Millimeter, and Terahertz Waves*, 2012, **33**, 245–291.

[145] Tinkham, M. 'Energy gap interpretation of experiments on infrared transmission through superconducting films'. *Phys. Rev.*, 1956, **104**, 845.

[146] Glover III, R. and Tinkham, M. 'Conductivity of Superconducting Films for Photon Energies between 0.3 and 40 kT_c'. *Phys. Rev.*, 1957, **108**, 243.

[147] Jeon, T.-I. and Grischkowsky, D. 'Characterization of optically dense, doped semiconductors by reflection THz time domain spectroscopy'. *Applied Physics Letters*, 1998, **72**, 3032–3034.

[148] Willis, K.; Hagness, S. and Knezevic, I. 'A generalized Drude model for doped silicon at terahertz frequencies derived from microscopic transport simulation'. *Applied Physics Letters*, 2013, **102**, 122113.

[149] Yan, F.; Parrott, E. P.; Ung, B. S.-Y. and Pickwell-MacPherson, E. 'Solvent doping of PEDOT/PSS: effect on terahertz optoelectronic properties and utilization in terahertz devices'. *The Journal of Physical Chemistry C*, 2015, **119**, 6813–6818.

[150] Ordal, M. A.; Bell, R. J.; Alexander, R. W.; Long, L. L. and Querry, M. R. 'Optical properties of fourteen metals in the infrared and far infrared: Al, Co, Cu, Au, Fe, Pb, Mo, Ni, Pd, Pt, Ag, Ti, V, and W.' *Applied optics*, 1985, **24**, 4493–4499.

[151] Zhou, D.-X.; Parrott, E. P.; Paul, D. J. and Zeitler, J. A. 'Determination of complex refractive index of thin metal films from terahertz time-domain spectroscopy'. *Journal of Applied Physics*, 2008, **104**, 053110.

[152] Tiwana, P.; Parkinson, P.; Johnston, M. B.; Snaith, H. J. and Herz, L. M. 'Ultrafast terahertz conductivity dynamics in mesoporous TiO_2: influence of dye sensitization and surface treatment in solid-state dye-sensitized solar cells'. *J. Phys. Chem. C*, 2010, **114**, 1365–1371.

[153] Sarkar, S.; Ravi, V. K.; Banerjee, S.; Yettapu, G. R.; Markad, G. B.; Nag, A. and Mandal, P. 'Terahertz Spectroscopic Probe of Hot Electron and Hole Transfer from Colloidal $CsPbBr_3$ Perovskite Nanocrystals'. *Nano letters*, 2017, **17**, 5402–5407.

[154] Zhao, D. and Chia, E. E. 'Free Carrier, Exciton, and Phonon Dynamics in Lead-Halide Perovskites Studied with Ultrafast Terahertz Spectroscopy'. *Advanced Optical Materials*, 2020, **8**, 1900783.

[155] Burdanova, M. G.; Tsapenko, A. P.; Satco, D. A.; Kashtiban, R.; Mosley, C. D.; Monti, M.; Staniforth, M.; Sloan, J.; Gladush, Y. G.; Nasibulin, A. G. and Lloyd-Hughes, J. 'Giant negative terahertz photoconductivity in controllably doped carbon nanotube networks'. *ACS Photonics*, 2019, **6**, 1058–1066.

[156] De Wolf, S.; Holovsky, J.; Moon, S.-J.; Löper, P.; Niesen, B.; Ledinsky, M.; Haug, F.-J.; Yum, J.-H. and Ballif, C. 'Organometallic halide perovskites: sharp optical absorption edge and its relation to photovoltaic performance'. *J. Phys. Chem. Lett.*, 2014, **5**, 1035–1039.

[157] Hao, F.; Stoumpos, C. C.; Cao, D. H.; Chang, R. P. and Kanatzidis, M. G. 'Lead-free solid-state organic–inorganic halide perovskite solar cells'. *Nat. Photonics*, 2014, **8**, 489–494.

[158] Zhao, B.; Abdi-Jalebi, M.; Tabachnyk, M.; Glass, H.; Kamboj, V. S.; Nie, W.; Pearson, A. J.; Puttisong, Y.; Gödel, K. C.; Beere, H. E. *et al.* 'High Open-Circuit Voltages in Tin-Rich Low-Bandgap Perovskite-Based Planar Heterojunction Photovoltaics'. *Adv. Mater.*, 2017, **29**, 1604744.

[159] Rajendra Kumar, G; Kim, H.-J.; Karupannan, S. and Prabakar, K. 'Interplay between iodide and tin vacancies in $CsSnI_3$ perovskite solar cells'. *J. Phys. Chem. C*, 2017, **121**, 16447–16453.

[160] Shi, T.; Zhang, H.-S.; Meng, W.; Teng, Q.; Liu, M.; Yang, X.; Yan, Y.; Yip, H.-L. and Zhao, Y.-J. 'Effects of organic cations on the defect physics of tin halide perovskites'. *J. Mater. Chem. A*, 2017, **5**, 15124–15129.

[161] Lee, S. J.; Shin, S. S.; Kim, Y. C.; Kim, D.; Ahn, T. K.; Noh, J. H.; Seo, J. and Seok, S. I. 'Fabrication of efficient formamidinium tin iodide perovskite solar cells through SnF_2–pyrazine complex'. *J. Am. Chem. Soc.*, 2016, **138**, 3974–3977.

[162] Leijtens, T.; Prasanna, R.; Gold-Parker, A.; Toney, M. F. and McGehee, M. D. 'Mechanism of tin oxidation and stabilization by lead substitution in tin halide perovskites'. *ACS Energy Lett.*, 2017, **2**, 2159–2165.

[163] Xu, X.; Chueh, C.-C.; Yang, Z.; Rajagopal, A.; Xu, J.; Jo, S. B. and Jen, A. K.-Y. 'Ascorbic acid as an effective antioxidant additive to enhance the efficiency and stability of Pb/Sn-based binary perovskite solar cells'. *Nano Energy*, 2017, **34**, 392–398.

[164] Tong, J.; Song, Z.; Kim, D. H.; Chen, X.; Chen, C.; Palmstrom, A. F.; Ndione, P. F.; Reese, M. O.; Dunfield, S. P.; Reid, O. G. *et al.* 'Carrier lifetimes of $> 1\,\mu$s in Sn − Pb perovskites enable efficient all-perovskite tandem solar cells'. *Science*, 2019, **364**, 475–479.

[165] Yang, Z.; Yu, Z.; Wei, H.; Xiao, X.; Ni, Z.; Chen, B.; Deng, Y.; Habisreutinger, S. N.; Chen, X.; Wang, K. *et al.* 'Enhancing electron diffusion length in narrow-bandgap perovskites for efficient monolithic perovskite tandem solar cells'. *Nat. Commun.*, 2019, **10**, 1–9.

[166] Bowman, A. R.; Klug, M. T.; Doherty, T. A.; Farrar, M. D.; Senanayak, S. P.; Wenger, B.; Divitini, G.; Booker, E. P.; Andaji-Garmaroudi, Z.; Macpherson, S. *et al.* 'Microsecond Carrier Lifetimes, Controlled p-Doping, and Enhanced Air Stability in Low-Bandgap Metal Halide Perovskites'. *ACS Energy Lett.*, 2019, **4**, 2301–2307.

[167] Eames, C.; Frost, J. M.; Barnes, P. R.; O'Regan, B. C.; Walsh, A. and Islam, M. S. 'Ionic transport in hybrid lead iodide perovskite solar cells'. *Nat. Commun.*, 2015, **6**, 1–8.

[168] Knight, A. J. and Herz, L. M. 'Preventing phase segregation in mixed-halide perovskites: a perspective'. *Energy Environ. Sci.*, 2020, **13**, 2024–2046.

[169] Shockley, W. and Queisser, H. J. 'Detailed balance limit of efficiency of p-n junction solar cells'. *J. Appl. Phys.*, 1961, **32**, 510–519.

[170] Hopper, T. R.; Gorodetsky, A.; Frost, J. M.; Müller, C.; Lovrincic, R. and Bakulin, A. A. 'Ultrafast intraband spectroscopy of hot-carrier cooling in lead-halide perovskites'. *ACS Energy Lett.*, 2018, **3**, 2199–2205.

[171] Hopper, T. R.; Jeong, A.; Gorodetsky, A. A.; Krieg, F.; Bodnarchuk, M. I.; Huang, X.; Lovrincic, R.; Kovalenko, M. V. and Bakulin, A. A. 'Kinetic modelling of intraband carrier relaxation in bulk and nanocrystalline lead-halide perovskites'. *Phys. Chem. Chem. Phys.*, 2020, **22**, 17605–17611.

[172] Righetto, M.; Lim, S. S.; Giovanni, D.; Lim, J. W. M.; Zhang, Q.; Ramesh, S.; Tay, Y. K. E. and Sum, T. C. 'Hot carriers perspective on the nature of traps in perovskites'. *Nat. Commun.*, 2020, **11**, 1–9.

[173] Lim, S. S.; Giovanni, D.; Zhang, Q.; Solanki, A.; Jamaludin, N. F.; Lim, J. W. M.; Mathews, N.; Mhaisalkar, S.; Pshenichnikov, M. S. and Sum, T. C. 'Hot carrier extraction in $CH_3NH_3PbI_3$ unveiled by pump-push-probe spectroscopy'. *Sci. Adv.*, 2019, **5**, eaax3620.

[174] Lu, J.; Liu, H. and Sun, J. 'Negative terahertz photoconductivity in 2D layered materials'. *Nanotechnology*, 2017, **28**, 464001.

[175] Docherty, C. J.; Lin, C.-T.; Joyce, H. J.; Nicholas, R. J.; Herz, L. M.; Li, L.-J. and Johnston, M. B. 'Extreme sensitivity of graphene photoconductivity to environmental gases'. *Nat. Commun.*, 2012, **3**, 1–6.

[176] Kar, S.; Mohapatra, D. R.; Freysz, E. and Sood, A. K. 'Tuning photoinduced terahertz conductivity in monolayer graphene: Optical-pump terahertz-probe spectroscopy'. *Phys. Rev. B*, 2014, **90**, 165420.

[177] Jnawali, G.; Rao, Y.; Yan, H. and Heinz, T. F. 'Observation of a transient decrease in terahertz conductivity of single-layer graphene induced by ultrafast optical excitation'. *Nano Lett.*, 2013, **13**, 524–530.

[178] George, P. A.; Strait, J.; Dawlaty, J.; Shivaraman, S.; Chandrashekhar, M.; Rana, F. and Spencer, M. G. 'Ultrafast optical-pump terahertz-probe spectroscopy of the carrier relaxation and recombination dynamics in epitaxial graphene'. *Nano Lett.*, 2008, **8**, 4248–4251.

[179] He, Y.; Su, R.; Huang, Y.; Zhou, Y.; Zhao, Q.; Khurgin, J. B.; Xiong, Q. and Xu, X. 'High-Order Shift Current Induced Terahertz Emission from Inorganic Cesium Bromine Lead Perovskite Engendered by Two-Photon Absorption'. *Adv. Funct. Mater.*, 2019, **29**, 1904694.

[180] Walters, G.; Sutherland, B. R.; Hoogland, S.; Shi, D.; Comin, R.; Sellan, D. P.; Bakr, O. M. and Sargent, E. H. 'Two-photon absorption in organometallic bromide perovskites'. *ACS Nano*, 2015, **9**, 9340–9346.

[181] Han, L.; Wu, L.; Liu, C. and Zhang, J. 'Doping-Enhanced Visible-Light Absorption of $CH_3NH_3PbBr_3$ by the Bi^{3+}-Induced Impurity Band without Sacrificing a Band gap'. *The Journal of Physical Chemistry C*, 2019, **123**, 8578–8587.

[182] Hu, Y.; Bai, F.; Liu, X.; Ji, Q.; Miao, X.; Qiu, T. and Zhang, S. 'Bismuth incorporation stabilized α-$CsPbI_3$ for fully inorganic perovskite solar cells'. *ACS Energy Letters*, 2017, **2**, 2219–2227.

[183] Yamada, Y.; Hoyano, M.; Oto, K. and Kanemitsu, Y. 'Effects of Impurity Doping on Photoluminescence Properties of $APbX_3$ Lead Halide Perovskites'. *Physica Status Solidi (b)*, 2019, 1800545.

[184] Li, J.-L.; Yang, J.; Wu, T. and Wei, S.-H. 'Formation of DY center as n-type limiting defects in octahedral semiconductors: the case of Bi-doped hybrid halide perovskites'. *Journal of Materials Chemistry C*, 2019, **7**, 4230–4234.

[185] Yavari, M.; Ebadi, F.; Meloni, S.; Wang, Z. S.; Yang, T. C.-J.; Sun, S.; Schwartz, H.; Wang, Z.; Niesen, B.; Durantini, J. *et al.* 'How far does the defect tolerance of lead-halide perovskites range? The example of Bi impurities introducing efficient recombination centers'. *Journal of Materials Chemistry A*, 2019.

[186] Yamada, Y.; Hoyano, M.; Akashi, R.; Oto, K. and Kanemitsu, Y. 'Impact of chemical doping on optical responses in bismuth-doped $CH_3NH_3PbBr_3$ single crystals: carrier lifetime and photon recycling'. *The Journal of Physical Chemistry Letters*, 2017, **8**, 5798–5803.

[187] Wehrenfennig, C.; Liu, M.; Snaith, H. J.; Johnston, M. B. and Herz, L. M. 'Homogeneous emission line broadening in the organo lead halide perovskite $CH_3NH_3PbI_{3-x}Cl_x$'. *The Journal of Physical Chemistry Letters*, 2014, **5**, 1300–1306.

[188] Wright, A. D.; Verdi, C.; Milot, R. L.; Eperon, G. E.; Pérez-Osorio, M. A.; Snaith, H. J.; Giustino, F.; Johnston, M. B. and Herz, L. M. 'Electron–phonon coupling in hybrid lead halide perovskites'. *Nature Communications*, 2016, **7**, 11755.

[189] Sestu, N.; Cadelano, M.; Sarritzu, V.; Chen, F.; Marongiu, D.; Piras, R.; Mainas, M.; Quochi, F.; Saba, M.; Mura, A. *et al.* 'Absorption F-sum rule for the exciton binding energy in methylammonium lead halide perovskites'. *The Journal of Physical Chemistry Letters*, 2015, **6**, 4566–4572.

[190] Crothers, T. W.; Milot, R. L.; Patel, J. B.; Parrott, E. S.; Schlipf, J.; Muller-Buschbaum, P.; Johnston, M. B. and Herz, L. M. 'Photon reabsorption masks intrinsic bimolecular charge-carrier recombination in $CH_3NH_3PbI_3$ perovskite'. *Nano Letters*, 2017, **17**, 5782–5789.

[191] Milot, R. L.; Eperon, G. E.; Green, T.; Snaith, H. J.; Johnston, M. B. and Herz, L. M. 'Radiative monomolecular recombination boosts amplified spontaneous emission in HC $(NH_2)_2SnI_3$ perovskite films'. *The journal of physical chemistry letters*, 2016, **7**, 4178–4184.

[192] Feng, J. and Xiao, B. 'Crystal structures, optical properties, and effective mass tensors of $CH_3NH_3PbX_3$ (X= I and Br) phases predicted from HSE06'. *The Journal of Physical Chemistry Letters*, 2014, **5**, 1278–1282.

[193] Chang, Y.; Park, C. H. and Matsuishi, K. 'First-principles study of the Structural and the electronic properties of the lead-halide-based inorganic-organic perovskites $(CH_3NH_3)PbX_3$ and $CsPbX_3$ (X= Cl, Br, I)'. *Journal of the Korean Physical Society*, 2004, **44**, 889–893.

[194] Melissen, S. T. A. G.; Labat, F.; Sautet, P. and Le Bahers, T. 'Electronic properties of $PbX_3CH_3NH_3$ (X = Cl, Br, I) compounds for photovoltaic and photocatalytic applications'. *Physical Chemistry Chemical Physics*, 2015, **17**, 2199–2209.

[195] Akkerman, Q. A.; Motti, S. G.; Srimath Kandada, A. R.; Mosconi, E.; D'Innocenzo, V.; Bertoni, G.; Marras, S.; Kamino, B. A.; Miranda, L.; De Angelis, F. *et al.* 'Solution synthesis approach to colloidal cesium lead halide perovskite nanoplatelets with monolayer-level thickness control'. *Journal of the American Chemical Society*, 2016, **138**, 1010–1016.

[196] Yao, J.-S.; Ge, J.; Han, B.-N.; Wang, K.-H.; Yao, H.-B.; Yu, H.-L.; Li, J.-H.; Zhu, B.-S.; Song, J.-Z.; Chen, C. *et al.* 'Ce^{3+}-doping to modulate photoluminescence kinetics for efficient $CsPbBr_3$ nanocrystals based light-emitting diodes'. *Journal of the American Chemical Society*, 2018, **140**, 3626–3634.

[197] Perry, E. E.; Labram, J. G.; Venkatesan, N. R.; Nakayama, H. and Chabinyc, M. L. 'N-Type Surface Doping of $MAPbI_3$ via Charge Transfer from Small Molecules'. *Advanced Electronic Materials*, 2018, **4**, 1800087.

[198] Noel, N. K.; Habisreutinger, S. N.; Pellaroque, A.; Pulvirenti, F.; Wenger, B.; Zhang, F.; Lin, Y.-H.; Reid, O. G.; Leisen, J.; Zhang, Y. *et al.* 'Interfacial charge-transfer doping of metal halide perovskites for high performance photovoltaics'. *Energy & Environmental Science*, 2019, **12**, 3063–3073.

[199] Pan, H.; Xie, A.; Hou, S.; Yin, X.; Tang, C. S.; Hoa, N. T.; Birowosuto, M. D.; Wang, H.; Dang, C.; Rusydi, A. *et al.* 'Surface molecular doping of all-inorganic perovskite using zethrenes molecules'. *Nano Research*, 2019, **12**, 77–84.

[200] Liao, W.; Zhao, D.; Yu, Y.; Shrestha, N.; Ghimire, K.; Grice, C. R.; Wang, C.; Xiao, Y.; Cimaroli, A. J.; Ellingson, R. J. *et al.* 'Fabrication of efficient low-bandgap perovskite solar cells by combining formamidinium tin iodide with methylammonium lead iodide'. *J. Am. Chem. Soc.*, 2016, **138**, 12360–12363.

[201] Wei, M.; Xiao, K.; Walters, G.; Lin, R.; Zhao, Y.; Saidaminov, M. I.; Todorović, P.; Johnston, A.; Huang, Z.; Chen, H. *et al.* 'Combining efficiency and stability in mixed tin–lead perovskite solar cells by capping grains with an ultrathin 2D layer'. *Adv. Mater.*, 2020, **32**, 1907058.

[202] Liu, C.; Fan, J.; Li, H.; Zhang, C. and Mai, Y. 'Highly efficient perovskite solar cells with substantial reduction of lead content'. *Sci. Rep.*, 2016, **6**, 1–8.

[203] Hao, F.; Stoumpos, C. C.; Chang, R. P. and Kanatzidis, M. G. 'Anomalous band gap behavior in mixed Sn and Pb perovskites enables broadening of absorption spectrum in solar cells'. *J. Am. Chem. Soc.*, 2014, **136**, 8094–8099.

[204] Patel, J. B.; Milot, R. L.; Wright, A. D.; Herz, L. M. and Johnston, M. B. 'Formation dynamics of $CH_3NH_3PbI_3$ perovskite following two-step layer deposition'. *The Journal of Physical Chemistry Letters*, 2015, **7**, 96–102.

[205] Wang, K.-H.; Li, L.-C.; Shellaiah, M. and Sun, K. W. 'Structural and Photophysical Properties of Methylammonium Lead Tribromide ($MAPbBr_3$) Single Crystals'. *Scientific Reports*, 2017, **7**, 13643.

[206] Zhao, D.; Skelton, J. M.; Hu, H.; Vorakiat, C. La-o; Zhu, J.-X.; Marcus, R. A.; Michel-Beyerle, M.-E.; Lam, Y. M.; Walsh, A. and Chia, E. E. 'Low-frequency optical phonon modes and carrier mobility in the halide perovskite $CH_3NH_3PbBr_3$ using terahertz time-domain spectroscopy'. *Applied Physics Letters*, 2017, **111**, 201903.